Propagation of plate acoustic waves in contact with fluid medium

Nagaraj Ghatadi Suraji
Marquette University

PROPAGATION OF PLATE ACOUSTIC WAVES IN CONTACT WITH FLUID MEDIUM

by

Nagaraj Ghatadi Suraji

A Thesis submitted to the Faculty of the Graduate School,
Marquette University,
in Partial Fulfillment of the Requirements for the
Degree of Master of Science

Milwaukee, Wisconsin

May 2011

ABSTRACT
PROPAGATION OF PLATE ACOUSTIC WAVES IN CONTACT WITH FLUID MEDIUM

Nagaraj Ghatadi Suraji

Marquette University, 2011

The characteristics of acoustic waves propagating in thin piezoelectric plates in the presence of a fluid medium contacting one or both of the plate surfaces are investigated. If the velocity of plate wave in the substrate is greater than velocity of bulk wave in the fluid, then a plate acoustic wave (PAW) traveling in the substrate will radiate a bulk acoustic wave (BAW) in the fluid. It is found that, under proper conditions, efficient conversion of energy from plate acoustic waves to bulk acoustic waves and vice versa can be obtained. For example, using the fundamental anti symmetric plate wave mode (A_0 mode) propagating in a lithium niobate substrate and water as the fluid, total mode conversion loss (PAW to BAW and back from BAW to PAW) of less than 3 dB has been obtained. This mode conversion principle can be used to realize miniature, high efficiency transducers for use in ultrasonic flow meters. Similar type of transducer based on conversion of energy from surface acoustic wave (SAW) to bulk acoustic wave (BAW) has been developed previously. The use of plate waves has several advantages. Since the energy of plate waves is present on both plate surfaces, the inter digital transducer (IDT) can be on the surface opposite from that which is in contact with the fluid. This protects the IDT from possible damage due to the fluid and also simplifies the job of making electrical connections to the IDT. Another advantage is that one has wider choice of substrate materials with plate waves than is the case with SAWs. Preliminary calculations indicate that the mode conversion principle can also be used to generate and detect ultrasonic waves in air. This has potential applications for realizing transducers for use in non-contact ultrasonic's. The design of an ASIC (Application Specific Integrated Circuit) chip containing an amplifier and frequency counter for use with ultrasonic transducers is also presented in this thesis.

TABLE OF CONTENTS

LIST OF TABLES

LIST OF FIGURES

Chapter 1

Introduction

This thesis is concerned with the investigation of acoustic waves propagating in thin piezoelectric plates in the presence of a fluid medium contacting one or both of the plate surfaces. This work was motivated by prior work in our laboratory which had found that, under suitable conditions, a surface acoustic wave propagating in a piezoelectric substrate can efficiently generate a bulk acoustic wave in a liquid medium. One of the important applications of this effect has been to realize miniature, high efficiency transducers for use in ultrasonic flow meters [1, 2]. This made us think as to whether the same effect can also be observed with plate acoustic waves. That is, whether a plate acoustic wave can also efficiently generate a bulk acoustic wave. If so, this would be very useful, because for flow meter applications, the use of plate acoustic waves will have several advantages over the use of surface acoustic waves. These advantages are as follows. Since the energy of plate waves is present on both plate surfaces, the inter digital transducer (IDT) can be on the surface opposite from that which is in contact with the fluid. This protects the IDT from possible damage due to the fluid and also simplifies the job of making electrical connections to the IDT. Another advantage is that one has wider choice of substrate materials with plate waves than is the case with SAWs. This point will be explained in the next chapter. The analysis carried out in this thesis shows that plate waves can indeed be used to efficiently generate bulk waves in liquids. The theoretical analysis has been extended to the case where the fluid contacting the plate is a gas. It is found that, in this case also, the plate wave can radiate bulk acoustic wave in the

surrounding gas. This has potential applications for development of efficient transducers for generation and detection of ultrasonic waves in air. Another part of this thesis is concerned with the development of an ASIC (Application Specific Integrated Circuit) chip suitable for use with acoustic wave transducers and sensors.

This thesis is organized as follows. The first chapter provides a brief introduction to the subject of acoustic waves in solids and ultrasonic flow meters. The analysis of plate acoustic wave propagation in the presence of a fluid medium is presented in the second chapter. The third chapter discusses the design, fabrication, and evaluation of ASIC circuits for use with ultrasonic transducers. The last chapter presents a summary of the work done in this thesis and suggestions for future work in this area.

1.1 Acoustic waves in solids

Acoustic wave devices have been in commercial use for over 60 years. The telecommunications industry is the largest user of these devices, consuming approximately three billion acoustic wave filters annually, primarily for mobile phones and base stations. There are several new emerging applications for acoustic wave devices as sensors that may eventually equal the demand of the telecommunications market. These include automotive applications (torque and tire pressure sensors), medical applications (biosensors), and industrial and commercial applications (vapor, humidity, temperature and mass sensors). Acoustic wave sensors are competitively priced, inherently rugged, very sensitive, and intrinsically reliable [3]. Acoustic wave sensors are so named because they use acoustic wave as sensing mechanism. This section briefly describes basic acoustic waves that can propagate in solids. Acoustic waves that can propagate in solids can be classified as:

1. Bulk Acoustic Waves (BAW),
2. Surface Acoustic Waves (SAW), and
3. Plate Acoustic Waves (PAW).

Bulk acoustic waves travel in an unbounded elastic medium. There are two types of bulk waves: longitudinal waves and transverse waves. In isotropic solids, the velocity of longitudinal waves is approximately twice the velocity of transverse waves. BAW devices are widely used in communication applications as quartz resonators and delay lines [4, 5].

A typical thickness shear mode (TSM) quartz resonator is shown in Fig. 1. Metal electrodes are deposited on each face of a thin wafer of quartz. Applying an electrical signal to the electrodes induces strain in the quartz wafer. The fundamental frequency of this oscillator is determined by the condition that $h = \lambda/2$, where h is the thickness of the quartz crystal and λ is the acoustic wavelength. Thus the fundamental resonant frequency f_0 of the quartz oscillator is given by the equation

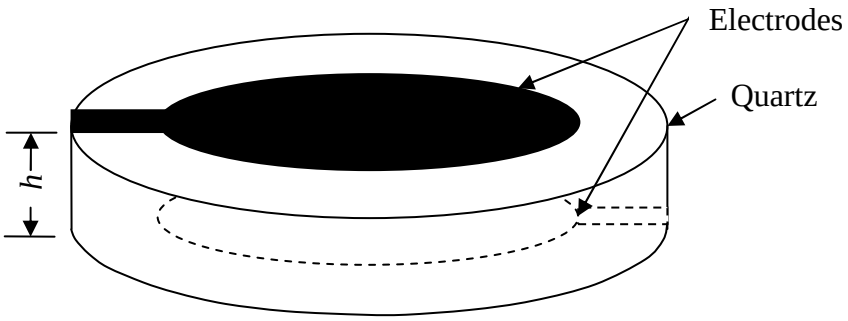

Fig. 1: Three dimensional view of Bulk acoustic wave resonator.

$$f_0 = \frac{v_t}{2h} \tag{1}$$

where v_t is the velocity of transverse shear waves in quartz. Even though this resonator was developed in 1918, this is still widely in use because of its stable operation.

Delay lines are devices used to slow down a signal by a time interval in an electrical network. Radio talk shows routinely use ultrasonic delay lines to monitor and cut off abusive callers before their comments are aired during radio talk shows. The ultrasonic delay line bounces the voice signal back and forth between two transducers until it has been monitored, then releases it for broadcast. A schematic diagram of a BAW delay line is shown in Fig. 2. An electrical signal applied to transducer T_1 is converted into an acoustic wave that propagates through the delay medium to the output transducer $T_{2.}$ At the output transducer $T_{2,}$ the acoustic wave is converted back into an electrical signal. The output signal is a delayed replica of the input signal. The time delay t_d of the delay line is given by the equation

$$t_d = L/v \tag{2}$$

where L is the length of the delay medium and v is the velocity of bulk acoustic wave in the delay medium.

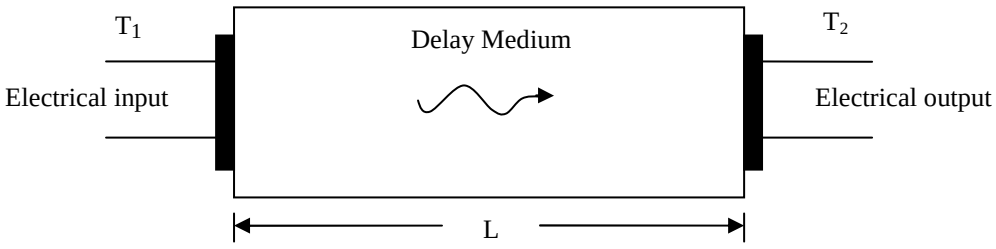

Fig. 2: Bulk acoustic wave delay line.

Surface acoustic waves propagate along the stress free boundary of a semi infinite elastic medium. The motion of the particles is high at the surface and decays as one

moves into the medium away from the surface. SAW waves can propagate in any direction, in isotropic and anisotropic media, with or without losses. Losses are due to scattering at the surface, impurities in a solid, and scratches on the surface. Surface waves are also popularly known as Rayleigh waves, name given after the scientist Lord Rayleigh, who developed the theory of surface waves while studying the waves generated by earthquake in 1881. Surface waves are very sensitive to surface irregularities. SAW devices can be designed and fabricated for frequencies at least two orders of magnitude higher than BAW devices, thus capable of providing higher sensitivity. They can be operated in a frequency range of 10 MHz to 2 GHz. SAW devices have wide applications in the field of signal processing. These include delay lines, band pass filters, and oscillators.

The structure of a typical SAW delay line is shown in Fig. 3. It consists of two fingerlike electrodes known as inter digital transducers (IDTs) deposited on the surface of a suitable piezoelectric material as shown in Fig. 4. A sinusoidal voltage signal applied to transducer T_1 is converted into a surface acoustic wave, which travels along the surface of the substrate towards the output transducer T_2. The output transducer then converts the acoustic signal back to the electric signal. The time delay t_d between input and output signals is given by Eq. 2. In the case of surface acoustic wave devices, length of the delay medium is given by $L + L_1$, where L is the distance between the innermost edges of transducers and L_1 equals number of finger pairs N times periodicity p, and v is the velocity of surface acoustic waves.

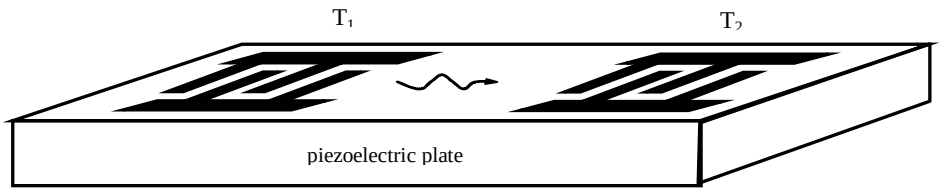

Fig. 3: Structure of a typical SAW delay line.

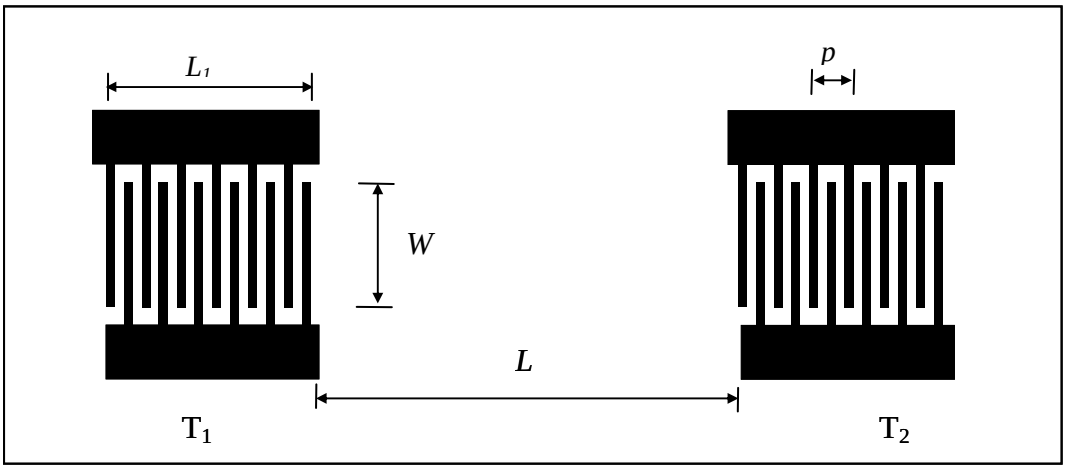

Fig. 4: Dimensions of IDTs deposited on the surface of a piezoelectric plate.

Plate Acoustic Waves propagate in plates of finite thickness. The thickness *h* of the plate is comparable to the wavelength λ of the acoustic wave. In 1917 H. Lamb showed that at a specified exciting frequency a finite number of plane sinusoidal waves could propagate in finite thickness plates [6]. The structure and device operation of PAW device is similar to that of a SAW device. The main difference is in the ratio of substrate thickness over wavelength. The ratio h/λ is much greater than 1 in SAW devices, whereas h/λ is comparable to 1 in PAW devices. There are three types of plate wave modes: anti symmetric (A), symmetric (S), and shear horizontal (SH) modes. A_0, SH_0, and S_0 are three all pass modes that have no cutoff frequency and propagate all the way down to $h/\lambda = 0$. That means, if a very thin plate with h/λ much less than 1 is used then only these three modes will propagate while the other higher order modes will be cut off.

Up until 1990s, many scientists had studied delay lines and signal processing devices based on plate acoustic waves for various applications [7-14]. However in all these works the ratio h/λ used was typically greater than three and work reported in these papers showed that many of the things that could be done with plate acoustic waves could also be done with SAW. Because of certain disadvantages in using the plate waves like dispersive characteristics of waves, presence of multiple modes, and need to have both surfaces freely supported, there was a situation when there was no interest in using plate waves in electronic applications. But later work done by White and his co-workers on plate waves generated on the substrate of thickness much less than λ has increased the use of PAW devices in sensor applications [15, 16]. At first the work done by White's group and many subsequent workers was limited to the anti symmetric A_0 plate wave mode and the substrate used was mostly silicon [17-20]. Later work done at Marquette University and elsewhere has shown that the other two fundamental plate wave modes, namely symmetric S_0 and shear horizontal SH_0, can also provide many important advantages for device applications [21-26].

1.2 Ultrasonic flow meters

The ultrasonic flow meter is an instrument that uses ultrasonic or acoustic waves to measure flow rate of fluids. Ultrasonic flow meters can be divided into transmission (or transit-time) meters and reflection (or Doppler) meters. Transmission flow meters are most commonly used ultrasonic flow meters. They are basically divided into two types [27]

- In-line flow meters (intrusive, wetted)

- Clamp-on flow meters (non-intrusive)

In in-line flow meters the transducers are placed on the inner walls of a pipe through which the fluid is flowing, whereas in clamp-on flow meters the transducers are mounted on the outside of the pipe wall. Transmission flow meters have two transducers mounted on each wall of the pipe through which the fluid is flowing. Acoustic waves generated by one transducer travel through the fluid and reach the other transducer. The time taken by the acoustic wave to travel from one transducer to the other, the transit time, is a function of the flow velocity of the fluid. Thus, by measuring this time, one can determine the fluid velocity and other relevant flow parameters.

Reflection flow meters require particulates or bubbles in the fluid flowing through the pipe. These flow meters are ideal for wastewater applications. Aeration would be required in clean liquid applications. The basic principle of operation employs the Doppler effect of an ultrasonic signal when it is reflected by suspended particles or gas bubbles. Two transducers are mounted in a case attached to one side of the pipe. A signal of known frequency is sent into the liquid to be measured. Solids, bubbles, or any discontinuity in the liquid, cause the pulse to be reflected to the receiver element. Because the liquid causing the reflection is moving, the frequency of the returned pulse is shifted. The frequency shift is proportional to the liquid's velocity.

The work described in this thesis is concerned with transmission type flow meters where the transducers are placed inside the pipe. The basic principle can be understood by referring to Fig. 5 which shows transducers *A* and *B* placed on opposite walls of a pipe. Let V denote velocity of the fluid flowing through the pipe and v_B denote the

velocity of bulk acoustic waves in the fluid. From Fig. 5 it can be shown that t_1, the transit time of acoustic waves to travel from *A* to *B*, is given by

$$t_1 = L/(v_B + Vcos\theta) \quad (3)$$

where *L* = acoustic path length between transducers *A* and *B*, and θ is the angle between the direction of acoustic wave propagation and the direction of fluid flow.

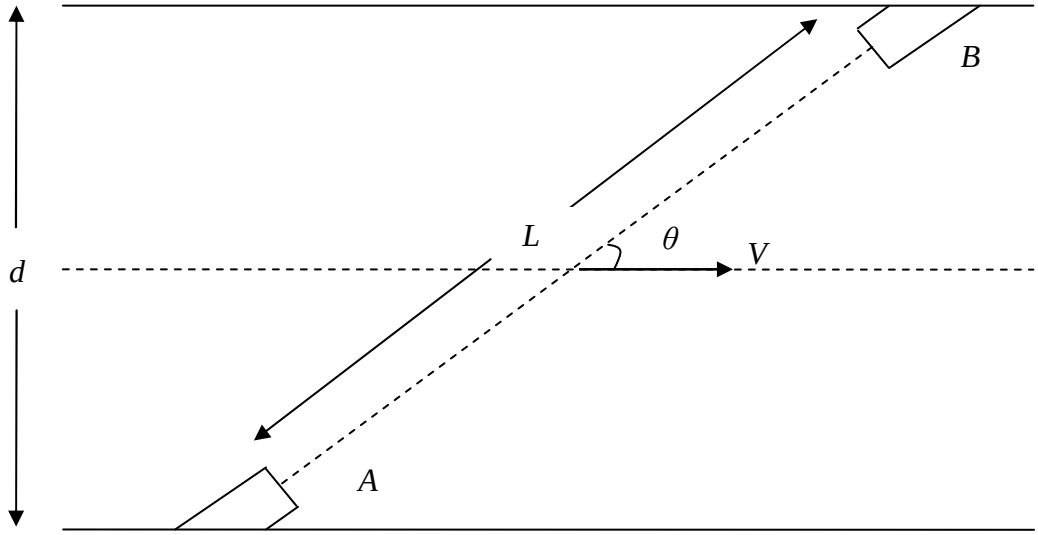

Fig. 5: Transmission type ultrasonic flow meter using wetted transducers.

The transit time of acoustic waves to travel from *B* to *A*, t_2 is given by

$$t_2 = L/(v_B - Vcos\theta) \quad (4)$$

Let us define a parameter $\alpha = (1/t_1 - 1/t_2)$. Substituting (3) and (4) in this equation we get

$$\alpha = 2VCos\theta/L \quad (5)$$

From Eq. (5) one can see that α is independent of $v_B$and depends only on fluid velocity V, angle θ and distance L. Thus by measuring the travel times t_1 and t_2, one can calculate α and from it the velocity of the flowing fluid.

One of the problems of currently available transducers is that they are generally large in size and protrude a considerable distance inward from the pipe wall and into the path of the flowing fluid. This causes several problems such as disturbance of flow stream resulting in erroneous flow data, fouling of transducer due to accumulation of rags, debris, etc. Prior work carried out in our laboratory has shown that a flat, planar transducer that has minimal protrusion into the pipe can be realized based on conversion of energy from surface acoustic waves (SAWs) to bulk acoustic waves (BAWs) and vice versa. This transducer, which operates by conversion of energy between surface and bulk waves, may be referred to as a mode conversion transducer (MCT). The structure of the MCT is shown in Fig. 6. It consists of a thin plate of a suitable piezoelectric material whose SAW velocity is greater than velocity of BAW in the fluid. It can be shown that under these conditions SAW propagating in the substrate will radiate a BAW in the fluid at an angle θ given by the equation $\theta = cos^{-1}(v_B/v_s)$, where v_B= BAW velocity in the fluid, and v_s= SAW velocity in the substrate. A similar device can be used on the other wall of the pipe. Here bulk wave incident from the fluid will generate SAW on the substrate.

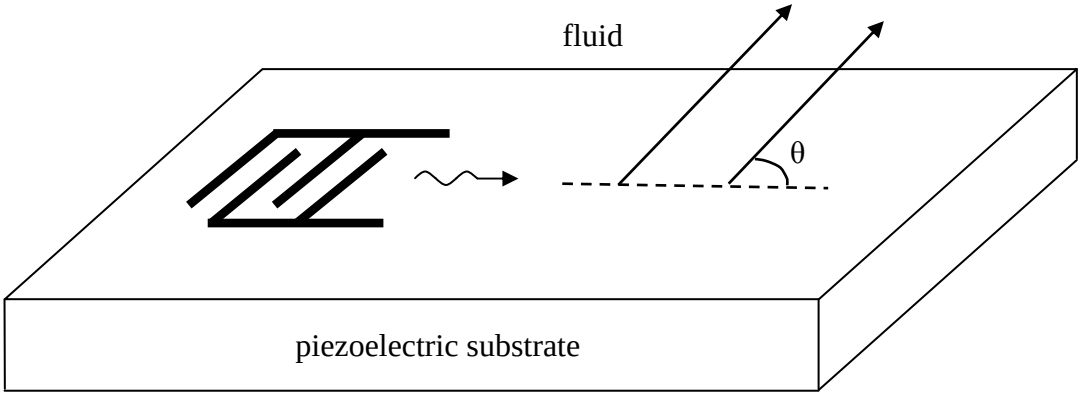

Fig. 6: Geometry of a mode conversion transducer. Surface acoustic wave propagating on the substrate radiates bulk acoustic wave in the fluid.

The question that we wish to answer is whether a similar transducer can be realized based on the conversion of energy from plate acoustic waves (PAWs) to bulk acoustic waves. In order to determine whether a plate acoustic wave can couple energy efficiently to a bulk acoustic wave, we need to analyze the propagation of acoustic waves in the presence of a fluid medium contacting the propagation surface. This subject is discussed in the next chapter.

Chapter 2

Propagation of plate acoustic waves in contact with a fluid medium

This chapter is concerned with the analysis of acoustic waves propagating in a piezoelectric substrate which is in contact with a fluid medium. The geometry of the problem under consideration is shown in Fig. 7. Acoustic waves propagate along the x_1 axis of a piezoelectric plate bounded by the planes $x_3 = 0$ and $x_3 = h$. The fluid occupies the region $x_3 < 0$, while the region $x_3 > h$ is free space. We consider a two-dimensional problem in which all field components are assumed to be constant in the x_2 direction.

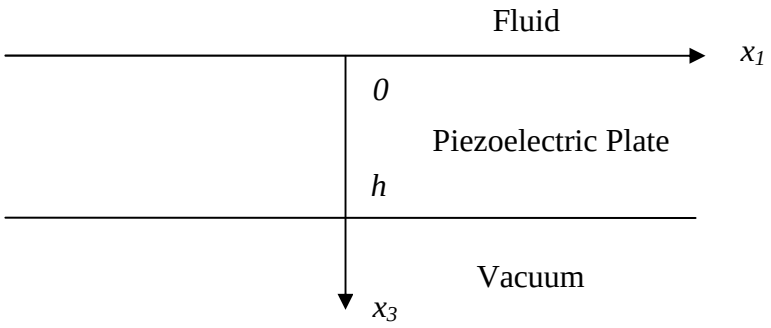

Fig. 7: Geometry of the problem used to analyze propagation of plate acoustic waves in contact with a fluid medium.

The analysis of this problem consists of solving the equations of motion subject to the appropriate boundary conditions. First, consider the piezoelectric plate. The equations of state for a piezoelectric medium are given by

$$T_{ij} = C_{ijkl}S_{kl} - e_{kij}E_k \tag{6}$$

$$D_i = e_{ijk}S_{jk} + \varepsilon_{ij}E_j \tag{7}$$

where T_{ij} are components of stress tensor, C_{ijkl} are the elastic constants, e_{ijk} are piezoelectric constants, D_i is the electric displacement, E_i is the electric field intensity,

and ε_{ij} are the components of permittivity tensor. The components of strain tensor S_{kl} are defined by

$$S_{kl} = \frac{1}{2}\left[\frac{\partial u_k}{\partial x_l} + \frac{\partial u_l}{\partial x_k}\right] \tag{8}$$

where u_i are components of particle displacement.

The equations of motion in the piezoelectric plate are given by

$$\rho \frac{\partial^2 u_i}{\partial t^2} = \frac{\partial T_{ij}}{\partial x_j} \tag{9}$$

where ρ is the density of the piezoelectric plate.

Gauss's Law in the piezoelectric plate is given by

$$\frac{\partial D_i}{\partial x_i} = 0 \tag{10}$$

The relation between electrostatic potential ϕ and electric field is given by

$$E_k = -\frac{\partial \phi}{\partial x_k} \tag{11}$$

Substituting Eq. (8) and (11) into Eq. (6), and using Eq. (9), we get

$$\rho \frac{\partial^2 u_i}{\partial t^2} = C_{ijkl} \frac{\partial^2 u_k}{\partial x_j \partial x_l} + e_{kij} \frac{\partial^2 \phi}{\partial x_j \partial x_k} \tag{12}$$

Substituting Eq. (8) and (11) into Eq. (7), and using Eq. (10), we get

$$\varepsilon_{ij} \frac{\partial^2 \phi}{\partial x_i \partial x_j} - e_{ikj} \frac{\partial^2 u_k}{\partial x_j \partial x_i} = 0 \tag{13}$$

Eqs. (12) and (13) are the equations of motion in the piezoelectric plate.

We assume solutions of the form

$$u_i = B_i\, e^{jbkx_3}\, e^{jk(x_1 - vt)} \qquad i = 1, 2, 3 \tag{14}$$

$$\phi = B_4 e^{jbkx_3}\, e^{jk(x_1 - vt)} \tag{15}$$

where B_i denotes complex amplitude of particle displacement u and potential ϕ, $k = \omega/v$ is the wave number, v is the velocity of the wave and b is the decay constant of the wave in the x_3 direction. Substituting Eq. (14) and (15) in Eq. (12) and (13), four homogeneous equations can be written in the following form

$$\begin{bmatrix} \Gamma_{11} - \rho v^2 & \Gamma_{12} & \Gamma_{13} & \Gamma_{14} \\ \Gamma_{21} & \Gamma_{22} - \rho v^2 & \Gamma_{23} & \Gamma_{24} \\ \Gamma_{31} & \Gamma_{32} & \Gamma_{33} - \rho v^2 & \Gamma_{34} \\ \Gamma_{41} & \Gamma_{42} & \Gamma_{43} & \Gamma_{44} \end{bmatrix} \begin{bmatrix} B_1 \\ B_2 \\ B_3 \\ B_4 \end{bmatrix} = 0 \tag{16}$$

Here Γ is a symmetric matrix whose elements are given by

$$\Gamma_{ij} = C_{3i3j}b^2 + \left(C_{1i3j} + C_{3i1j}\right)b + C_{1i1j} \tag{17}$$

$$\Gamma_{i4} = e_{3i3}b^2 + (e_{1i3} + e_{3i1})b + e_{1i1} \tag{18}$$

$$\Gamma_{44} = -[\varepsilon_{33}b^2 + (\varepsilon_{13} + \varepsilon_{31})b + \varepsilon_{11}] \tag{19}$$

To obtain a non-trivial solution for vector B it is required that the determinant of Γ matrix in Eq. (16) be equal to zero. This condition results in an eighth order equation in decay constant b with coefficients A_0 through A_8 that are functions of material constants and velocity v.

$$A_8b^8 + A_7b^7 + A_6b^6 + A_5b^5 + A_4b^4 + A_3b^3 + A_2b^2 + A_1b + A_0 = 0 \tag{20}$$

Eq. (20) gives eight roots for decay constant b. For every value of b, there are eight four component eigenvectors $B_n = (B_{1n}, B_{2n}, B_{3n}, B_{4n})$, $n = 1, 2, \ldots\ldots, 8$, corresponding to the

eight solutions b_n. Since for each b_n and associated eigenvector B_n, the corresponding solutions given in Eqs. (14) and (15) satisfy the equations of motion, a linear combination of all the allowed solutions will also satisfy these equations. Thus the general solution can be written as

$$u_i = \left(\sum_{n=1}^{8} W_n B_{in} e^{jb_n k x_3} \right) e^{jk(x_1 - vt)} \quad i = 1, 2, 3 \tag{21}$$

$$\phi = \left(\sum_{n=1}^{8} W_n B_{4n} e^{jb_n k x_3} \right) e^{jk(x_1 - vt)} \tag{22}$$

where W_n are the weighting coefficients.

Next, we consider the situation in the fluid. For a non-conducting, non-viscous fluid the elastic constant matrix has the following simple form

$$\begin{bmatrix} C^f & C^f & C^f & 0 & 0 & 0 \\ C^f & C^f & C^f & 0 & 0 & 0 \\ C^f & C^f & C^f & 0 & 0 & 0 \\ 0 & 0 & 0 & 0 & 0 & 0 \\ 0 & 0 & 0 & 0 & 0 & 0 \\ 0 & 0 & 0 & 0 & 0 & 0 \end{bmatrix} \tag{23}$$

Equation of motion in the fluid is given by

$$\rho^f \frac{\partial^2 u_i^f}{\partial t^2} = \frac{\partial T_{ij}^f}{\partial x_j} \tag{24}$$

Gauss's Law is given by

$$\frac{\partial D_i^f}{\partial x_i} = 0 \tag{25}$$

Electric field intensity is given by

$$E_i^f = -\frac{\partial \phi^f}{\partial x_i} \tag{26}$$

Mechanical stress and electric displacement are given by

$$T_{ij}^f = C_{ijkl}^f S_{kl}^f \tag{27}$$

$$D_i^f = -\varepsilon_{ij}^f \frac{\partial \phi^f}{\partial x_j} \tag{28}$$

where parameters have their usual meanings as defined in Eqs. (6) through (11) but the superscript f indicates that these are defined in the fluid medium.

Assume solutions of the form

$$u_1^f = W_{11} e^{jb_f k x_3} e^{jk(x_1 - vt)} \tag{29}$$

$$u_3^f = W_{10} e^{jb_f k x_3} e^{jk(x_1 - vt)} \tag{30}$$

$$\phi^f = W_9 e^{jb_f k x_3} e^{jk(x_1 - vt)} \tag{31}$$

where b_f is the decay constant in the x_3 direction.

Partial differentiation of Eqs. (29) through (31) gives

$$\begin{aligned} \frac{\partial^2}{\partial x_1^2} &= -k^2 \\ \frac{\partial^2}{\partial x_3^2} &= -k^2 b_f^2 \\ \frac{\partial^2}{\partial x_1 \partial x_3} &= -k^2 b_f \\ \frac{\partial^2}{\partial t^2} &= -k^2 v^2 \end{aligned} \tag{32}$$

Substituting Eq. (27) into Eq. (24), and using Eq. (29) and (30), we get

$$C^f \left(\frac{\partial^2 u_1^f}{\partial x_1^2} + \frac{\partial^2 u_3^f}{\partial x_1 \partial x_3} \right) = \rho^f \frac{\partial^2 u_1^f}{\partial t^2} \tag{33}$$

$$C^f\left(\frac{\partial^2 u_1^f}{\partial x_1 \partial x_3}+\frac{\partial^2 u_3^f}{\partial x_3^2}\right)=\rho^f\frac{\partial^2 u_3^f}{\partial t^2} \tag{34}$$

Solving Eqs. (33) and (34) using Eq. (32), we get a 2×2 matrix as shown below

$$\begin{bmatrix} C^f-\rho^f v^2 & C^f b_f \\ C^f b_f & C^f b_f^2-\rho^f v^2 \end{bmatrix}\begin{bmatrix} W_{11} \\ W_{10} \end{bmatrix}=0 \tag{35}$$

To obtain a non-trivial solution for $W_{11}$and W_{10}, it is required that the determinant of the matrix should be equal to zero. This condition gives

$$b_f=\pm\sqrt{\frac{\rho^f v^2-C^f}{C^f}} \tag{36}$$

Also we can write from Eq. (35) that

$$W_{11}=\frac{\rho^f v^2-C^f b_f^2}{C^f b_f}\,W_{10} \tag{37}$$

and Eq. (27) can be written as

$$T_{33}^f=C^f\left(\frac{\partial u_1^f}{\partial x_1}+\frac{\partial u_3^f}{\partial x_3}\right) \tag{38}$$

Partial differentiation of Eq. (29) with respect to x_1 and Eq. (30) with respect to x_3 gives

$$\begin{aligned} \frac{\partial u_1^f}{\partial x_1}&=jkW_{11} \\ \frac{\partial u_3^f}{\partial x_3}&=jkb_fW_{10} \end{aligned} \tag{39}$$

Substituting Eq. (39) in Eq. (38), and using Eq. (37), we get

$$T_{33}^f=jk\left(\frac{\rho^f v^2}{b_f}\right)W_{10} \tag{40}$$

Finally, in free space *($x_3 > h$)*, the relationship between electric displacement and electric field intensity is given by

$$D_i^v = -\varepsilon_0 \frac{\partial \phi^v}{\partial x_i} \tag{41}$$

where D_i^v, ϕ^v and ε_0 are the electric displacement, electric potential and the permittivity in free space.

2.1 Boundary Conditions

The boundary conditions on the problem are as follows. At the plate-fluid interface (plane $x_3 = 0$), the normal component of particle displacement u_3, electric potential ϕ, normal component of flux density D_3, and stress component normal to the surface T_{33}, are continuous; whereas the shear stress components T_{31} and T_{32} are zero. Thus, the boundary conditions at $x_3 = 0$ are [28]:

$$\begin{aligned} u_3^f &= u_3 \text{ ;} \\ \phi^f &= \phi \text{ ;} \\ D_{33}^f &= D_3\text{;} \\ T_{33}^f &= T_{33} \text{ ; and} \\ T_{31} &= T_{32} = 0. \end{aligned} \tag{42}$$

At the plate vacuum interface (plane $x_3 = h$), the mechanical boundary conditions are that the stress components T_{31}, T_{32}, and T_{33} are zero and the electrical boundary conditions are that potential and normal component of flux density are continuous.

$$\begin{aligned} T_{31} &= T_{32} = T_{33} = 0 \text{ ;} \\ \phi^v &= \phi \text{ ; and} \\ D_3^v &= D_3. \end{aligned} \tag{43}$$

Application of the above boundary conditions to the assumed field solutions leads to a set of ten homogenous equations in the ten unknown amplitudes W_n ($n = 1, 2,\ldots, 10$).

Expanding the tensor notations for respective tensor terms in Eq. (42) and substituting $x_3 = 0$, we get six equations as follows,

$$W_1B_{31} + W_2B_{32} + W_3B_{33} + W_4B_{34} + W_5B_{35} + W_6B_{36} + W_7B_{37} + W_8B_{38} - W_{10} = 0 \quad (44)$$

$$W_1B_{41} + W_2B_{42} + W_3B_{43} + W_4B_{44} + W_5B_{45} + W_6B_{46} + W_7B_{47} + W_8B_{48} - W_9 = 0 \quad (45)$$

$$W_n\{B_{1n}(e_{311} + e_{313}b_n) + B_{2n}(e_{321} + e_{323}b_n) + B_{3n}(e_{331} + e_{333}b_n) - B_{4n}(\varepsilon_{13} + \varepsilon_{33}b_n)\} - W_9 j\varepsilon^f = 0 \quad (46)$$

$$W_n\{B_{1n}(C_{3311} + C_{3313}b_n) + B_{2n}(C_{3321} + C_{3323}b_n) + B_{3n}(C_{3331} + C_{3333}b_n) + B_{4n}(e_{133} + e_{333}b_n)\} - W_{10}\frac{\rho^f v^2}{b_f} = 0 \quad (47)$$

$$W_n\{B_{1n}(C_{3111} + C_{3113}b_n) + B_{2n}(C_{3121} + C_{3123}b_n) + B_{3n}(C_{3131} + C_{3133}b_n) + B_{4n}(e_{131} + e_{331}b_n)\} = 0 \quad (48)$$

$$W_n\{B_{1n}(C_{3211} + C_{3213}b_n) + B_{2n}(C_{3221} + C_{3223}b_n) + B_{3n}(C_{3231} + C_{3233}b_n) + B_{4n}(e_{132} + e_{332}b_n)\} = 0 \quad (49)$$

Expanding the tensor notations for respective tensor terms in Eq. (43) and substituting $x_3 = h$, we get four equations as follows,

$$W_n\{B_{1n}(C_{3111} + C_{3113}b_n) + B_{2n}(C_{3121} + C_{3123}b_n) + B_{3n}(C_{3131} + C_{3133}b_n) + B_{4n}(e_{131} + e_{331}b_n)\}e^{jb_nkh} = 0 \quad (50)$$

$$W_n\{B_{1n}(C_{3211} + C_{3213}b_n) + B_{2n}(C_{3221} + C_{3223}b_n) + B_{3n}(C_{3231} + C_{3233}b_n) + B_{4n}(e_{132} + e_{332}b_n)\}e^{jb_nkh} = 0 \quad (51)$$

$$W_n\{B_{1n}(C_{3311} + C_{3313}b_n) + B_{2n}(C_{3321} + C_{3323}b_n) + B_{3n}(C_{3331} + C_{3333}b_n) + B_{4n}(e_{133} + e_{333}b_n)\}e^{jb_nkh} = 0 \quad (52)$$

$$W_n\{B_{1n}(e_{311}+e_{313}b_n)+B_{2n}(e_{321}+e_{323}b_n)+B_{3n}(e_{331}+e_{333}b_n)- B_{4n}(\varepsilon_{13}+\varepsilon_{33}b_n-j\varepsilon_0)\}e^{jb_nkh}=0 \quad (53)$$

2.2 Modifying a 10×10 boundary condition matrix into an 8×8 matrix

Equations (44) through (53) gives us a 10×10 boundary condition matrix. We can see from the above ten equations that only Eq. (44) and Eq. (47) has terms in W_{10}, and Eq. (45) and Eq. (46) has terms in W_9. By suitable modification, we can reduce this 10×10 matrix to an 8×8 matrix and that work is explained below.

From Eq. (45), we get

$$W_9=W_1B_{41}+W_2B_{42}+W_3B_{43}+W_4B_{44}+W_5B_{45}+W_6B_{46}+W_7B_{47}+W_8B_{48} \quad (54)$$

Substituting Eq. (54) for W_9 in Eq. (46), we get

$$W_n\{B_{1n}(e_{311}+e_{313}b_n)+B_{2n}(e_{321}+e_{323}b_n)+B_{3n}(e_{331}+e_{333}b_n)- B_{4n}(\varepsilon_{13}+\varepsilon_{33}b_n+j\varepsilon^f)\}=0 \quad (55)$$

From Eq. (44), we get

$$W_{10}=W_1B_{31}+W_2B_{32}+W_3B_{33}+W_4B_{34}+W_5B_{35}+W_6B_{36}+W_7B_{37}+W_8B_{38} \quad (56)$$

Substituting Eq. (56) for W_{10} in Eq. (47), we get

$$W_n\left\{B_{1n}(C_{3311}+C_{3313}b_n)+B_{2n}(C_{3321}+C_{3323}b_n)+B_{3n}\left(C_{3331}+C_{3333}b_n-\frac{\rho^f v^2}{b_f}\right)+B_{4n}(e_{133}+e_{333}b_n)\right\}=0 \quad (57)$$

By writing Equations (48), (49), (57), (55), and (50) through (53) in order, we get a set of eight homogenous algebraic equations for the eight weighting coefficients. Note that these equations do not have any terms in W_9 and W_{10}. These modified equations can be written in the form

$$[P_{mn}][W_n] = 0 \tag{58}$$

where $[W]$ is a column vector with components $(W_1, W_2 \ldots, W_8)$, and the boundary condition matrix $[P]$ is an 8×8 matrix whose components are given by

$$P_{in} = (C_{3ik1} + C_{3ik3}b_n)B_{kn} + (e_{13i} + e_{33i}b_n)B_{4n} \qquad i = 1, 2$$

$$P_{3n} = (C_{3311} + C_{3313}b_n)B_{1n} + (C_{3321} + C_{3323}b_n)B_{2n} + \left(C_{3331} + C_{3333}b_n - \frac{\rho^f v^2}{b_f}\right)B_{3n} + (e_{133} + e_{333}b_n)B_{4n}$$

$$P_{4n} = (e_{3k1} + e_{3k3}b_n)B_{kn} - (\varepsilon_{13} + \varepsilon_{33}b_n + j\varepsilon^f)B_{4n}$$

$$P_{5n} = P_{1n}e^{jb_nkh}$$

$$P_{6n} = P_{2n}e^{jb_nkh}$$

$$P_{7n} = (C_{3311} + C_{3313}b_n)B_{1n} + (C_{3321} + C_{3323}b_n)B_{2n} + (C_{3331} + C_{3333}b_n)B_{3n} + (e_{133} + e_{333}b_n)B_{4n}, \text{ and}$$

$$P_{8n} = (e_{3k1} + e_{3k3}b_n)B_{kn} - (\varepsilon_{13} + \varepsilon_{33}b_n - j\varepsilon_0)B_{4n}$$

where subscript *n* ranges from 1 through 8 and *k* ranges from 1 to 3.

To obtain a non-trivial solution for the weighting coefficients *W*, the determinant of the boundary condition matrix $[P_{mn}]$ should be equal to zero. Thus the velocity of the propagating plate wave is found by searching for value of *v* that simultaneously makes the determinant of the Γ matrix (Eq. 16) and determinant of the P_{mn} matrix (Eq. 58) equal to zero. In the Γ matrix, there are two unknown variables, namely wave velocity *v* and decay constant *b*. This decay constant is also a variable in the *P* matrix. Thus to solve this kind of complex problem we use numerical method. In numerical method, the decay constant *b* and its eigenvectors *B* are calculated for an assumed velocity. And then, these calculated values are substituted to find the determinant of the boundary condition matrix *P*. This iterating process is repeated till the minimum value of |P| is obtained. The correct

velocity gives minimum |P| value for a chosen h/λ ratio. The velocity v depends on various parameters such as the type of the substrate, its thickness, wavelength, crystal orientation, and direction of propagation. Thus we need to specify these parameters in the computer program.

2.3 Flowchart and programming procedure to calculate plate wave velocity

The flowchart of the Matlab program to find the wave velocity for the case of a substrate in contact with the fluid on one side and free space on the other side is given below in Fig. 8. The program finds values of |P| for iterated velocities to locate the minima in the |P| versus velocity plot. The description of the main steps in the program is as follows.

1. Material constants c, e, ε, and ρ of the piezoelectric plate, c^f, ε^f and ρ^f of the fluid, permittivity of the free space ε_o, ratio of plate thickness and acoustic wavelength h/λ (or h in program), and Euler angles λ, μ, and θ are entered directly in program.
2. Rotated material constants of the piezoelectric plate are calculated and they will be used onwards in the program.
3. The range of h is defined.
4. A search velocity range is defined.

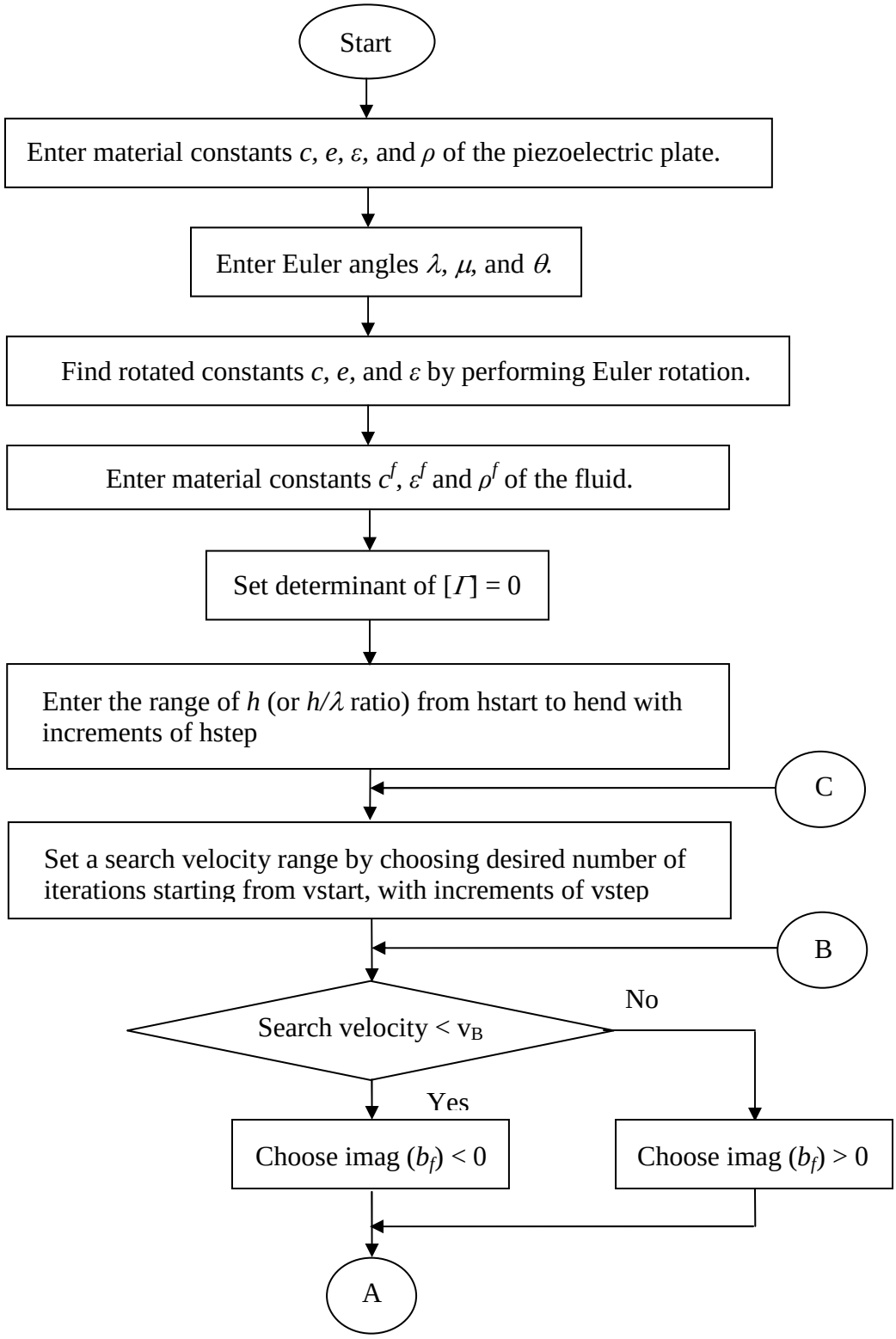

Fig. 8: Flowchart to calculate plate acoustic wave velocity.

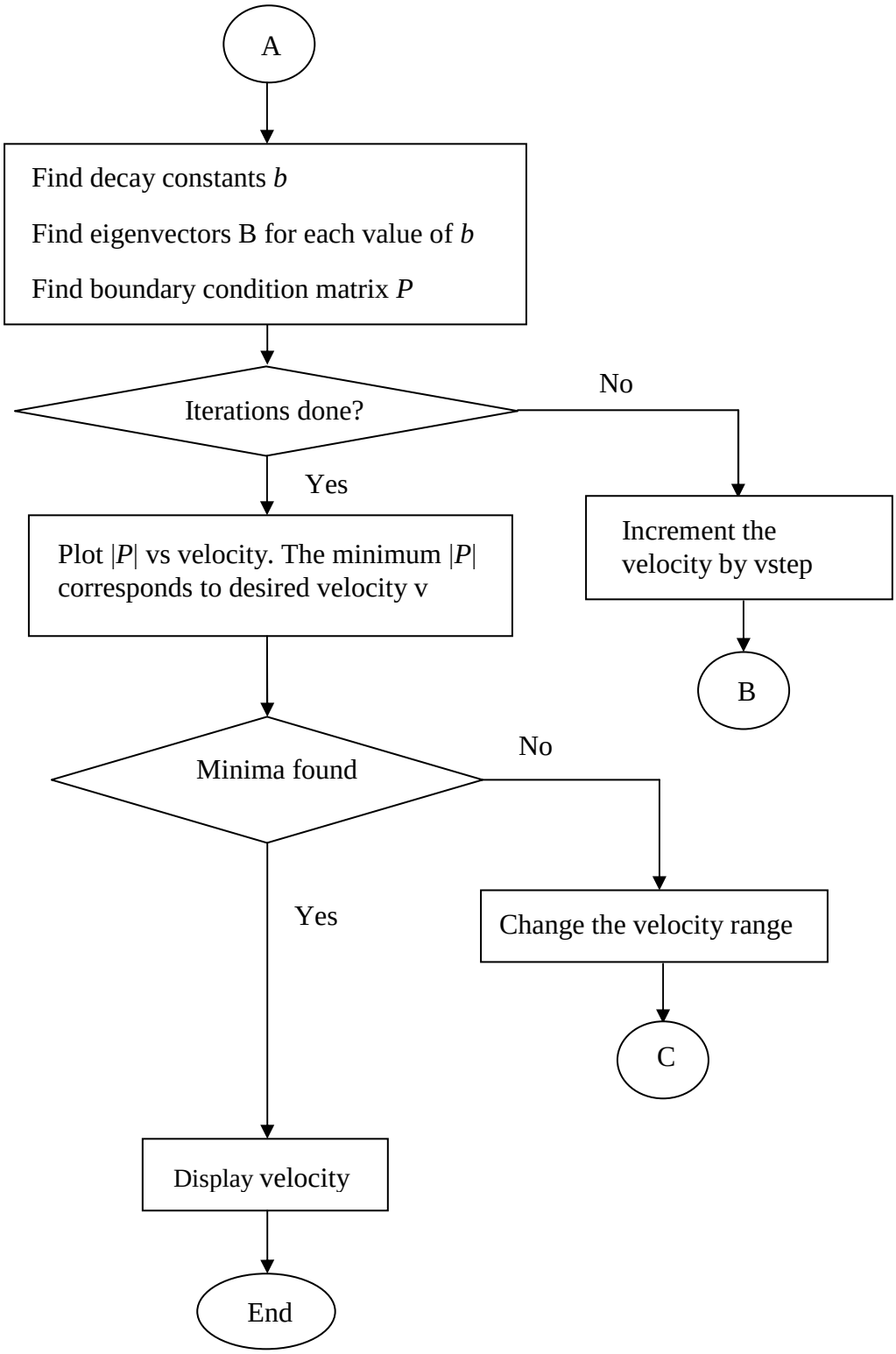

Fig. 8 (Continued): Flowchart to calculate plate acoustic wave velocity.

5. Consider a case where search velocity range is less than velocity of bulk wave in the fluid v_B. In this case real velocity search has to be done. Let us say for given plate velocity the complex decay constant $b_f = b_f^R + jb_f^I$. From Eqs. (29) through (31) $e^{jb_f kx_3}$ factor can be written as

$$e^{j(b_f^R + jb_f^I)kx_3} = e^{jb_f^R kx_3}.e^{-b_f^I kx_3} \quad (59)$$

For $x_3 < 0$, Eq. (59) will become $e^{-jb_f^R kx_3}.e^{b_f^I kx_3}$ and since plate wave should decay in the fluid therefore b_fs with negative imaginary part should be chosen. Fig. 9 is one such example of real velocity search for 128 Y-X lithium niobate at h/λ = 0.16.

6. For search velocity range greater than v_B, complex velocity search has to be done. In this case amplitude of the wave should increase in the fluid and therefore b_f s with positive imaginary parts should be chosen.
7. The components of Γ matrix are defined using Eqs. (17) through (19) and its determinant is calculated. This matrix has decay constant *b* as unknown variable.
8. Decay constants *b* and their corresponding eigenvectors *B* are calculated.
9. The determinant of *P* matrix is calculated. Minima of |P| which are possible solutions of velocity are searched. The minimum with correct velocity has low value of |P| and its velocity changes with h/λ (or *h* in program).
10. Decay constants *b* and their corresponding eigenvectors *B* are calculated for the velocity found in step 9.

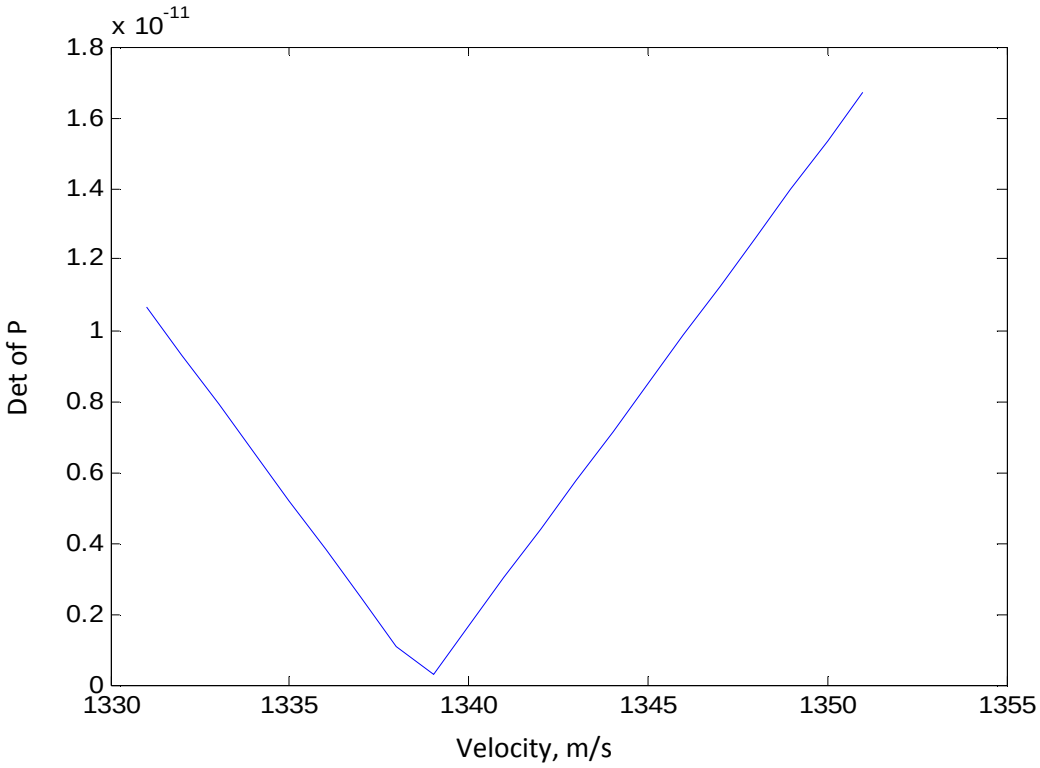

Fig. 9: Iterative search for real velocity, where the search velocity range is less than v_B.

The reason for searching complex velocity in the program for v_p greater than v_B is as follows. If the velocity of plate wave in the substrate is greater than velocity of bulk wave in the fluid, then a PAW propagating in the substrate will radiate a BAW in the fluid. Due to this radiation, the plate wave will suffer attenuation. The attenuation of the wave is accounted for by the imaginary part of the complex velocity. The attenuation coefficient α is a measure of radiation or conversion efficiency. In this case, the radiation or conversion efficiency means the ability of plate wave to radiate a bulk wave in the fluid.

From Appendix B, the attenuation per unit acoustic wavelength can be written as

$$\alpha = 54.58(v^I/v^R) \;\; dB/\lambda \tag{60}$$

where v^R and v^I are the real and imaginary parts of the complex velocity. Thus the velocity has to be complex for the attenuation to occur. Therefore it is necessary to find both the real and imaginary parts of the velocity which requires iterative search procedures for each case. First, the minimum |P| is found by searching for purely real part of velocity as shown in Fig. 10. A particular case of 128 Y-X lithium niobate which is in contact with water on one of its surfaces with h/λ = 0.4 has been considered. The real part of the velocity was found to be 2861 m/s. Now considering this real part, iterative search for imaginary part is done as shown in Fig. 11. The imaginary part of the velocity was found out to be 64 m/s. So, the final velocity *v* is equal to (2861 + i64) m/s. From this, we get that the attenuation per unit wavelength will be

$$\alpha = 54.58(64/2861)$$

$$= 1.22\, dB/\lambda.$$

With h/λ = 0.21, the iterative search (both real and imaginary parts of velocity) for the above considered case was carried out as shown in Fig. 12 and 13. For the final velocity obtained that is *v* = (1968 + i167) m/s, the attenuation per unit wavelength was found to be 4.63 dB/λ. One can see that as the h/λ ratio decreases, the real part of the complex velocity decreases and the imaginary part increases, thus increasing the attenuation or the efficiency of plate wave to generate a bulk wave in fluid.

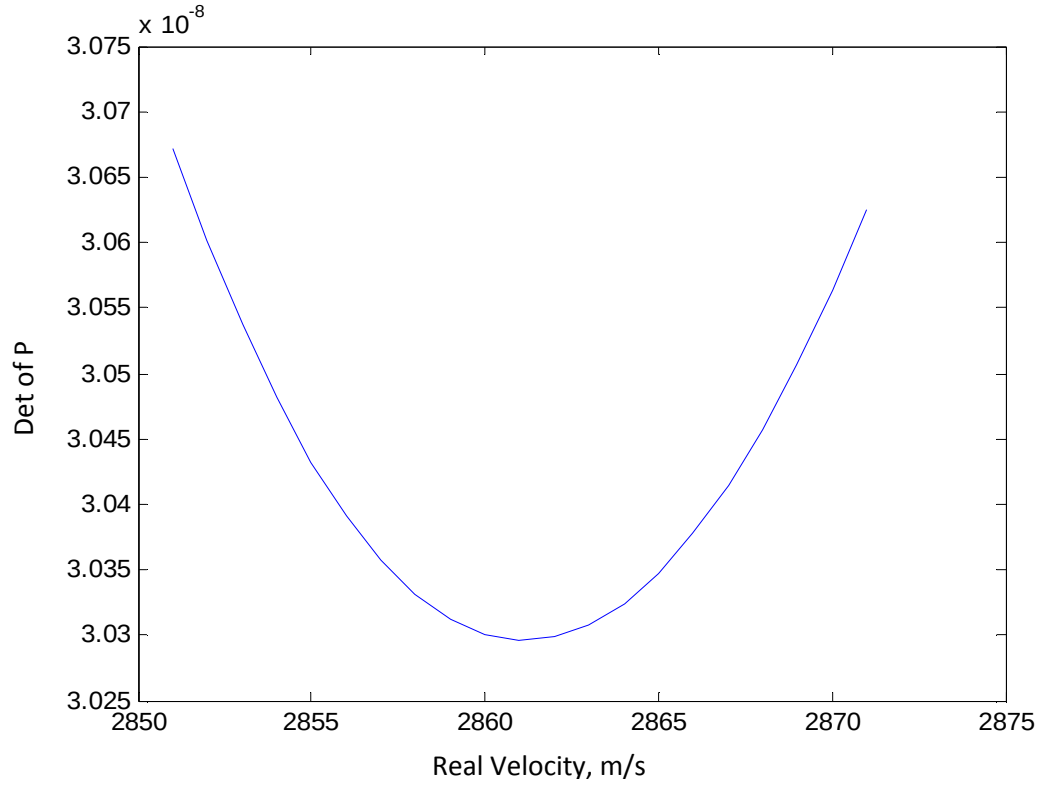

Fig. 10: Iterative search for real part of the velocity for $h/\lambda = 0.4$.

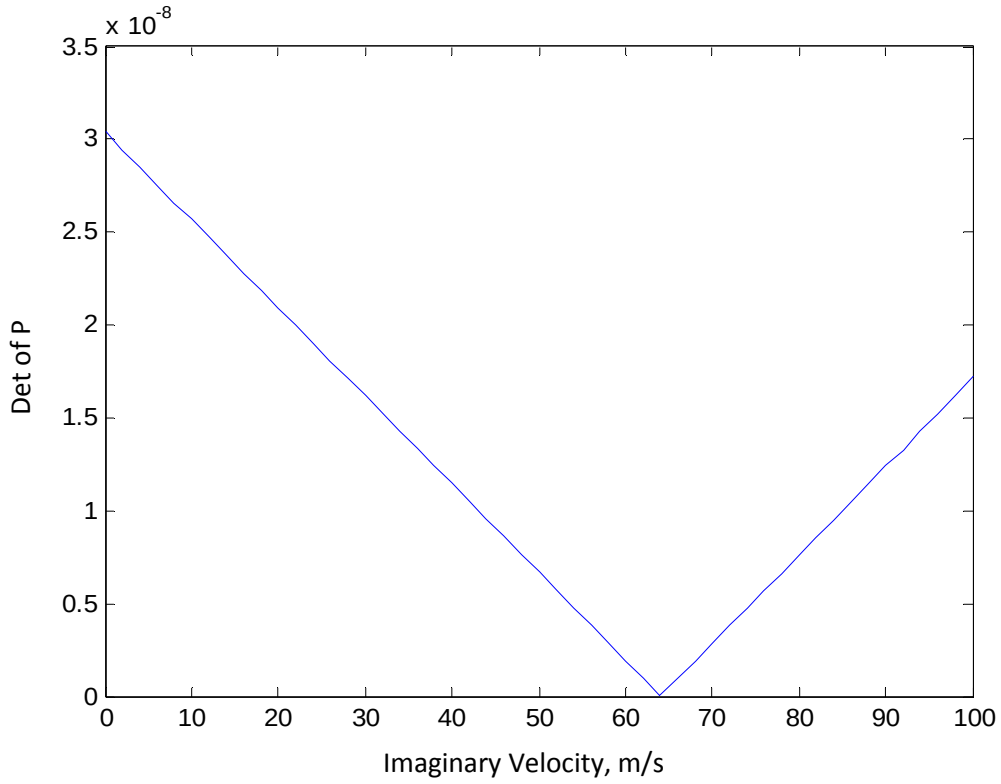

Fig. 11: Iterative search for imaginary part of the velocity for $h/\lambda = 0.4$.

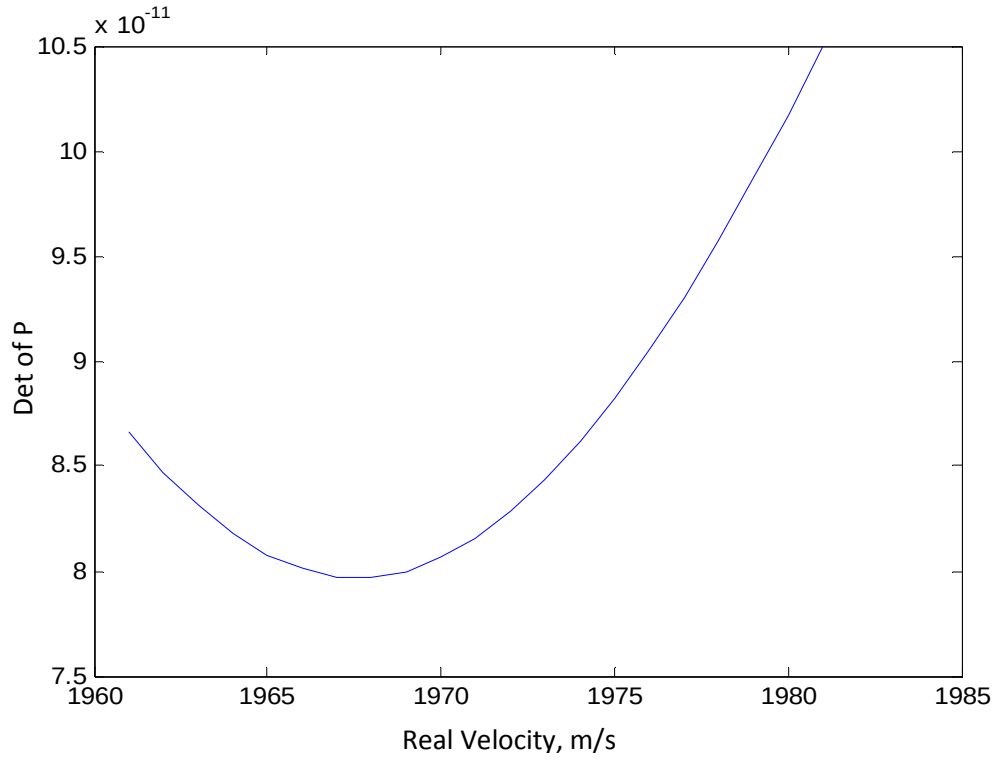

Fig. 12: Iterative search for real part of the velocity for $h/\lambda = 0.21$.

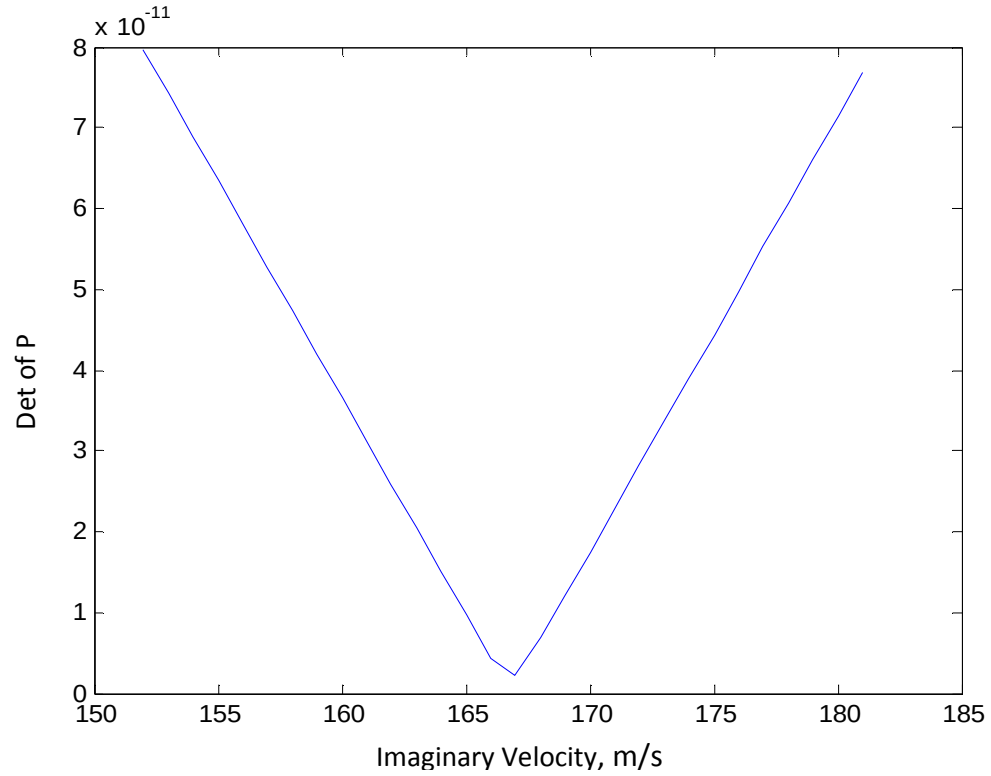

Fig. 13: Iterative search for imaginary part of the velocity for $h/\lambda = 0.21$.

For a 128 Y-X lithium niobate plate, which is in contact with water on one of its surfaces, pure real velocity search (for plate wave velocity v_p less than v_B) and complex velocity search (for v_p greater than v_B), for different values of h/λ was carried out. Fig. 14(a) shows the calculated results for the plate wave velocity versus product *hf*, where *h* is the thickness of the plate and *f* is the acoustic frequency. One can see that the velocity of the plate wave increases as *hf* increases, then it exhibits a jump at the point where the sign of decay constant b_f changes, that is, at $hf \approx 220$ m/s. Dotted line in Fig. 14(a) shows velocity in the absence of water loading that is, free space on both sides of the piezoelectric plate. Fig. 14(b) shows the calculated results for the attenuation versus product *hf*. The velocity of bulk acoustic waves in water v_B is approximately 1500 m/s. The velocity v_p of the plate wave becomes equal to v_B at $hf \approx 220$ m/s. For *hf* less than 220 m/s, v_p is less than v_B, whereas for *hf* greater than 220 m/s, v_p becomes greater than v_B. The plate wave will not radiate energy in the water, and hence not suffer any attenuation, when its velocity is less than v_B ($hf \leq 220$ m/s). On the other hand when v_p becomes greater than v_B ($hf \geq 220$ m/s) then the plate wave will radiate bulk wave in the water and therefore suffer attenuation. Fig. 14(b) shows that attenuation coefficient greater than 2 dB per wavelength can be obtained for values of *hf* lying between 220 and 750 m/s. Such large values of attenuation coefficient indicate that there is strong coupling between the plate wave mode and bulk acoustic wave propagating in water.

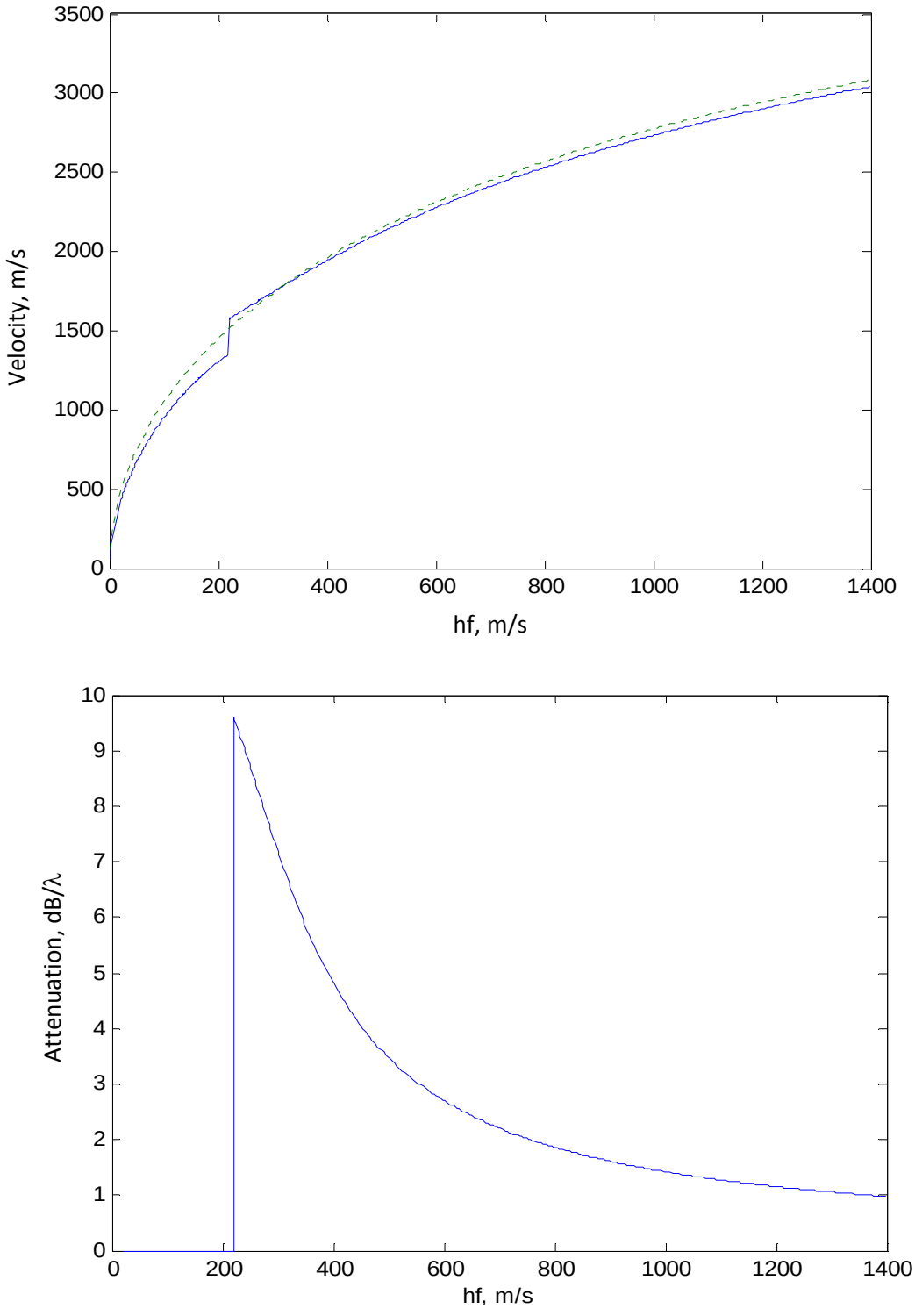

Fig. 14: Velocity (a) and attenuation per wavelength (b) for plate waves propagating in a 128 Y-X lithium niobate plate in the presence of water contacting one of the plate surfaces.

The water loading effect on two other widely used substrates, namely quartz and lithium tantalate, has also been studied. Fig. 15(a) shows the calculated results of plate wave velocity versus product *hf* for X-Y+10 quartz which is in contact with water on one of its surfaces. Fig. 15(b) shows the plot for attenuation coefficient versus *hf*. In this case, the plate wave will not radiate a bulk wave in water for $hf \leq 291$ m/s. Attenuation coefficient as high as 12 dB/λ was obtained at $hf = 291$ m/s. One can see that the attenuation coefficient of minimum 2 dB/λ can be obtained for wide range of *hf* values from $hf = 291$ m/s to 1350 m/s.

Fig. 16(a) shows the calculated results of plate wave velocity versus product *hf* for Y-Z lithium tantalate which is in contact with water on one of its surfaces. In this case, the plate wave will not radiate a bulk wave in water for $hf \leq 259$ m/s. In this case, the maximum attenuation coefficient obtained was 5.91 dB/λ at $hf = 259$ m/s as shown in Fig. 16(b). Attenuation coefficient greater than 2 dB per wavelength can be obtained for values of *hf* lying between 259 and 505 m/s.

It has been stated in chapter 1 that one has a wider choice of substrate materials by using plate waves. The reason for this is as follows. Suppose that the fluid flowing in the pipe is water. Then $v_B \approx 1500$ m/s, and to obtain the optimum value of $\theta = 45^0$, the velocity of acoustic wave in the substrate should be $1500/(\cos\theta) = 2120$ m/s. But the velocity of SAWs in widely used substrate materials such as quartz, lithium niobate, lithium tantalate, etc. is in the range of 3200 to 3900 m/s. But for plate waves, the desired velocity can be obtained in these materials by using a suitable value of the product *hf*.

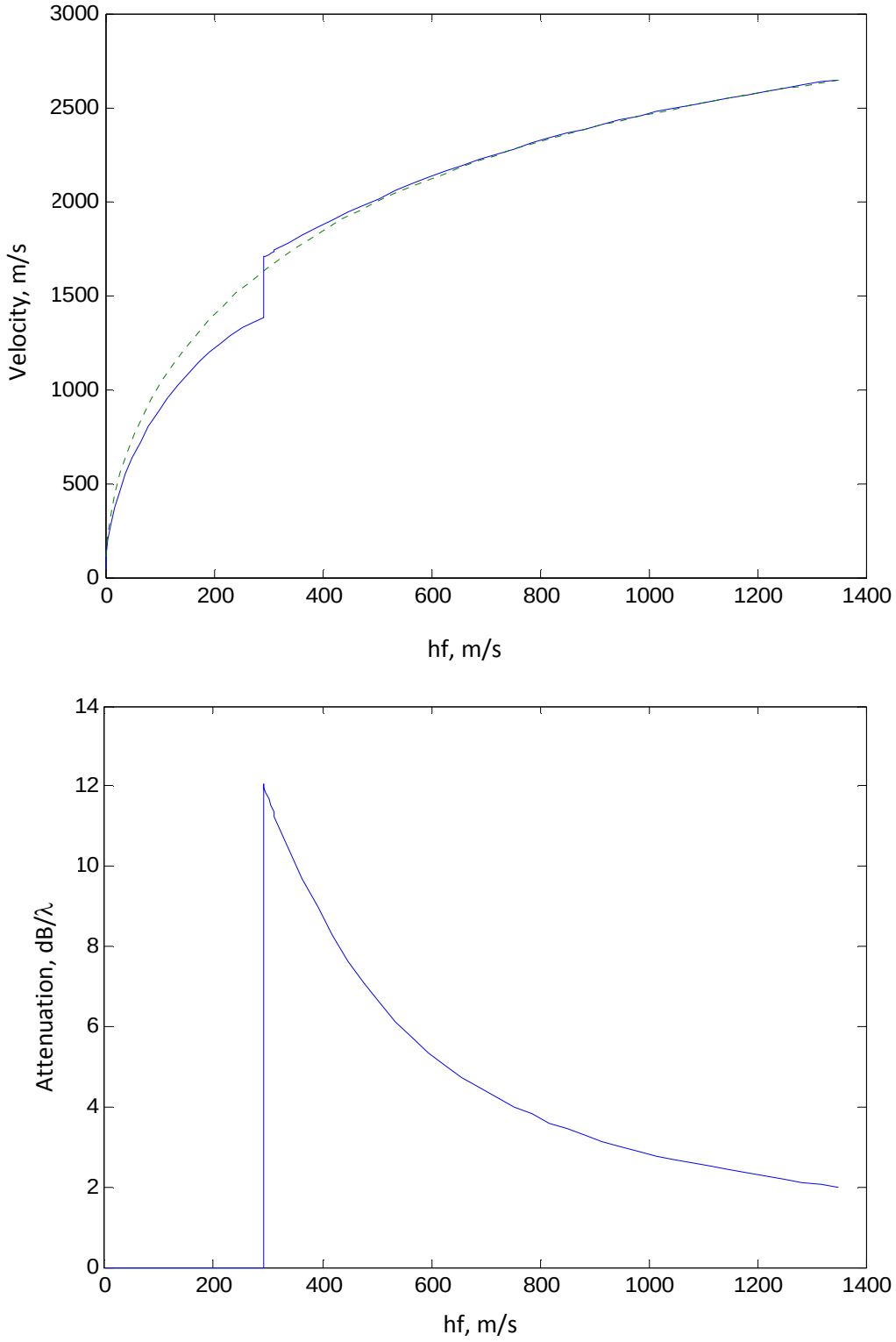

Fig. 15: Velocity (a) and attenuation per wavelength (b) for plate waves propagating in a X-Y+10 quartz plate in the presence of water contacting one of the plate surfaces.

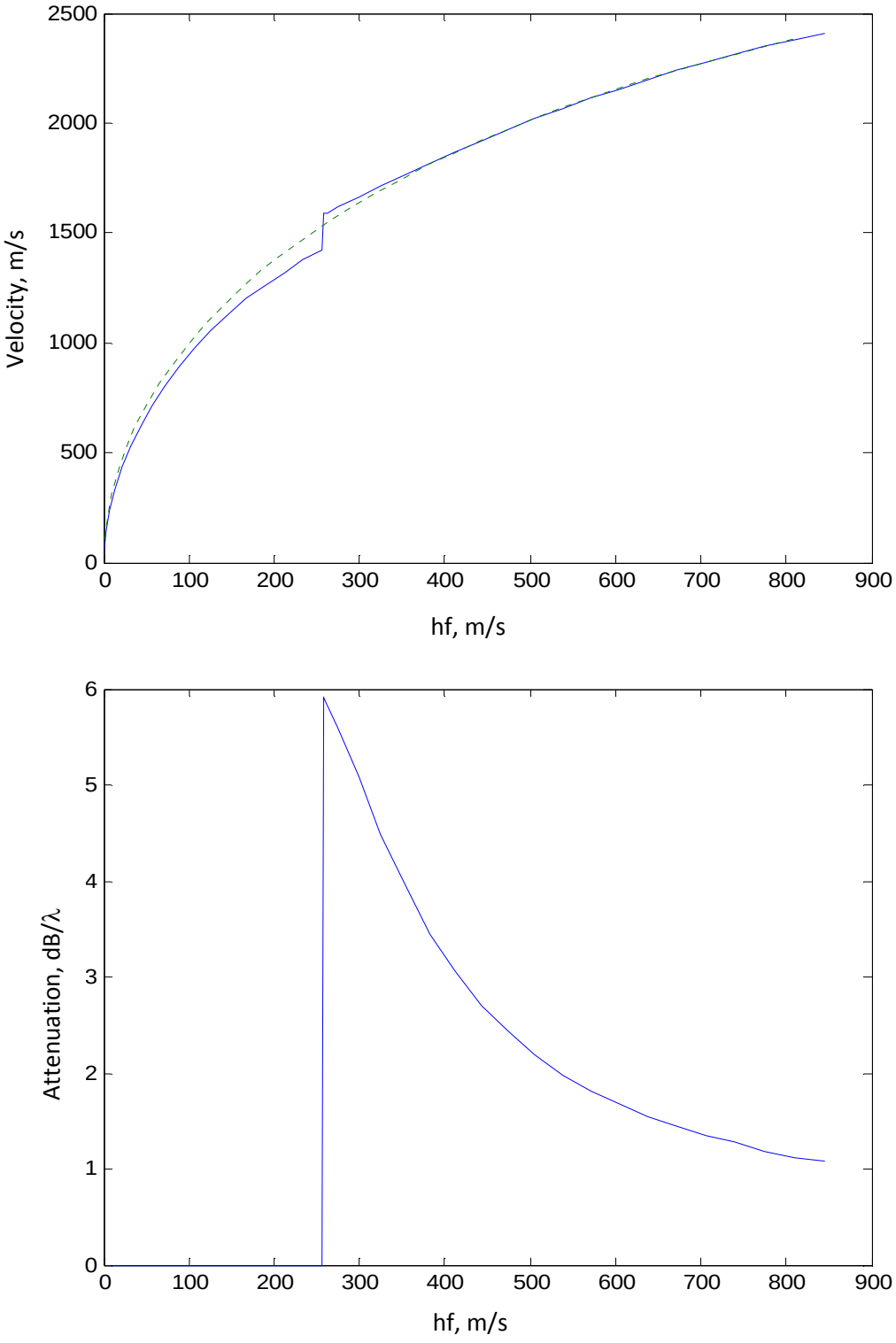

Fig. 16: Velocity (a) and attenuation per wavelength (b) for plate waves propagating in a Y-Z lithium tantalate in the presence of water contacting one of the plate surfaces.

2.4 Fluid on both sides of a piezoelectric plate

In the previous sections we have considered the case where the fluid was in contact with one surface of a piezoelectric plate. In this section we will consider a case where the fluid is present on both sides of the plate. The geometry of the problem under consideration is shown in Fig. 17. The fluid occupies the regions $x_3 < 0$ and $x_3 > h$.

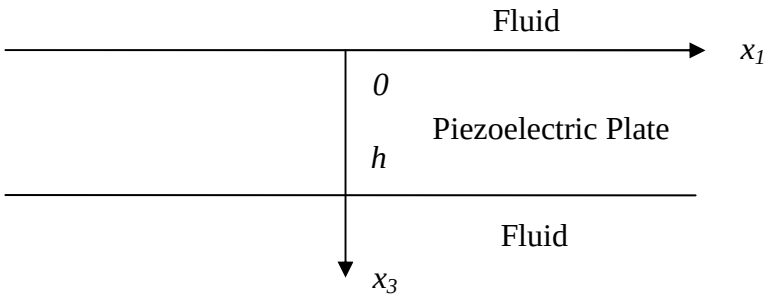

Fig. 17: Geometry of the problem used to analyze propagation of plate acoustic waves in contact with fluid medium on both sides of the plate.

To solve this problem, we use Eqs. (6) through (40) and apply boundary condition equation (42) at the planes $x_3 = 0$ and $x_3 = h$. The method used to solve this problem is as follows. When the plate wave velocity v_p is less than bulk wave in the fluid that is $v_p < v_B$, wave should decay in the fluid, therefore for $x_3 < 0$, b_fs with negative imaginary parts are chosen and for $x_3 > h$, b_fs with positive imaginary parts are chosen. When $v_p > v_B$, wave should grow exponentially and therefore for $x_3 < 0$, b_fs with positive imaginary parts and for $x_3 > h$, b_fs with negative imaginary parts are chosen.

As an example we analyzed the case where there is water on both sides of a 128 Y-X lithium niobate plate. The plots of velocity and attenuation of the plate wave on the parameter *hf* are shown in the Fig. 18. One can see that velocity of the plate wave increases as the *hf* increases, then exhibits a jump at point where sign of b_f changes. The value of *hf* where velocity of the plate wave becomes equal to the bulk wave in water is

200 m/s. The dotted lines in Fig. 18(a and b) are the velocity and attenuation results for the case where the water was in contact with one of the plate surfaces that is water on one side and free space on the other side of a piezoelectric plate. As for the attenuation dependence on *hf*, one can see from the above figures that the attenuation is almost double in this case compared to the case where the water was in contact with only one of the plate surfaces. This is due to the fact that the plate wave is radiating bulk wave from both surfaces, thus resulting in almost double attenuation.

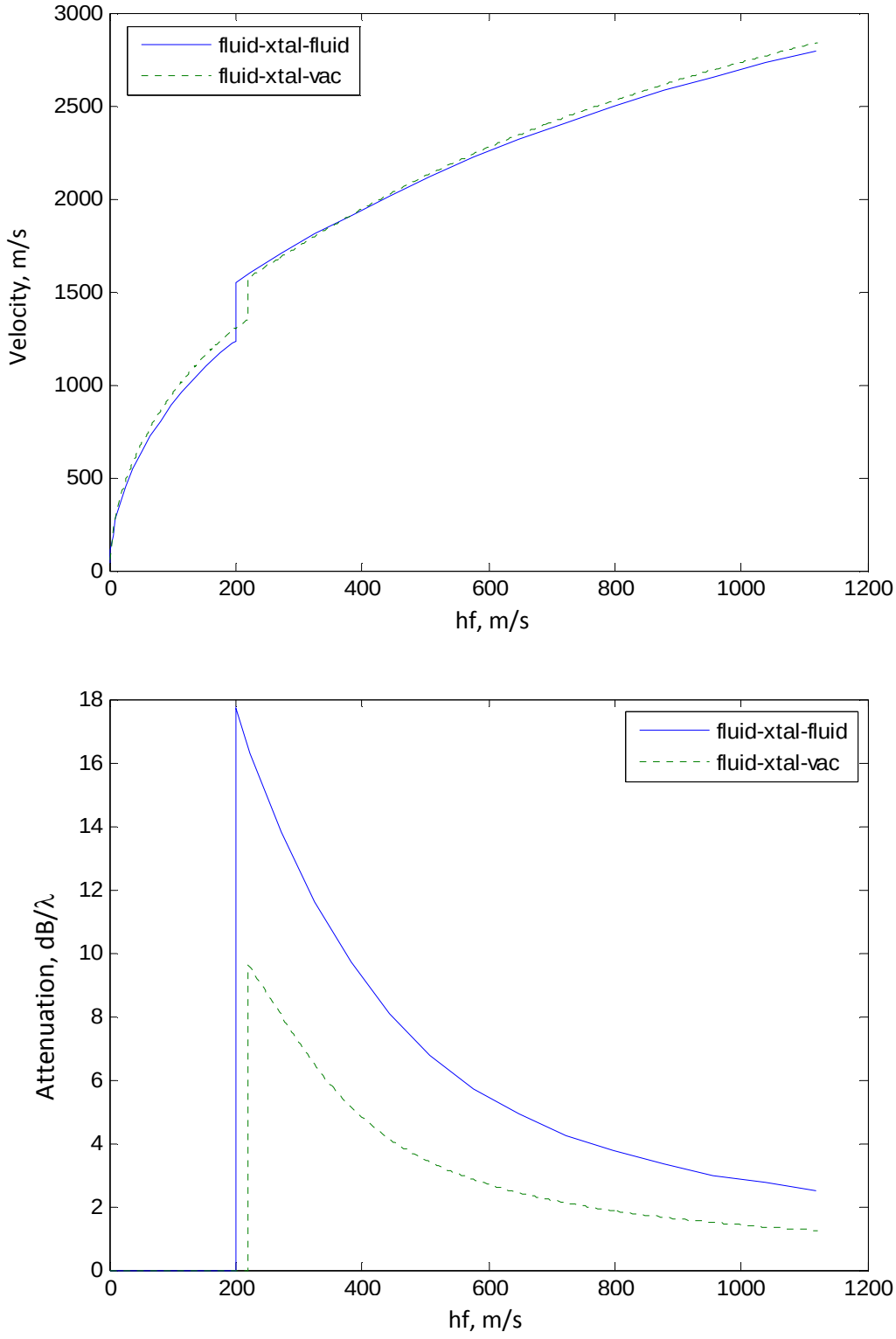

Fig. 18: Velocity (a) and attenuation per wavelength (b) for plate waves propagating in a 128 Y-X lithium niobate plate in the presence of water on both surfaces of the plate.

2.5 Experimental measurements

The theoretical calculations done in this section show that, under suitable conditions, a plate wave propagating in the piezoelectric plate can efficiently generate a bulk acoustic wave in water. This effect can be used to realize efficient transducers for use in ultrasonic flow meters. This fact has been confirmed by preliminary experimental measurements that were performed by Dr. Joshi and some of his other co-workers, namely Drs. Boris Zaitsev and Iren Kuznetsova. Their experimental work is briefly described below.

The use of the mode conversion transducer in a flow meter application is as shown in Fig. 19. The basic operation of this flow meter is as follows. Transducer A converts plate acoustic wave propagating in the plate to bulk acoustic wave in water, while transducer B converts bulk acoustic wave in water into plate acoustic wave. The parameter L represents coupling length which is defined as the length over which plate and bulk waves are coupled to, or interact with, each other.

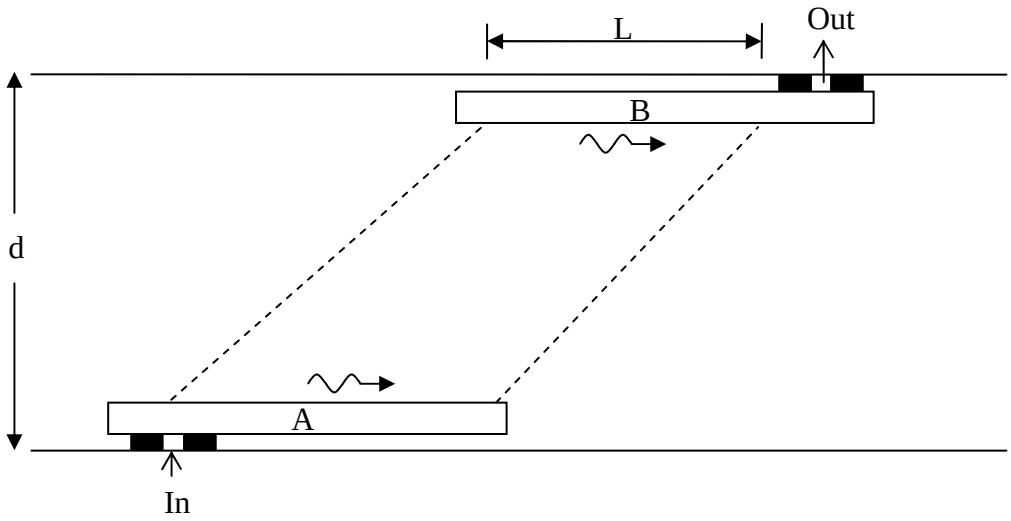

Fig. 19: Block diagram of a flow meter using plate wave to bulk wave mode conversion transducers.

For the experiments performed in our laboratory, devices A and B were identical plate wave delay lines fabricated on a 0.5 mm thick 128 Y- X lithium niobate substrate. The IDTs consisted of 5 finger pairs having period p = 1.82 mm. For h/λ = 0.5/1.82 = 0.275, the velocity of the plate wave is v_p = 2332 m/s giving IDT resonant frequency of f_0 = v_p/p = 1.28 MHz. Thus the device is operating at hf = 640 m/s. The bulk acoustic wave in water is radiated at angle θ given by $\theta = \cos^{-1}(1500/2332) = 50^0$. Preliminary experiments were carried out to measure the overall conversion efficiency of the arrangement shown in Fig. 19 as a function of coupling length L. The results of these measurements are shown in Fig. 20 below. One can see that by proper choice of the coupling length, total insertion loss as low as 12 dB can be obtained. Of this, slightly more than 9 dB loss is due to the inter digital transducers. Thus the total mode conversion loss, PAW to BAW and back from BAW to PAW, is less than 3 dB [29].

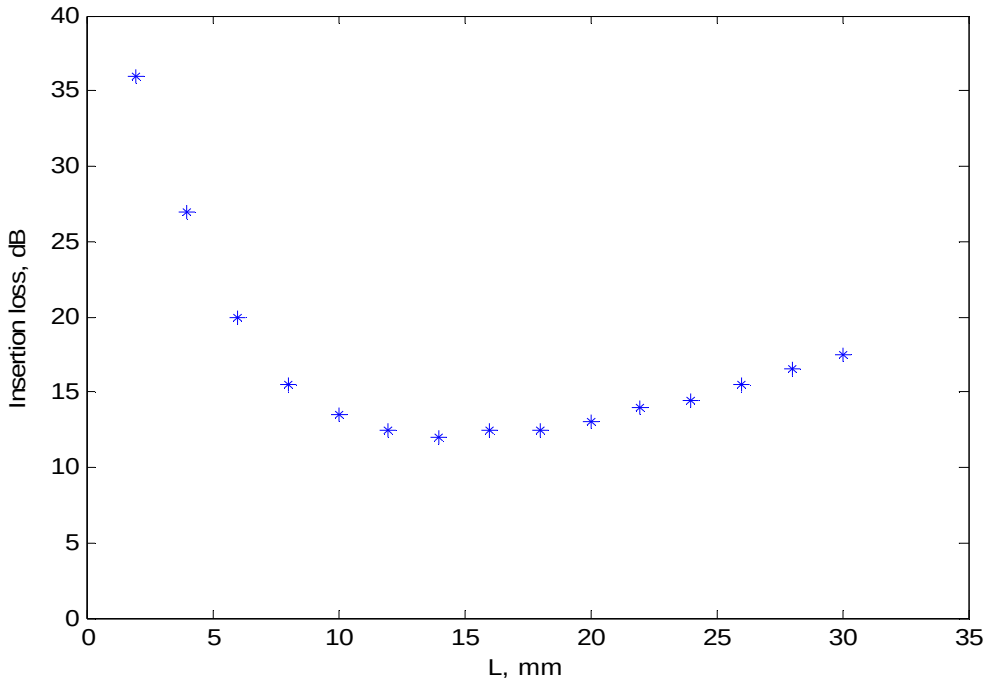

Fig. 20: Overall insertion loss in dB as a function of L, coupling length in mm.

2.6 Radiation of bulk waves in air:

So far we have considered the case where the fluid was a liquid in contact with the piezoelectric plate. In this section we will consider the case where the fluid is a gas such as air, for example. By using the analysis method described previously we carried out theoretical calculations to study the effect of air loading on the plate wave. A particular case of 128 Y-X lithium niobate plate of finite thickness *h* which is in contact with air on the plane $x_3 = 0$ and free space on the plane $x_3 = h$ is considered. The geometry of the problem is as shown in Fig. 21.

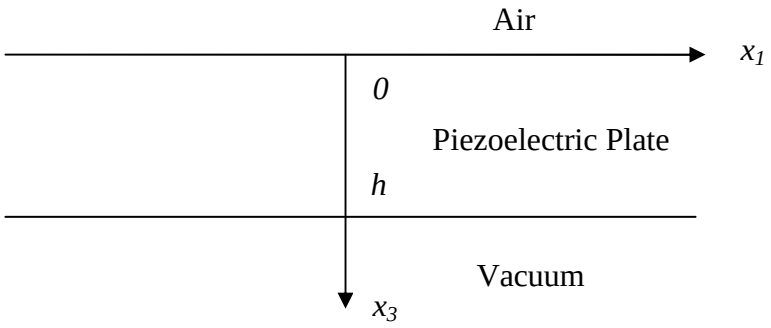

Fig. 21: Geometry of the problem used to analyze propagation of plate acoustic waves in contact with air.

To solve this problem, we use Eqs. (6) through (41) and apply boundary condition equations (42) and (43) in the planes $x_3 = 0$ and $x_3 = h$. The problem was solved by using the method described in section 2.3. The plots of velocity and attenuation of the wave propagating in a 128 Y-X lithium niobate plate in contact with air on one of it surfaces on *hf* are shown in Fig. 22. The velocity of the bulk wave v_B in air is approximately 343 m/s. In this case, the velocity of the wave propagating in a plate v_p should be greater than 343 m/s for the plate wave to radiate energy in the air. Fig 22(a) shows the calculated results

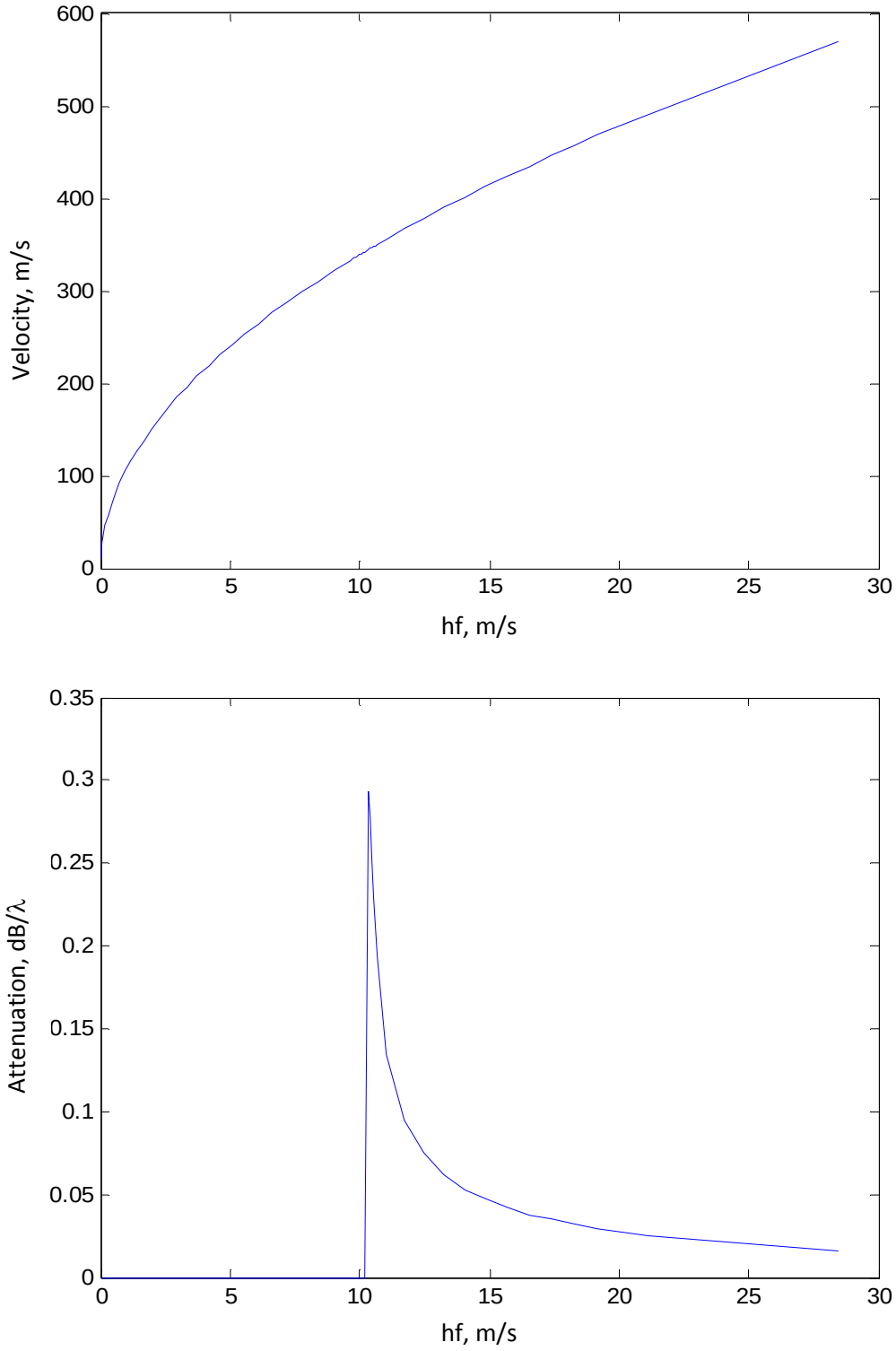

Fig. 22: Velocity (a) and attenuation per wavelength (b) for plate waves propagating in a 128 Y-X lithium niobate plate in the presence of air contacting one of the plate surfaces.

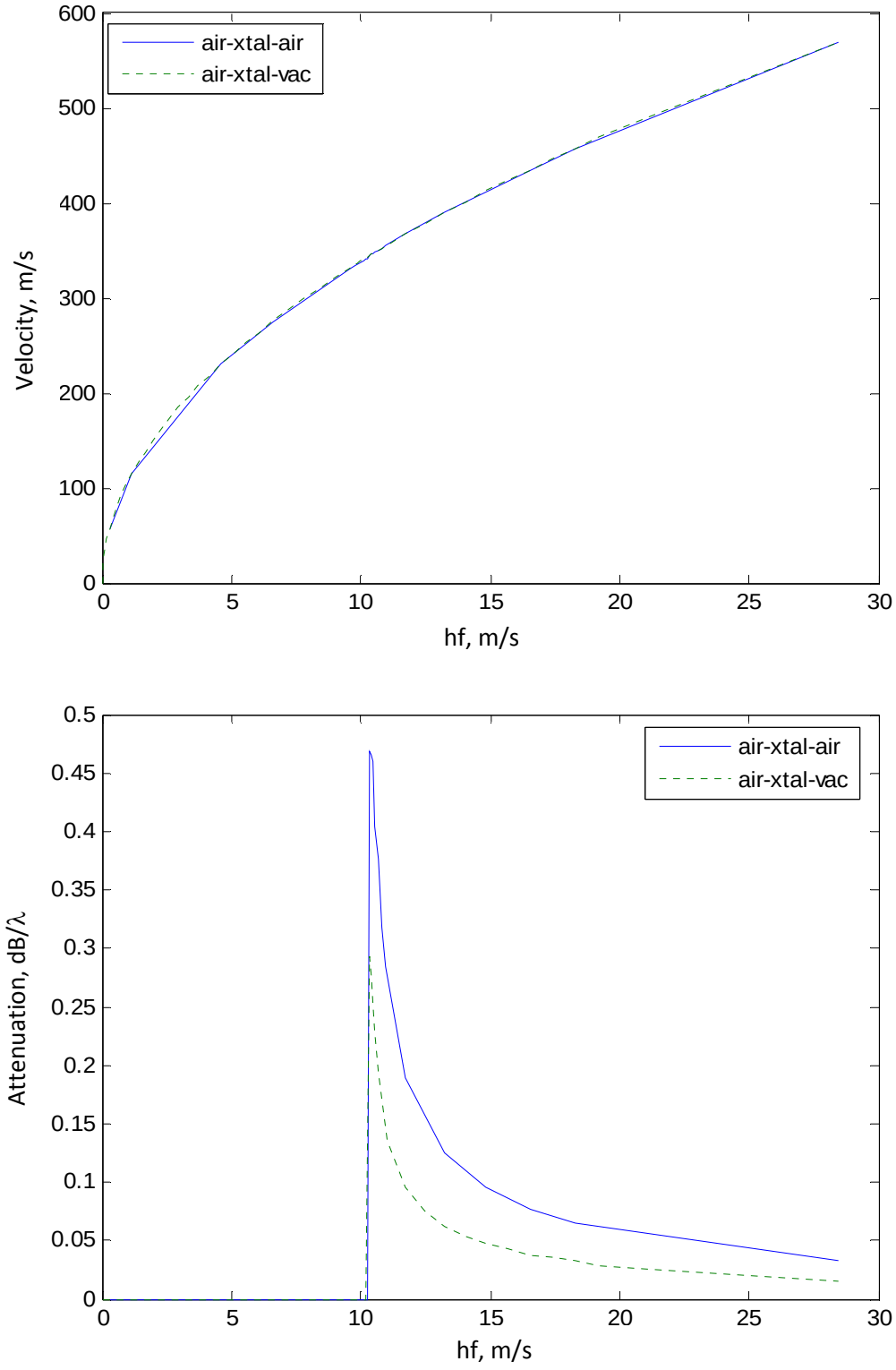

Fig. 23: Velocity (a) and attenuation per wavelength (b) for plate waves propagating in a 128 Y-X lithium niobate plate in the presence of air on both surfaces of the plate.

of the plate wave velocity versus the product *hf*. The velocity plot does not exhibit a noticeable jump in this case due to the relatively weak coupling to bulk waves in air. However, as Fig. 22(b) shows the plate wave will radiate bulk wave in air for values of *hf* greater than 10.3 m/s. The results obtained for the case of air on both sides of the piezoelectric plate are shown in Fig. 23.

The data in Figs. 22 and 23 shows that plate acoustic waves will be able to radiate bulk waves in air. The coupling in the case of air is much weaker than in the case of water. Nevertheless, the fact that mode coupling principle can be used to generate waves in air is encouraging. This can be understood from the discussion below.

It is well known that ultrasonic waves can be generated efficiently in solids and to a certain extent in liquids, but it is very difficult to generate them efficiently in air. Because of this limitation, ultrasonic systems for medical imaging, non destructive evaluation (NDE), material characterization, surface metrology, etc., have to place an ultrasonic transducer in direct contact with the object under test. For many cases of interest, however, the contact method is not acceptable [30].

Development of non-contact ultrasound (NCU) would allow many more useful applications of ultrasonic test methods. The possibility of implementing NCU test systems has therefore attracted the imagination of scientists and engineers for the past many years. One of the essential requirements for successful development of NCU systems is the ability to efficiently generate and detect ultrasonic waves in air. Therefore there is great impetus at present for development of efficient air-coupled transducers. The fundamental problem in air-coupled transducers arises due to the huge acoustic impedance mismatch between solids and gases. For example, the acoustic impedance of a

typical piezoelectric ceramic is 35 MRayl, which is nearly five orders of magnitude greater than that of air which is only 400 Rayl. Air-coupled piezoelectric transducers therefore require the use of impedance matching layers to partially mitigate the enormous impedance mismatch between air and the piezoelectric element. Several matching configurations have been proposed. These include single quarter-wavelength ($\lambda/4$) layers, stacks of $\lambda/4$ layers, half-wavelength ($\lambda/2$) configurations, and a stack of very thin matching layers whose total acoustic thickness is $\lambda/4$. In any of these configurations, a key aspect for successful design of the transducer is the acoustic impedance of the outer layer. This is seriously limited by the availability of consistent materials having the required very low acoustic impedance, very low attenuation, and thickness for the designed configuration and working frequency [31]. The best air-coupled piezoelectric transducers reported to date have insertion losses that range from 24 dB at 0.45 MHz to 50 dB at 2.2 MHz [31, 32]. The fabrication of these transducers is also very complicated. The mode conversion principle discussed here may be able to overcome these problems and allow us to realize efficient air-coupled transducers.

Chapter 3

Development of Application-Specific Integrated Circuit Chip

The aim of this project is to design and fabricate an Application-Specific Integrated Circuit (ASIC) chip containing an amplifier and a frequency counter suitable for use with mode conversion transducers. An integrated circuit chip designed for a specific application is known as an ASIC chip. The advantages of using an ASIC over standard or "off the shelf" ICs can be understood by considering the block diagram of a typical surface acoustic wave (SAW) sensor.

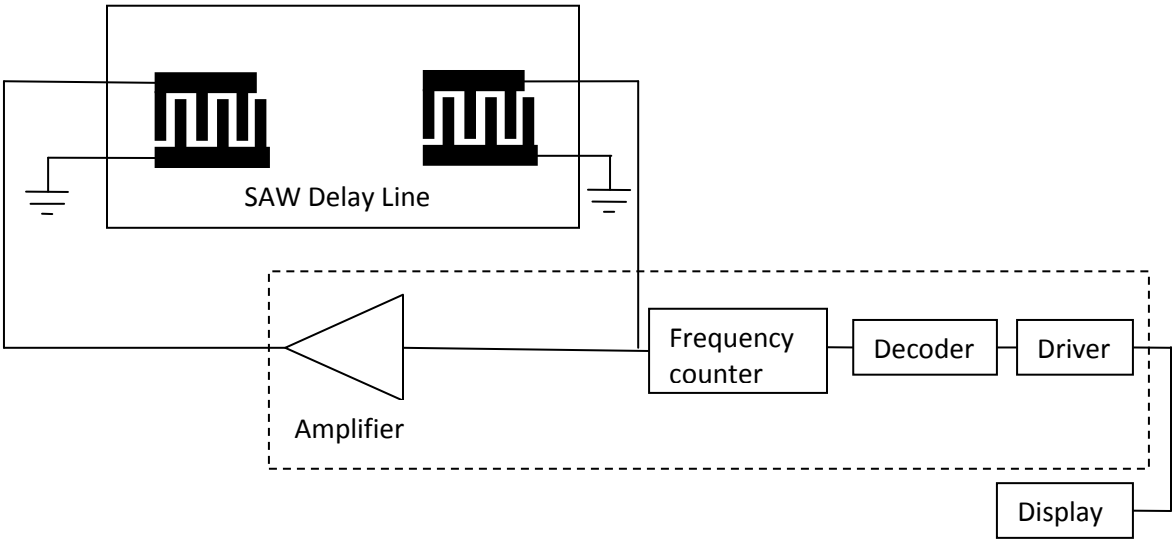

Fig. 24: Block diagram of a typical surface acoustic wave (SAW) sensor.

The block diagram of a SAW sensor is shown in Fig. 24. It consists of a SAW delay line fabricated on a suitable piezoelectric substrate. The output of the delay line is fed back to its input through a suitable amplifier resulting in a delay line stabilized SAW oscillator. The parameter that is to be sensed produces a change in the time delay of the SAW delay line and thereby in the frequency of the oscillator. The change in frequency

can be accurately measured by using a frequency counter. The output of the frequency counter is fed to a decoder which converts the measured frequency to the value of the measured parameter. The value of the sensed parameter is displayed using a suitable driver and display unit. Consider the case of building the circuit shown inside the dotted box using off the shelf ICs. For this case four different chips, namely one for the amplifier, one for the frequency counter, one for the decoder, and one for the driver will be required. By using an ASIC, all the above functions can be implemented in just one chip. This will reduce the number of chips. Also, it will eliminate the problem of interconnections between chips, thus improving system reliability.

The ASIC design in this project is implemented using Metal-Oxide-Semiconductor (MOS) technology. MOSFETs have become the primary switching devices in high-density IC design because they are extremely small, the device structures are very simple, and the drain and source terminals are interchangeable. A layout tool such as Tanner EDA's L-Edit (Layout Editor) is used to design the patterns on each layer and accomplish the physical design of the chip. Each layer in this tool is distinguished by a separate color on the computer monitor and the overall image can be interpreted as the top view of the circuit as shown in Fig. 26. To get a chip fabricated, geometrical design rules setup by different processing lines have to be followed while designing a circuit in L-Edit. These design rules are set of minimum linewidths, spacings, and layout guidelines needed to fabricate a chip. There are two ways to specify these dimensions [33]:

- **Specific Values:** All dimensions are stated in standard unit of length, such as the micron.

- **Scalable:** Distances are specified as a multiple of λ that has dimensions of length. The value of λ is adjusted to correspond to the limitations of the process line.

For this project, we used a 1.50μ Scalable CMOS N-well Analog (SCNA) technology and Scalable Complimentary Metal-Oxide Semiconductor (SCMOS) rules to design the circuits on a 2.2mm×2.2mm pad frame. The value of λ is 0.8 microns. The circuits laid out using L-Edit were fabricated with AMIS-ABN run at University of Southern California (USC). The 40 pin chips designed follow the product definition, protocols and design rules as setup by Tanner EDA Inc. and MOSIS facility in USC.

To design and fabricate an amplifier, we started our work by designing simple n-channel and p-channel MOS transistors. Fig. 25 shows the schematic symbol for an NMOS transistor, where D is the Drain, G is the Gate, S is the Source, and B is the Body or Substrate. The top and cross-sectional view of an NMOS in a layout editor is shown in Fig. 26. The empty grid in L-Edit stands for p-type substrate. The p-type substrate has to be set at the lowest potential used in the circuit so that the source-substrate and drain-substrate junctions always remain reverse biased. Thus the substrate of NMOS transistors in our chips, which is connected to pin numbers 10 and 40, must always be connected to ground.

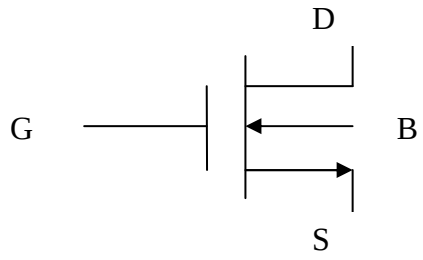

Fig. 25: Schematic symbol for an n-channel MOSFET.

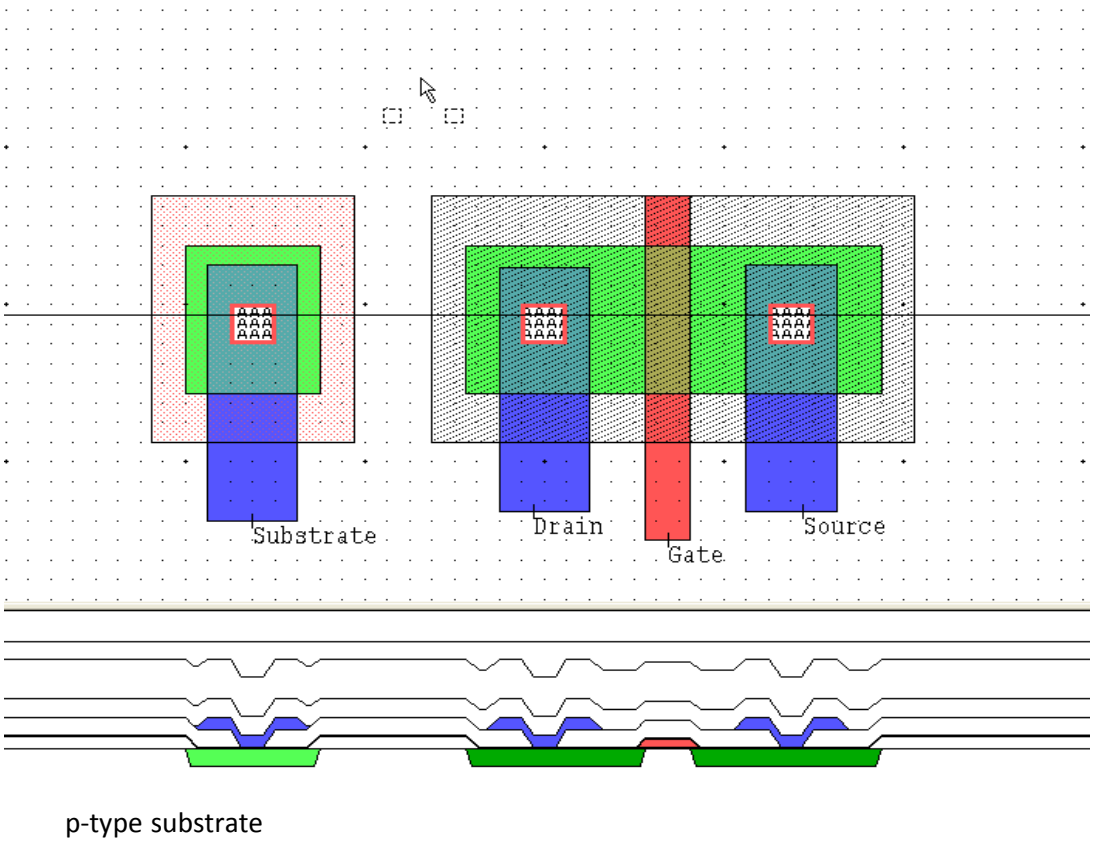

Fig. 26: Top and cross-sectional view of an n-channel MOSFET in a layout editor.

After finishing the design and before exporting the layout for fabrication, any violations in the design rules were checked by running a DRC (Design Rule Check) in L-Edit. After rectifying the design for any possible errors we converted the layout file into GDS II (Graphic Database System) and using SmartFTP-FTP (File Transfer Protocol) Client software we exported the GDS II file to the MOSIS organization for chip fabrication. Fig. 27 is a microphotograph of a NMOS transistor fabricated in one of our chips. One can clearly see that this picture looks same as the top view layout of an NMOS transistor in a layout editor as shown in Fig. 26.

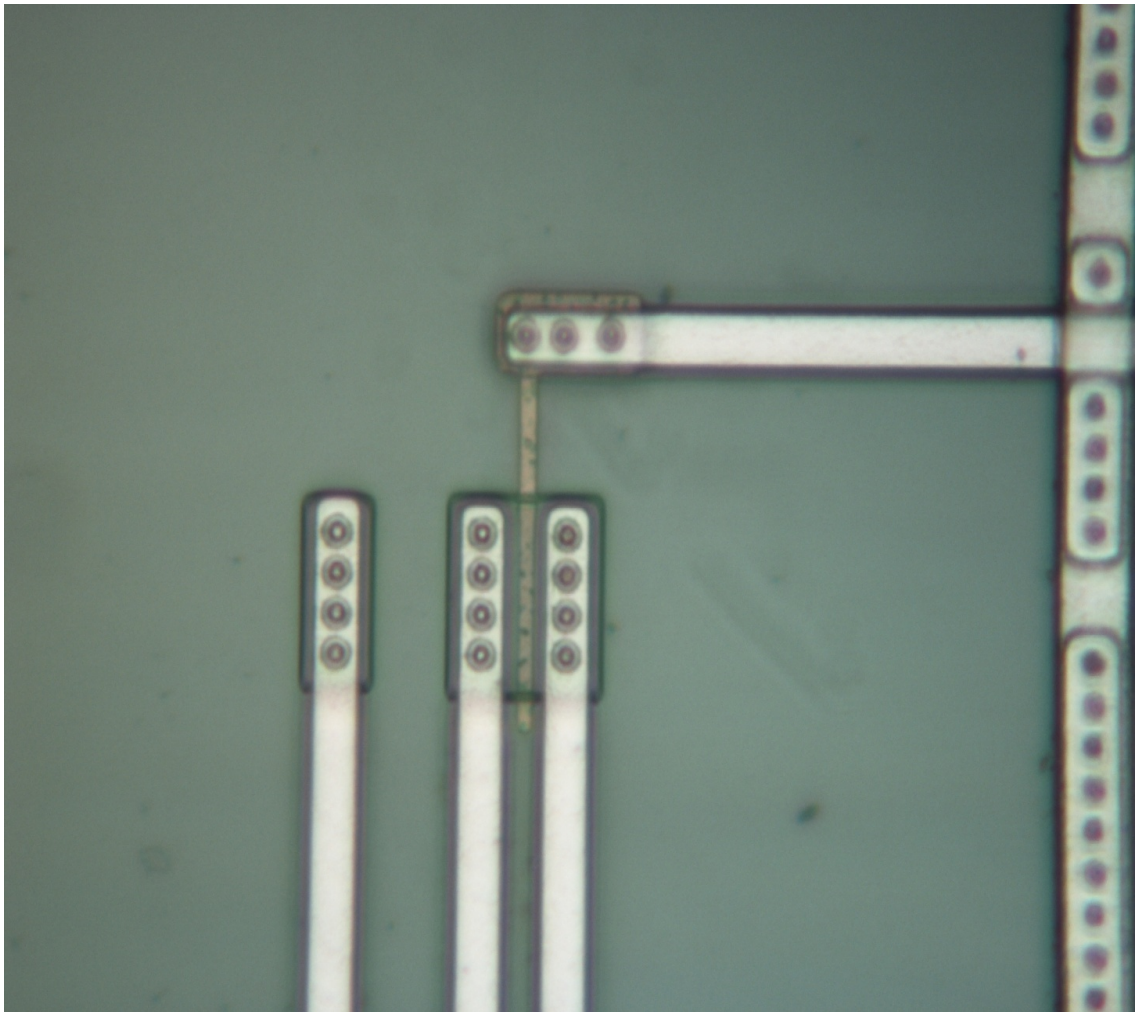

Fig. 27: Microphotograph of an NMOS transistor inside a chip. The magnification factor is 100.

3.1 Output characteristics of an NMOS transistor

The output characteristics of the MOSFET are a family of curves that show the drain current I_D versus drain-to-source voltage V_{DS} with the gate-to-source voltage V_{GS} as a parameter. To study the output characteristics of an NMOS transistor the circuit was connected as shown in Fig. 28. For theoretical analysis OrCAD capture PSpice was used. The spice parameters used in PSpice are given in Appendix C. The drain current I_D was measured by sweeping the drain-to-source voltage V_{DS} from 0 to 5 volts in steps of 0.1

volts, for V_{GS} = 0, 1, 2, 3, 4 and 5 volts respectively. By using LABVIEW setup in the Nanotechnology laboratory at Marquette University, the output characteristics plot was obtained on HP 4145A Semiconductor Parameter Analyzer. Fig. 29 shows the theoretical and experimental results for an NMOS transistor having width-to-length ratio (W/L ratio) of 30.

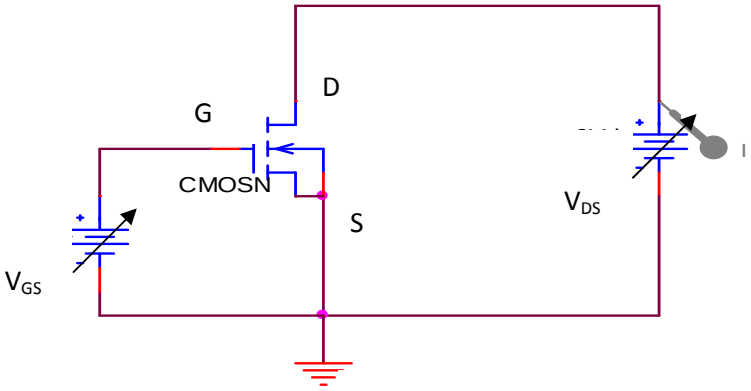

Fig. 28: Output characteristics measurement for an NMOS transistor.

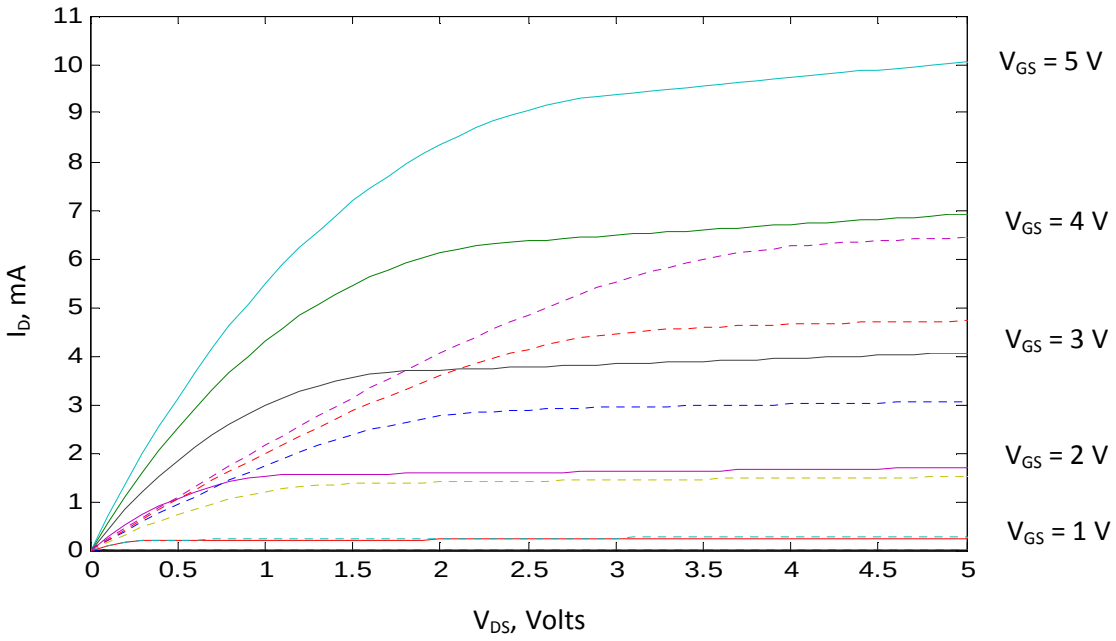

Fig. 29: Output characteristics of an NMOS transistor having W/L = 30. Solid lines: theory; dotted lines: experiment.

3.2 Transfer characteristics of an NMOS transistor

The transfer characteristics of the MOSFET refer to a graph of I_D versus V_{GS} when the device is in saturation. To study the transfer characteristics of an NMOS the circuit is connected as shown in Fig. 30. The gate and drain were tied together for the circuit to operate in the saturation region. From Pspice, by sweeping the gate-to-source voltage V_{GS} from 0 to 5 volts in steps of 0.1 volts, a plot of I_D versus V_{GS} was obtained as shown in Fig. 31. For experimental analysis, the circuit was built on the breadboard. By using a HP E3631A Triple Output DC power supply as a voltage source, V_{GS} was applied to the appropriate pins on the chip. The drain current I_D for V_{GS} = 0 to 5 volts was measured using an Agilent 34401A Digital Multimeter. The dotted line in Fig. 31 indicates the experimental data obtained.

By following the design rules described above, NMOS transistors having W/L values of 10 and 1 were also designed and fabricated. Fig. 32 and 33 are the plots of transfer characteristics of these devices. We see that experimental results are in fair agreement with theory for W/L values of 30 and 10. However, for reasons that are not clear to us, we see large deviation between theory and experiment for device having W/L = 1.

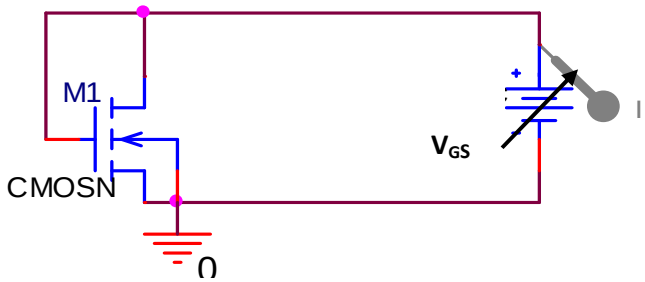

Fig. 30: Transfer characteristic measurement for an NMOS transistor.

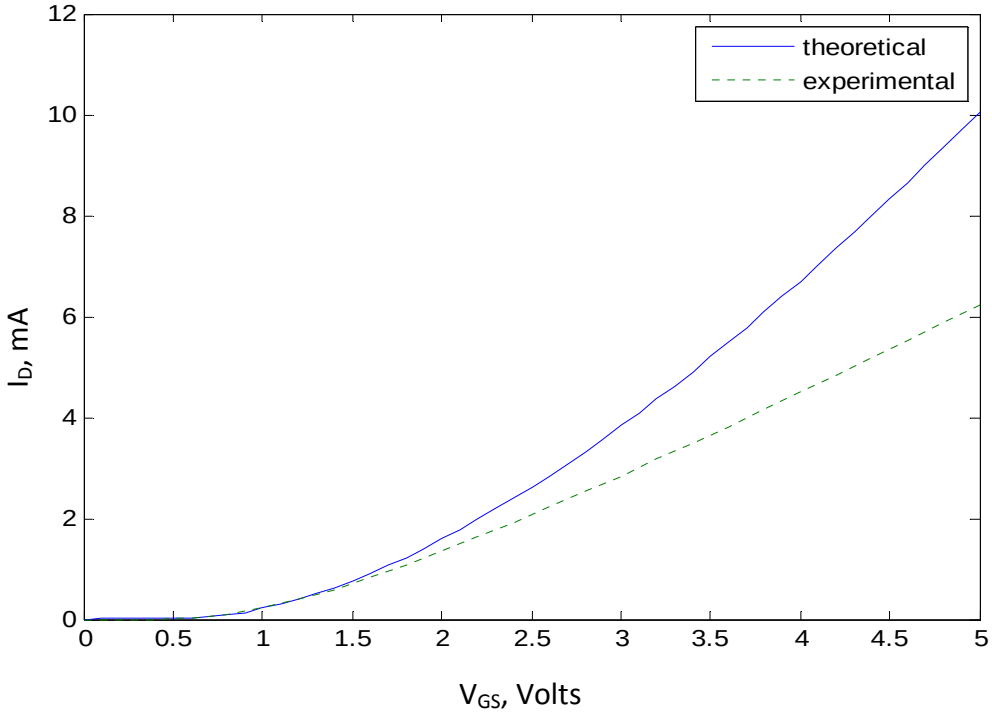

Fig. 31: Transfer characteristics of an NMOS transistor having W/L = 30.

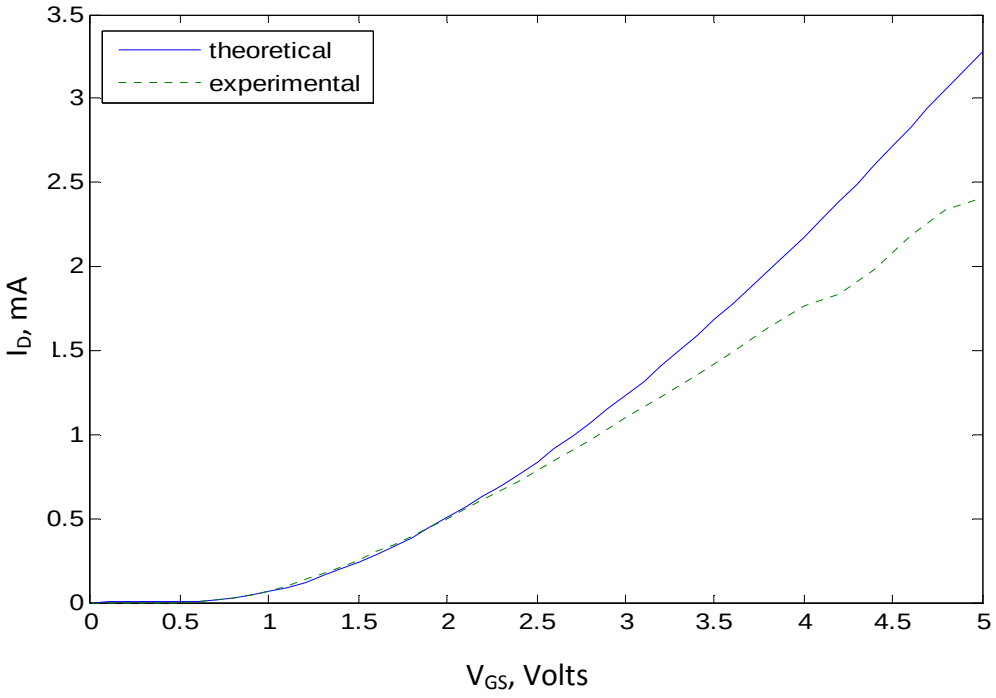

Fig. 32: Transfer characteristics of an NMOS transistor having W/L = 10.

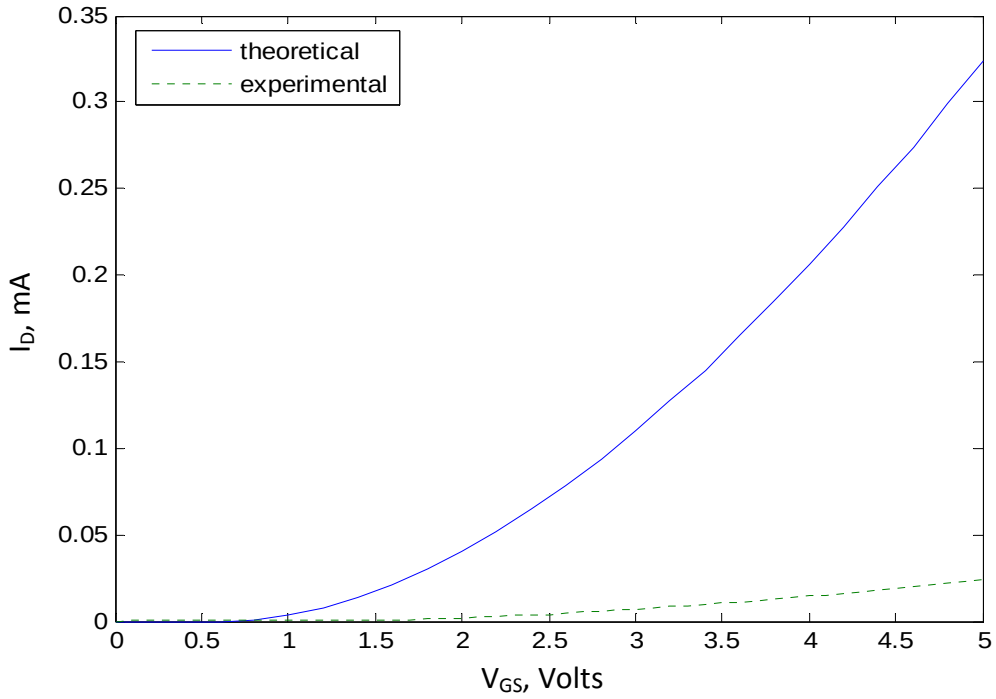

Fig. 33: Transfer characteristics of an NMOS transistor having W/L = 1.

3.3 Comparison between theory and experiment

It is useful at this point to compare the theoretical and experimental results for the output and transfer characteristics shown in Figs. 29, 31, 32, and 33. First let us look at the transfer characteristics shown in Figs. 31 through 33. According to the simple MOS model, the drain current I_D varies as square of V_{GS}. However, this ignores the velocity saturation effect that occurs in short channel devices [34]. Velocity saturation effects set in for values of V_{DS} greater than V_{DSsat} where V_{DSsat} is given by

$$V_{DS_{sat}} = \left(\frac{L}{\mu_n}\right) v_{sat}$$

Here L = length of the channel, μ_n = mobility of electrons, and v_{sat} = saturation velocity of electrons, which is approximately 10^7 cm/s. Now, for our devices, L = 1.6 µm and μ_n = 550 cm^2/Vs. So from the above equation, we get V_{DSsat} = 2.9 V. Due to velocity

saturation, the plot of I_D versus V_{GS} becomes linear. Now, for the plots in Figs. 31 – 33, the gate and drain are tied together (Fig. 30). So here $V_{DS} = V_{GS}$. We see that indeed the experimental plots begin to deviate from theory for values of V_{GS} greater than about 2.5 V, and that the variation of I_D versus V_{GS} becomes nearly linear. As regards the output characteristics shown in Fig. 29, here also we note that experimental values start to deviate appreciably from theory for values of V_{DS} greater than about 2.5 V. Further, due to velocity saturation, values of I_D are lower than those calculated from the simple model. This is also observed in our experimental data. Fig. 33 shows that for the very narrow device having W/L = 1, the experimental values of current are much lower than theoretically calculated values. This is probably due to the high contact resistance in this device. When the device width W is large, one can open multiple contact windows in the active layer (as shown in Fig. 27) so as to reduce the effective contact resistance. But this is not possible when channel width W is small.

3.4 Transfer characteristics of a PMOS transistor

The schematic symbol for a PMOS transistor is shown in Fig. 34. By following the design rules explained above we designed a p-channel MOSFET in the layout editor. Fig. 35 shows the top and cross-sectional view layout of a PMOS transistor in an L-Edit. One can see the n-well formed in a p-type silicon substrate and the source, gate, drain and body incorporated in that n-well. The microphotograph of a p-channel MOSFET in a 40 pin chip is shown in Fig. 36. The reason for many active contacts that one can notice in our NMOS and PMOS transistors (Fig. 36) is as follows. Let us say for example that each contact between active layer and metal has a resistance of 60 Ohms. One cannot neglect such resistance, so to lower the resistance many active contacts are made in parallel, to

get a lower total resistance. Multiple contacts were also made for other layers in a layout editor which are in contact with each other. For simplicity, these contacts are not shown in any of the figures listed in this chapter.

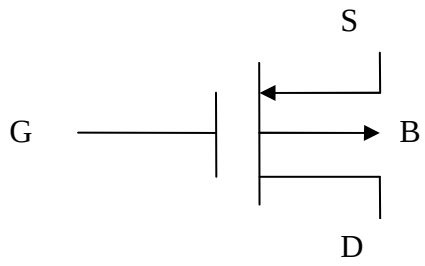

Fig. 34: Schematic symbol for a p-channel MOSFET.

Also, for the source-substrate and drain-substrate junctions of this transistor to stay reverse biased, the n-well of the p-channel transistor should be connected to the highest potential used in the circuit. Thus pin number 30 in our chip which is connected to the n-well must always be connected to highest potential in the circuit. Theoretical and experimental plots of output characteristics and transfer characteristics for a PMOS transistor having W/L = 30 are shown in Figs. 37 and 38.

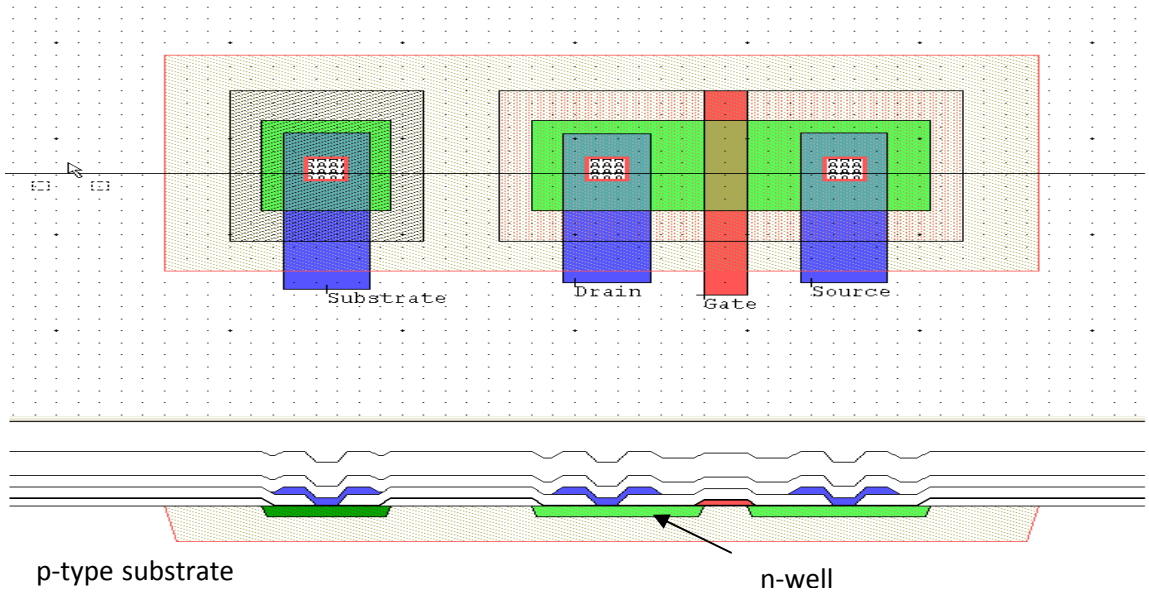

Fig. 35: Top and cross-sectional view of a p-channel MOSFET in a layout editor.

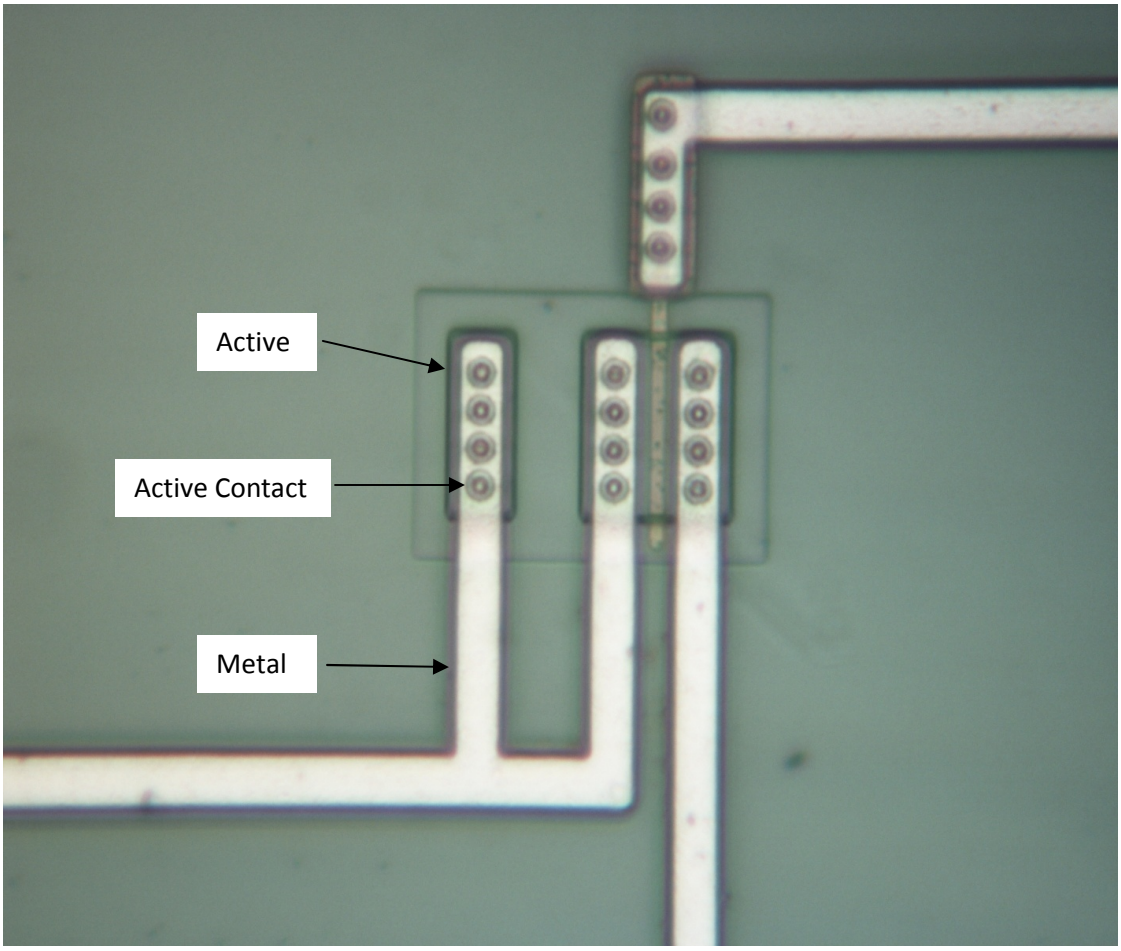

Fig. 36: Microphotograph of a PMOS transistor inside a chip. The magnification factor is 100.

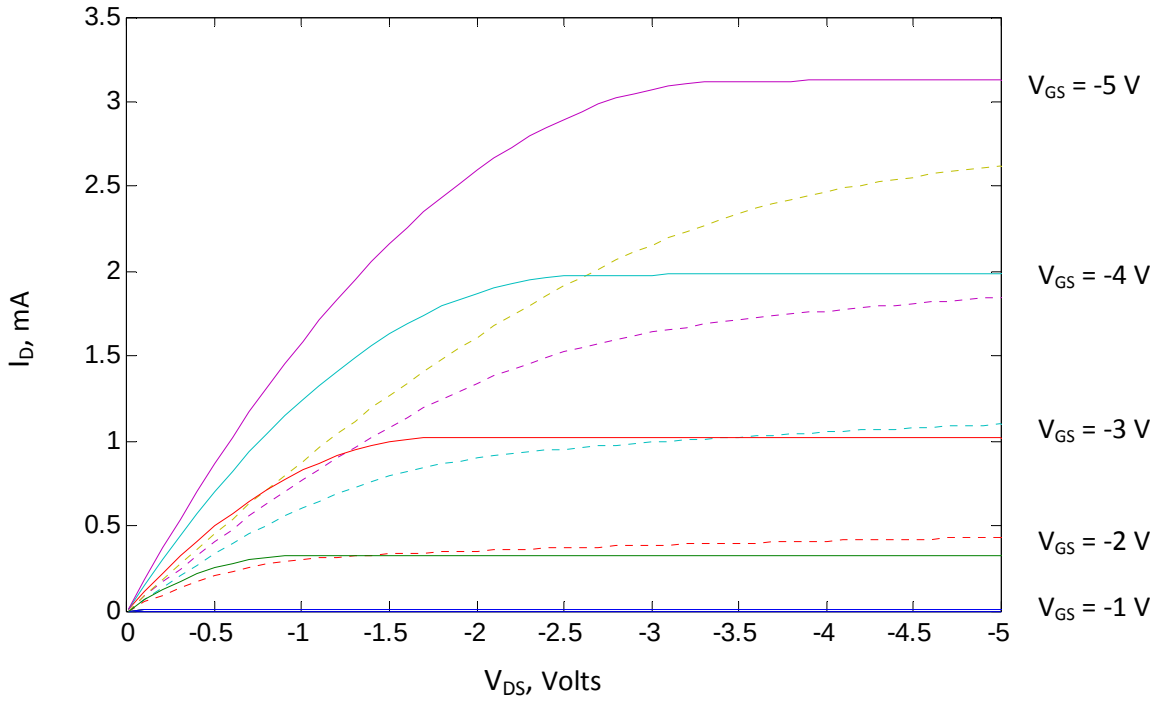

Fig. 37: Output characteristics of a PMOS transistor having W/L = 30.

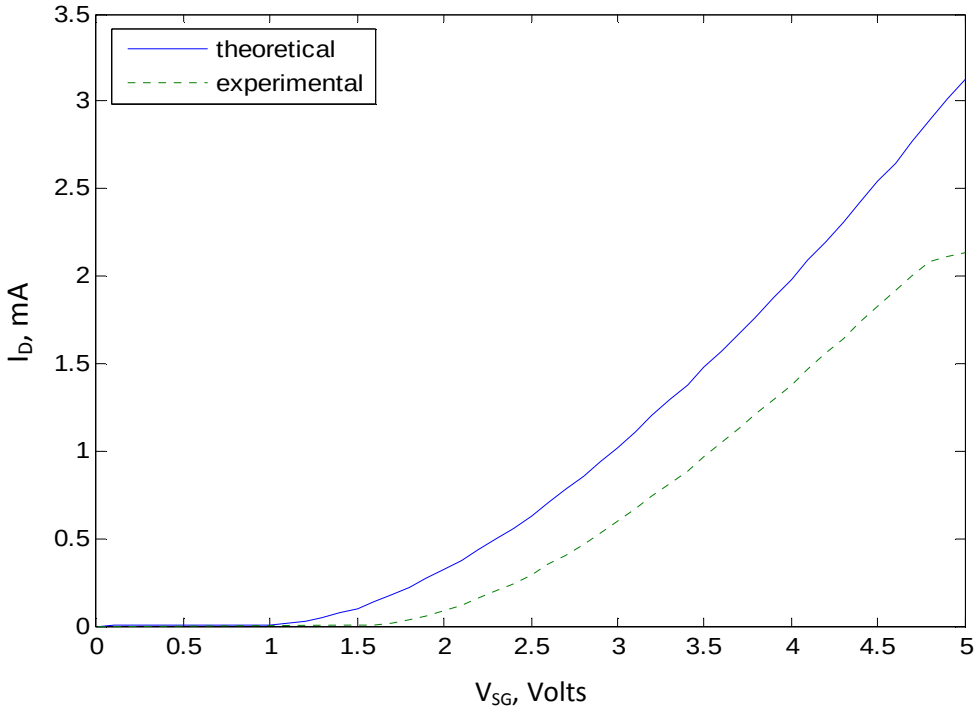

Fig. 38: Transfer characteristics of a PMOS transistor having W/L = 30.

The discussion in section 3.3 also applies to Figs. 37 and 38 to explain the deviation of experimental plots compared to theory.

3.5 CMOS circuit design

Complementary Metal-Oxide Semiconductor (CMOS) circuits are used in many applications from gate arrays to control logic. There are three main types of CMOS processes, they are

- **n-well CMOS:** In this process a p-type substrate is used. NMOS transistors are formed by diffusing n-type material into the substrate. For the PMOS transistors, a well of n-type is diffused in the substrate and the p-type diffusion then defines the drain and source of the PMOS transistors.
- **p-well CMOS:** In this process an n-type substrate is used. PMOS transistors are formed by diffusing p-type material into the substrate. For the NMOS transistors, a well of p-type is diffused followed by n-type diffusion within the well.
- **Twin tub CMOS:** This process uses both n-type and p-type wells in a lightly doped substrate.

The 1.50µ SCNA technology we used for designing our chips uses an n-well CMOS process. By using the NMOS and PMOS transistor layouts described in previous sections, a CMOS inverter was designed and fabricated. The schematic symbol of an inverter is shown in Fig. 39.

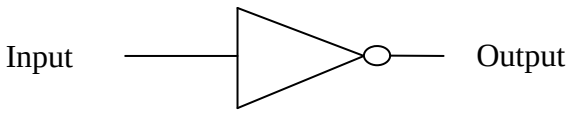

Fig. 39: Schematic symbol of an Inverter.

3.5.1 Voltage transfer characteristics (VTC) of CMOS inverter

The voltage transfer characteristics of a circuit refers to a plot of the output voltage V_{OUT} versus the input voltage V_{IN}. For the CMOS inverter circuit shown in Fig. 40 below, one can see that the gate of the PMOS device (upper device) is connected to the gate of the NMOS device (lower device). When the input is at V_{DD}, the NMOS device is conducting while the PMOS device is cut off. Hence the drain current of the NMOS is limited to the very small leakage current of the PMOS, even though a highly conductive channel is present in the NMOS device. The result of the very small leakage current flowing through the highly conductive channel is that V_{OUT} is approximately 0 V. When the input is at ground, the NMOS device is cut off while the PMOS device is conducting. Only the small leakage current of the NMOS can flow, so V_{OUT} is very close to V_{DD}.

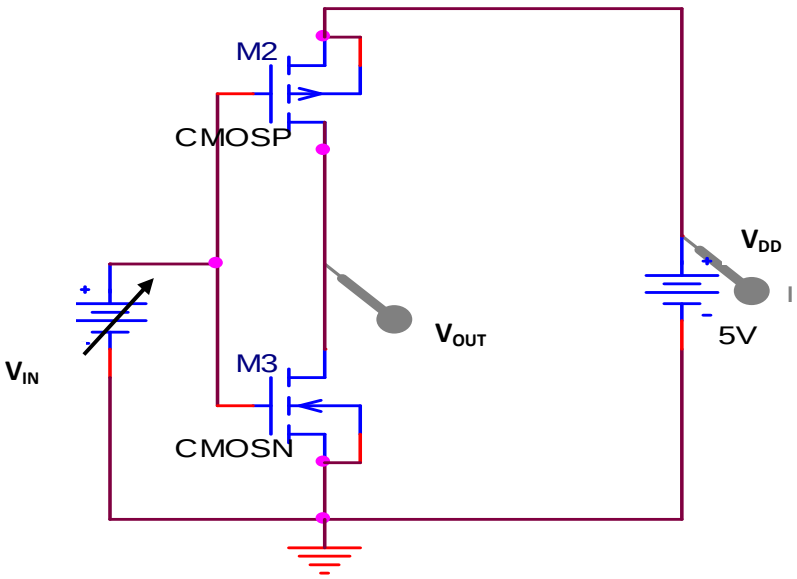

Fig. 40: Voltage transfer characteristics measurement for a CMOS inverter.

For a CMOS inverter circuit with width-to-length ratios of PMOS and NMOS devices of 30:1 and 10:1 respectively, SPICE analysis of voltage transfer characteristics was carried out by sweeping the input voltage from 0 to 5 volts in steps of 0.1 volts. The resulting plot of V_{OUT} versus V_{IN} was obtained as shown in Fig. 41. For experimental analysis, the input was connected to a triple output DC power supply, and by sweeping the input voltage from 0 to 5 volts in steps of 0.1 volts, the voltage across output was measured using a Digital Multimeter. Similar measurements were carried out for CMOS inverters with width-to-length ratios of PMOS and NMOS devices of 10:1 and 10:1, and 10:1 and 30:1 respectively. The theoretical analysis of voltage transfer characteristics of these inverters has been compared with experimental values obtained as shown in Fig. 42.

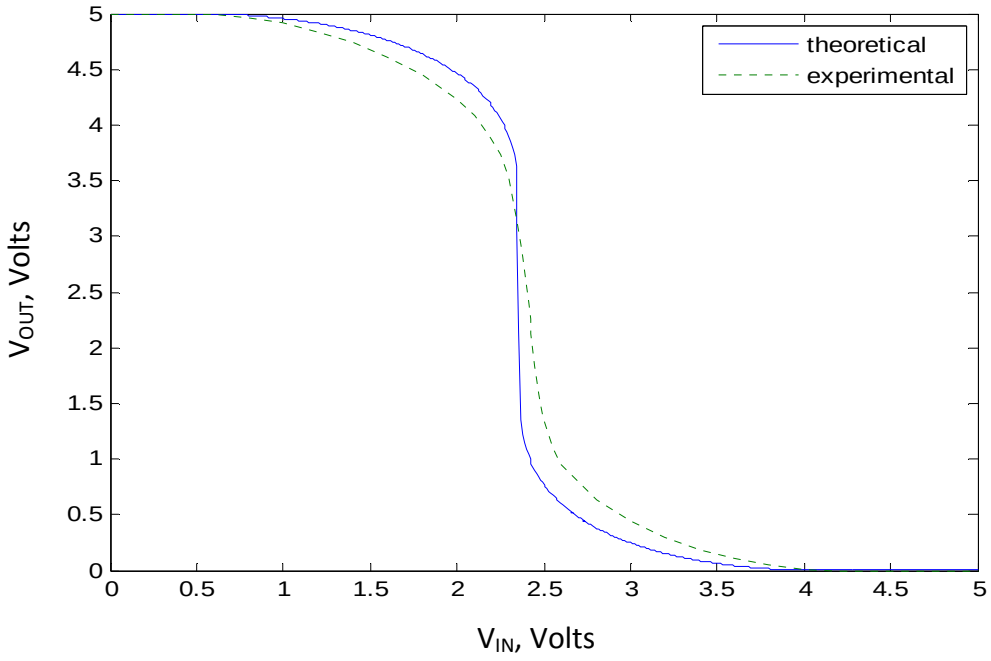

Fig. 41: Voltage transfer characteristics of a CMOS inverter. W/L values of PMOS and NMOS devices are 30:1 and 10:1 respectively.

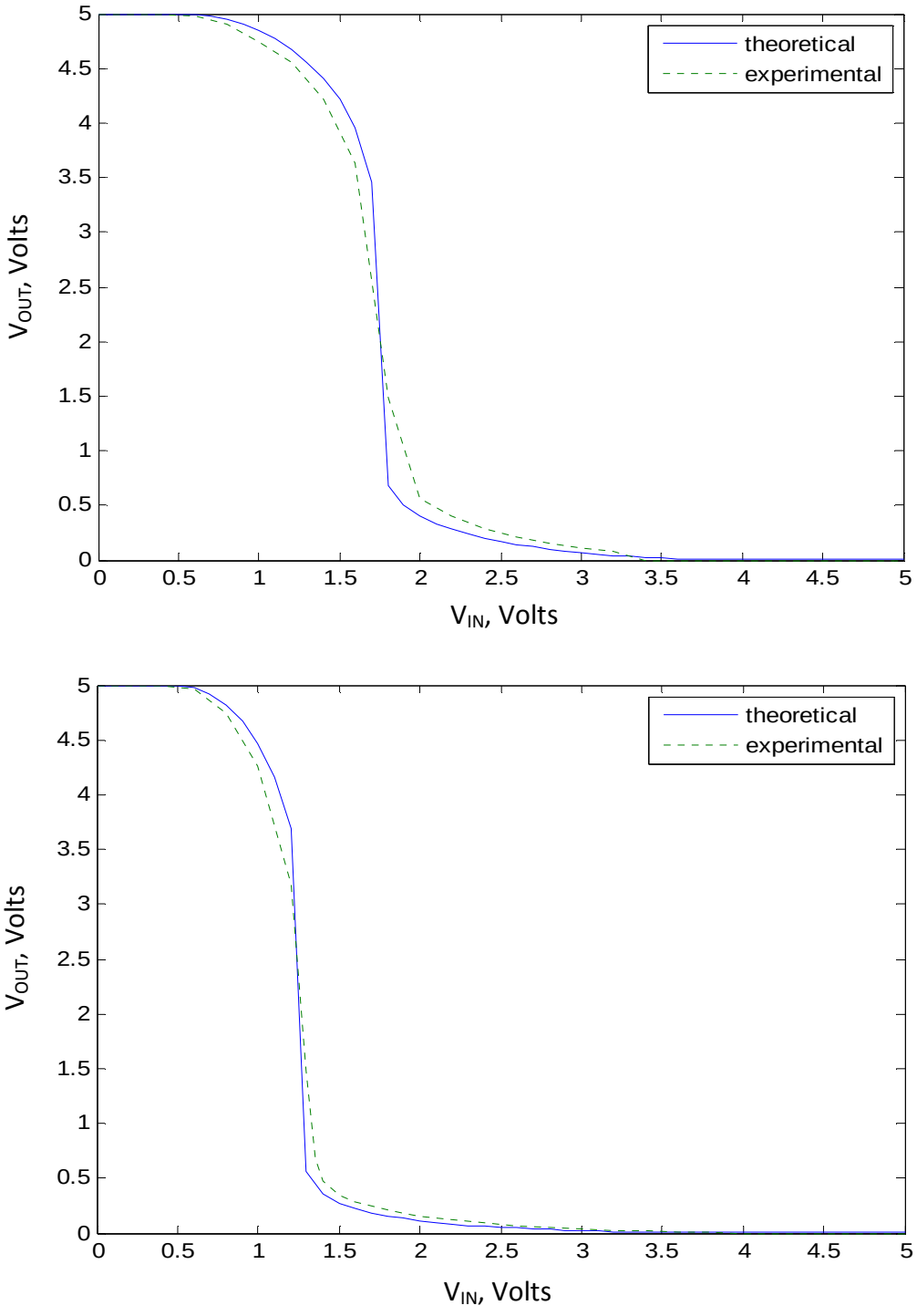

Fig. 42: Voltage transfer characteristics of a CMOS inverter. W/L values of PMOS and NMOS devices are (a) 10:1 and 10:1, and (b) 10:1 and 30:1.

3.5.2 CMOS inverter as a small signal amplifier

In this section we will discuss the use of a CMOS inverter as a small signal or ac amplifier. Fig. 41 is also the transfer function of a CMOS inverter which is due to the rapid voltage change about the switching thresholds. For a perfectly symmetric inverter, the steep transition region is halfway between the power supply V_{DD} and ground. This region can be used to design an amplifier with a linear inverting transfer function. Maximum gain can be obtained by operating the inverter amplifier in this region.

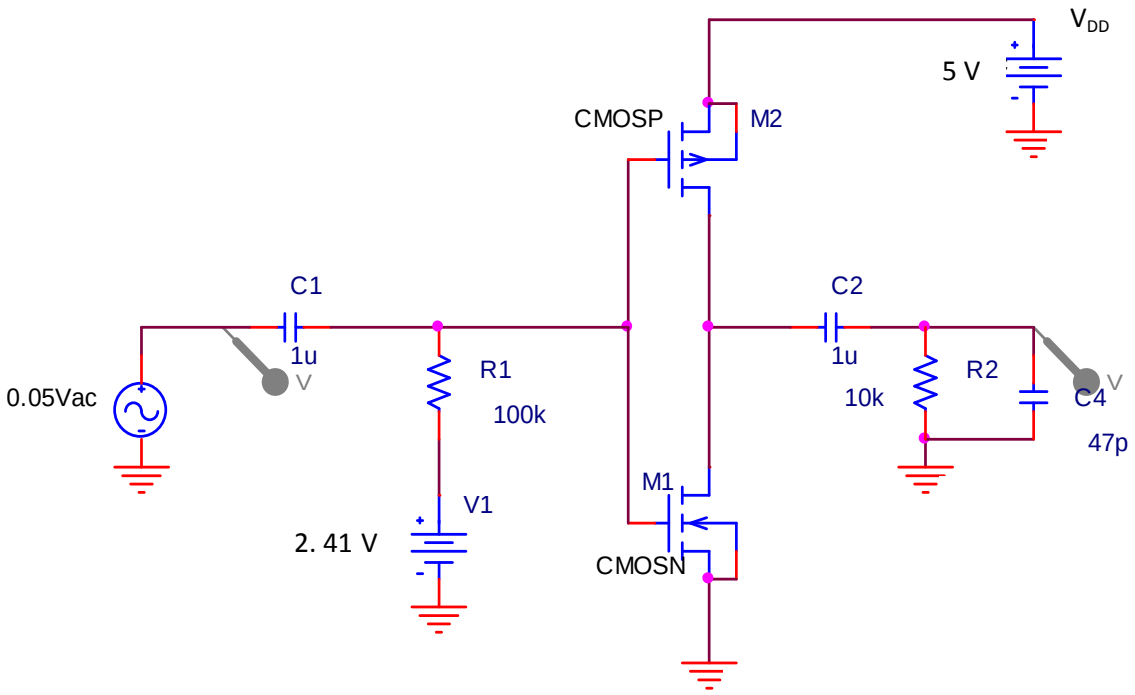

Fig. 43: Setup for CMOS inverter as a small signal amplifier. The output is taken across a parallel RC load.

To design a small signal linear amplifier the circuit was connected as shown in Fig. 43. For operation as a linear amplifier, the input was biased at 2.41 volts DC through resistor R1. A sinusoidal signal of 50 mV amplitude was applied as input as shown in

Fig. 43. The voltage gain of the amplifier is V_{OUT}/V_{IN} and here V_{IN} is 50 mV. The output was measured across a parallel RC load. For experimental analysis, a HP E3631A Triple Output DC Power supply, a HP 33120A Function generator, an Agilent 54641A Oscilloscope and, HP 10071A 10:1 Oscilloscope probes were used. The oscilloscope input and output waveforms at 100 kHz frequency are shown in Fig. 44. In Fig. 44, RMS (1) represents the RMS voltage applied at the input, which was connected to channel 1 of the oscilloscope, where as RMS (2) represents the RMS voltage across output (i.e across the load of 10 KΩ resistor in parallel with a 47 pF capacitor), which was connected to channel 2 of the oscilloscope.

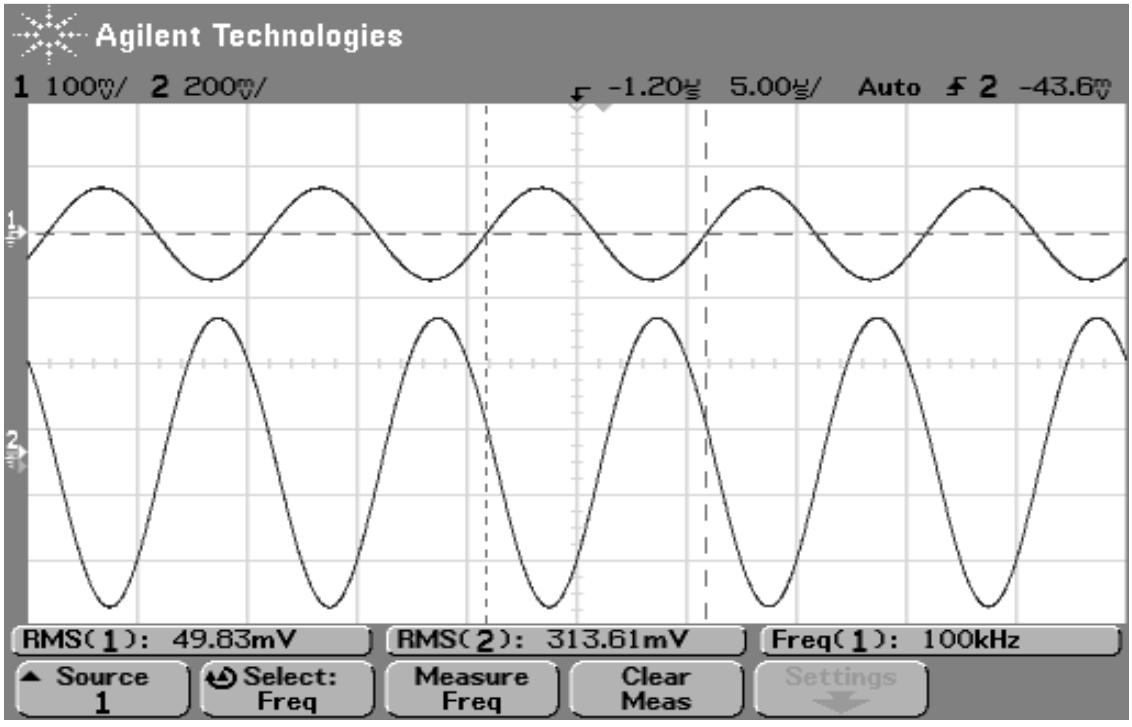

Fig. 44: Input and output voltage waveforms of a CMOS inverter as an amplifier at 100 kHz frequency.

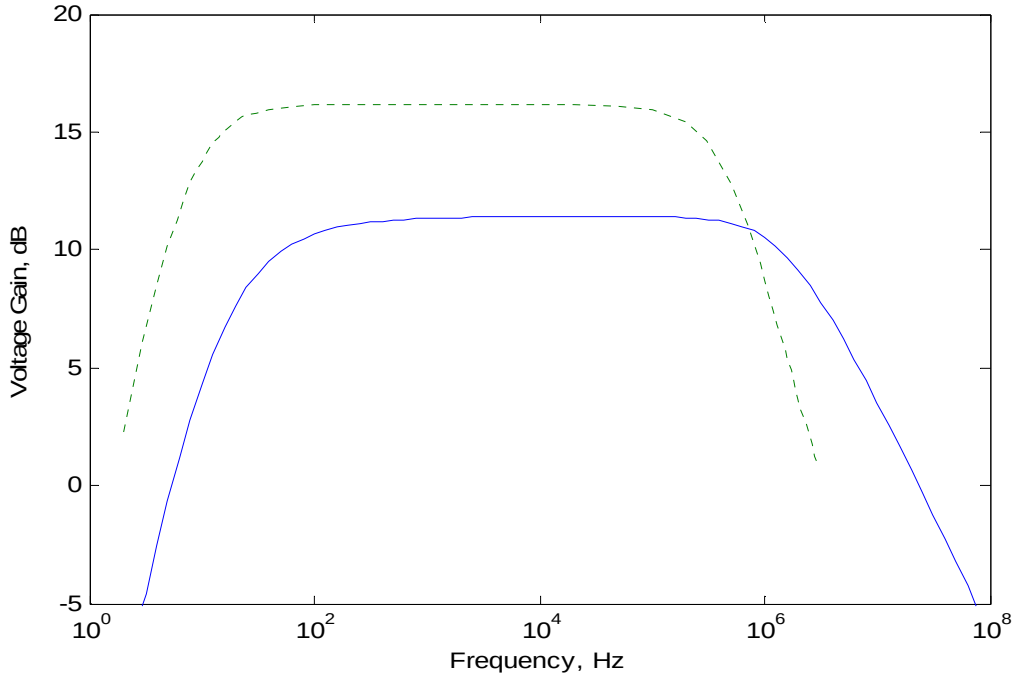

Fig. 45: Plot of voltage gain in dB versus frequency of an Inverter amplifier. Solid lines: theory; dotted lines: experiment.

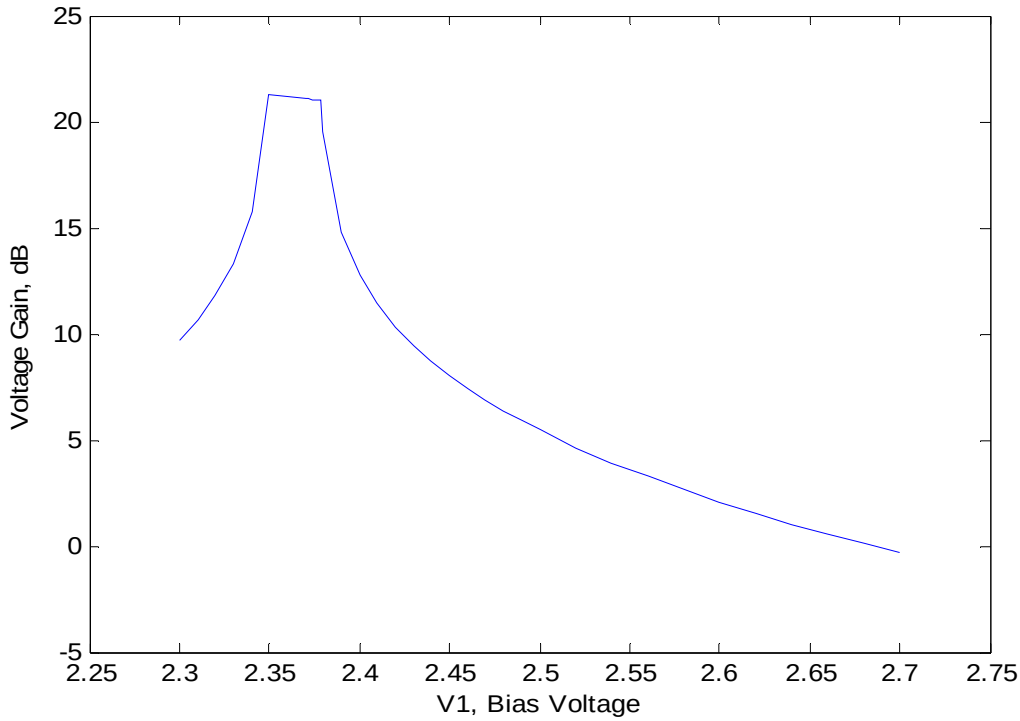

Fig. 46: Plot of small signal voltage gain in dB as a function of the bias voltage V1.

Fig. 45 shows the plot of voltage gain in dB versus frequency for an inverter used as a small signal amplifier. The dotted line represents the experimental data. We see that at mid band frequencies the experimental value of gain is 16 dB compared to the theoretical value of 11 dB. It can be seen from Fig. 41 that the transfer characteristic of the inverter in the transition region is very sharp. This means that the small signal voltage gain dv_0/dv_i is a sensitive function of the bias voltage. A plot of the small signal voltage gain as a function of the bias voltage V1 is shown in Fig. 46. We see that a small change in bias voltage from 2.41 volts to 2.38 volts can change the theoretical gain from 11 dB to 16 dB. Fig. 45 also shows that the experimentally measured bandwidth is less than the theoretically calculated value. This can be due to parasitic capacitances in the circuit.

3.6 Differential amplifier

Differential amplifiers are utilized to amplify and produce an output signal which is a function of the difference between two input signals and to thereby enable the detection of relatively weak signal levels while rejecting noise common on the differential input lines. In recent years, there has been an increasing demand for a system-on-chip configuration and reduction of power consumption, in response to which the MOS differential amplifiers have been widely used.

Fig. 47 shows the basic MOS differential amplifier configuration. M1 and M2, matched transistors, are biased by a constant current source. For initial discussion, assume that the current source is ideal. That is, its effective impedance is infinity.

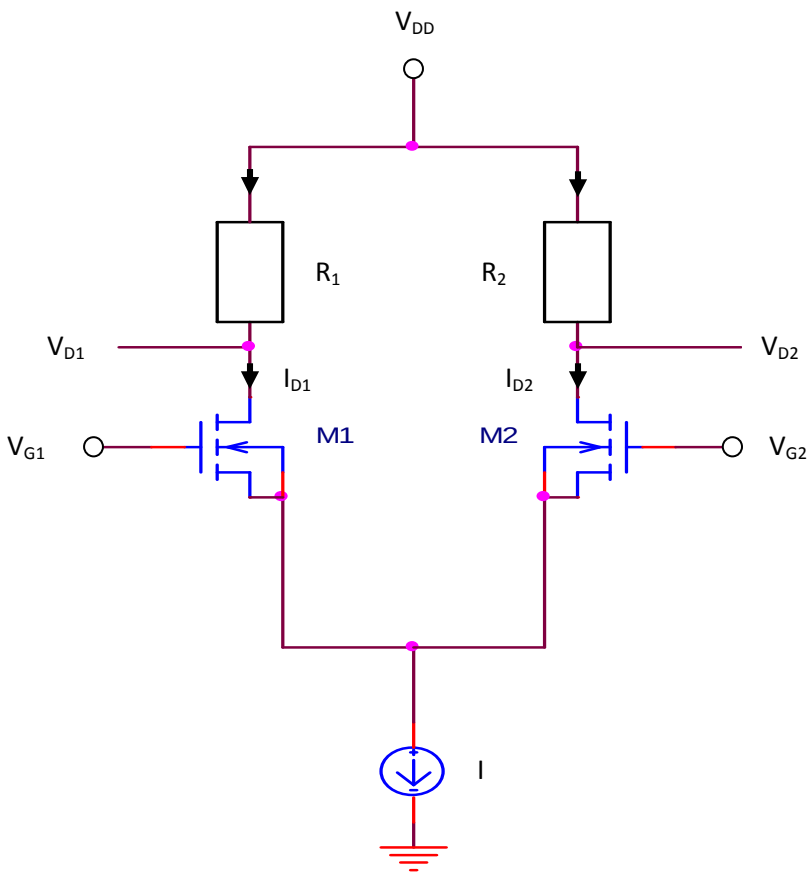

Fig. 47: Basic Differential amplifier with resistive loads.

Consider a case where two gate terminals are joined together and connected to a voltage $V_{G1} = V_{G2} = V_{CM}$. Since M1 and M2 are matched we can write

$I_{D1} = I_{D2} = I/2$, and

$V_{D1} = V_{D2} = V_{DD} - I_D R_D$

The differential output $V_0 = V_{D2} - V_{D1}$ will become zero. That is the differential pair does not respond to the common mode input. Thus the common mode gain A_{CM} should be equal to zero. Next, If the input voltage applied to V_{G1} and V_{G2} are not same, in this case the voltage applied to V_{G1} will cause a current to flow through R_1, but because of the circuit symmetry and balanced manner in which input is applied we observe that the

signal at the joint source connection must be zero, so that if V_{G1} goes up I_{D1} will go up and I_{D2} will go down such that the current through current source remains constant. Since the drain currents change, the output V_{D1} and V_{D2} will not be equal. Therefore the differential output V_0 will not be equal to zero. From the above it is clear that differential pair responds to difference mode or differential input signal between the two gates.

3.6.1 Constant Current Source

In this section we study the design of a constant current source. Two NMOS transistors of width-to-length ratio 30:1 were used to design the circuit shown in Fig. 48. The gate and drain of M3 transistor are tied together, forcing it to operate in the saturation region. When operating with common mode input voltage, to get 0.5 mA of drain current in each transistor of a MOS differential pair, the resistor R_D was designed to obtain drain current I_{D3} = 1 mA as shown in the figure below.

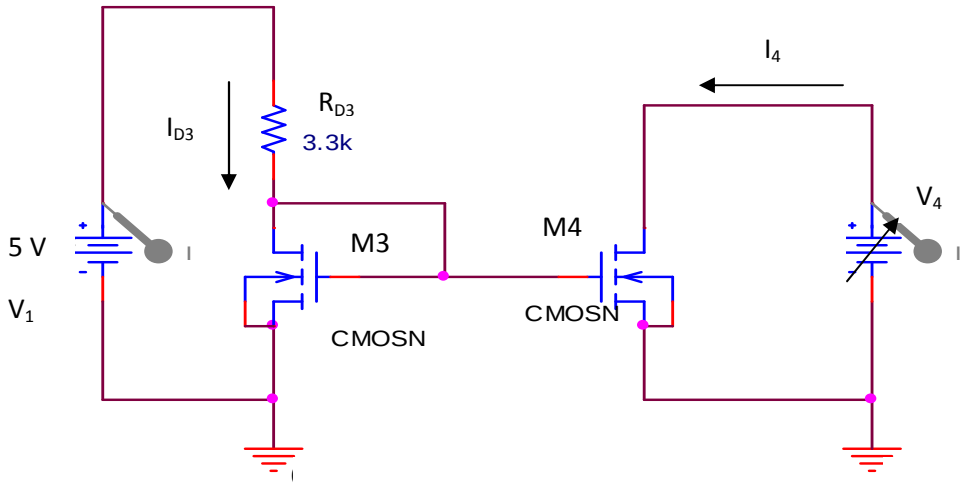

Fig. 48: Current mirror ciruit implementation using NMOS devices of width-to-length ratios 30:1.

Assuming that transistor M4 is operating in saturation region, its drain current I_4 will be same as I_{D3} for $V_4 \geq V_{GS}$. The theoretical and experimental results for output characteristics of a current mirror circuit are shown in Fig. 49. From Fig. 49 one can see

that, initially the drain current of transistor M4 is increasing with increase in V_4, for V_4 greater than or equal to 1.7 volts the plot of drain current is almost parallel to V_4 axis. The internal resistance of a constant current source R_{eff} is defined as the slope of the line I_4 versus V_4. From the data in Fig. 48, R_{eff} for our source was found out to be 50 kΩ.

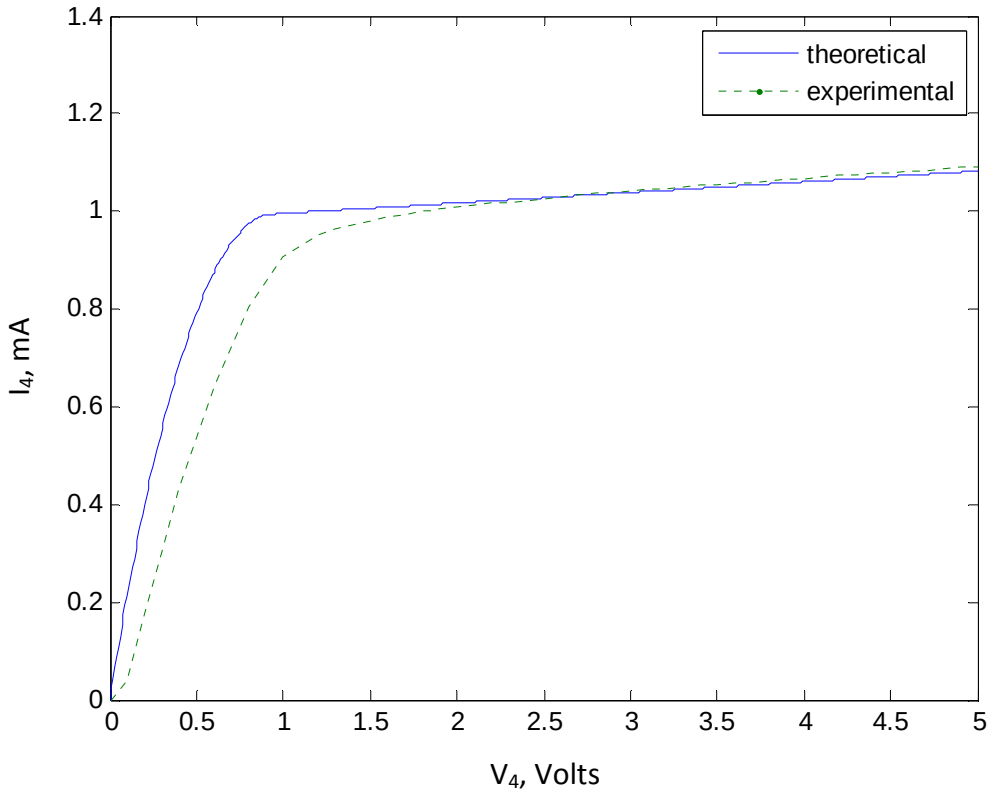

Fig. 49 : Output characteristics of a current mirror circuit.

3.6.2 Operation with a Differential input voltage

To study the response of the amplifier to a differential input signal the circuit was connected as shown in Fig. 50. Fixed postive 5 volts was applied to the gate of M2 transistor, that is V_{G2} = 5 volts. By sweeping the gate voltage V_{G1} from 4.5 volts to 5.5 volts in steps of 0.1 volts, the voltage across drains V_{D1} and V_{D2} was measured. In Fig. 50

transistor M3 and M4 form a circuit that act as a constant current source. This circuit is same as the one that has been explained in previous section.

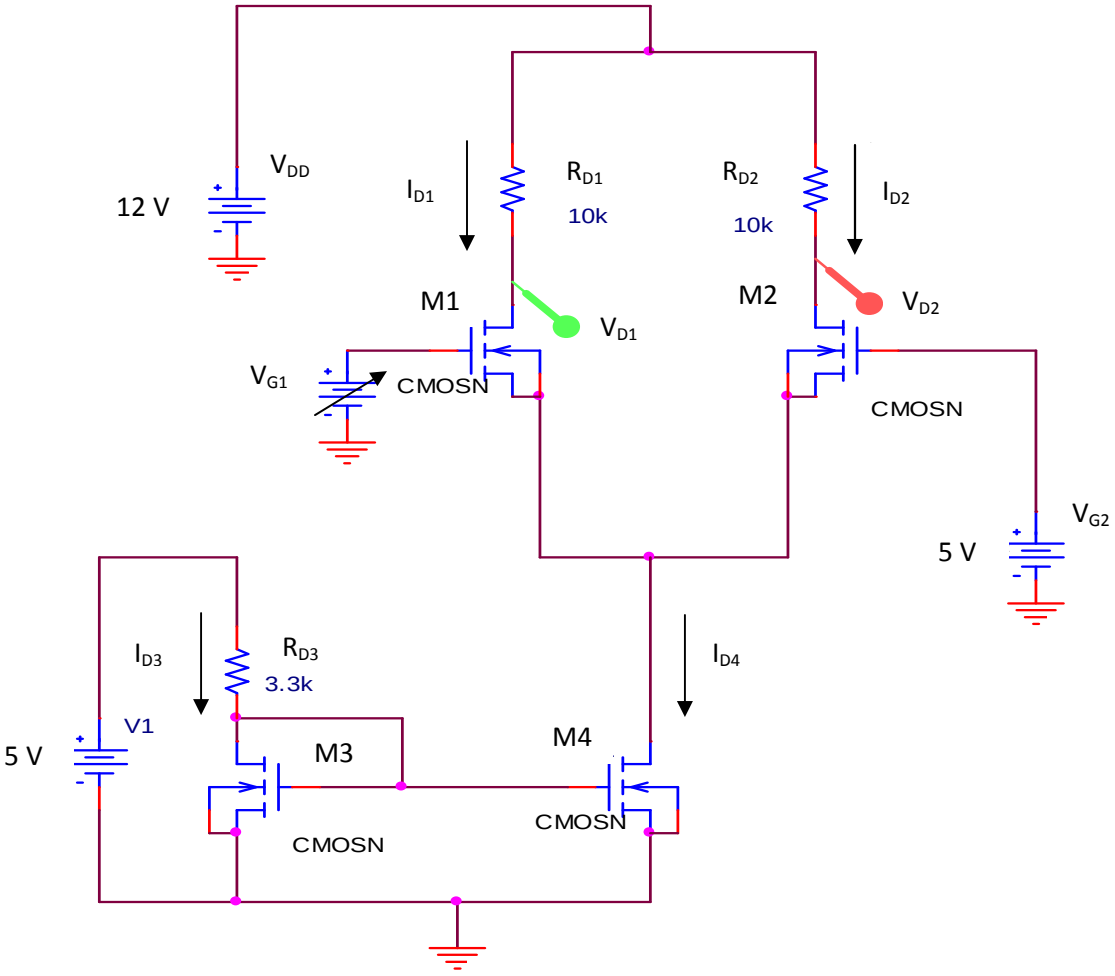

Fig. 50: MOS Differential amplifier implementation using NMOS devices of W/L = 30:1.

Let the differential input voltage $V_{id} = (V_{G1} – V_{G2})$. Then if V_{id} is positive, V_{G1} will be grater than V_{G2} and hence I_{D1} will be greater than I_{D2} and difference output voltage ($V_{D2} – V_{D1}$) will be positive. On the other hand, when V_{id} is negative, V_{G1} will be lower than V_{G2}, I_{D1} will be smaller than I_{D2}, and correspondingly difference output voltage ($V_{D2} – V_{D1}$) will be negative.

The theoretical and experimental values of drain voltages V_{D1} and V_{D2} versus V_{G1}, for V_{G2} fixed at 5 volts are shown in Fig. 51 and 52. It can be seen from these figures, that when V_{G1} increases the drain current I_{D1} increases and therefore V_{D1} decreases. On the other hand, V_{D2} increases with the rise in V_{G1} because I_{D2} decreases. Fig. 53 shows the theoretical and experimental plots of difference output voltage ($V_{D2} - V_{D1}$) versus V_{G1}.

The differential gain A_d of a differential amplifier can be defined as the ratio of the change in output voltage to the change in input voltage. That is,

$$A_d = \frac{(V_{D2} - V_{D1})}{(V_{G1} - V_{G2})}$$

From experimental measurements, the differential gain A_d was found out to be 7.34.

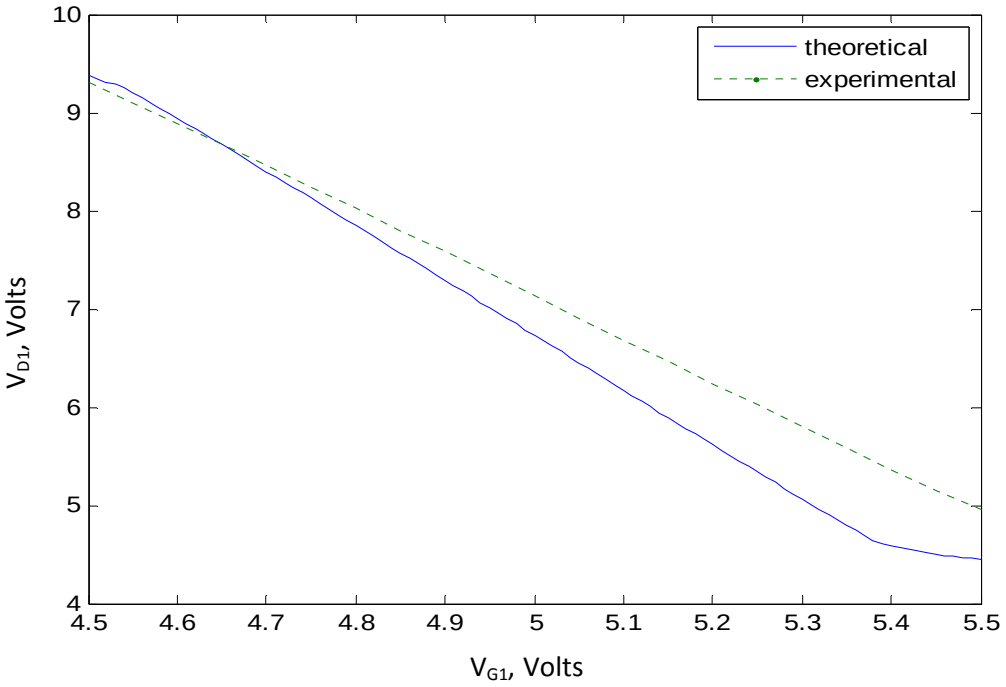

Fig. 51: Drain voltage V_{D1} versus gate voltage V_{G1} for V_{G2} = 5 volts.

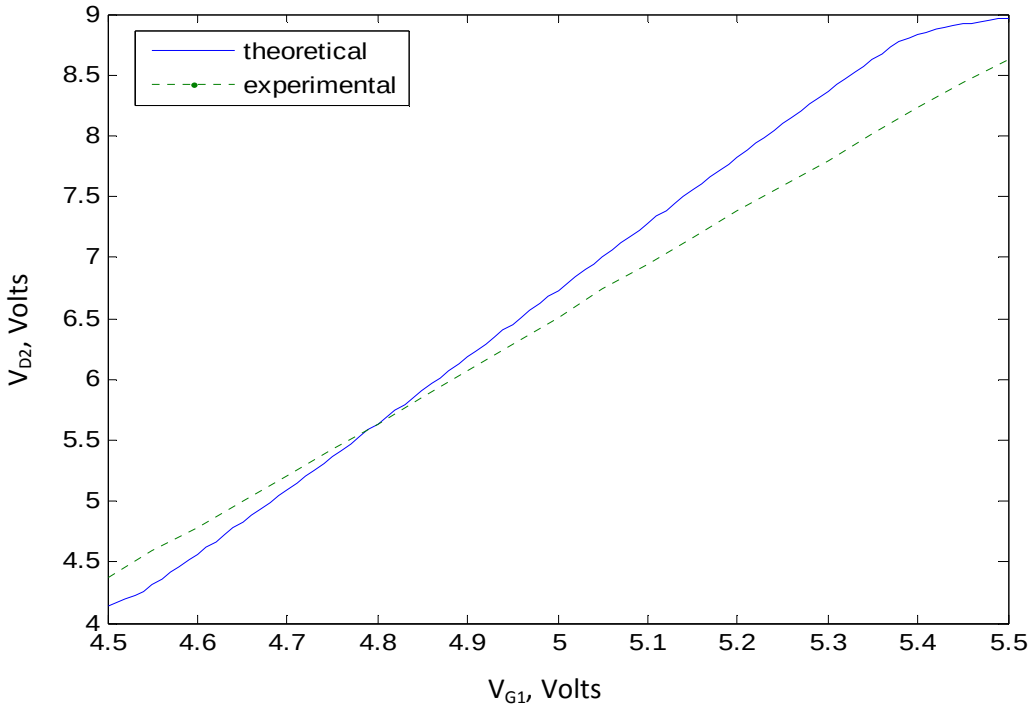

Fig. 52: Drain voltage V_{D2} versus gate voltage V_{G1} for $V_{G2} = 5$ volts.

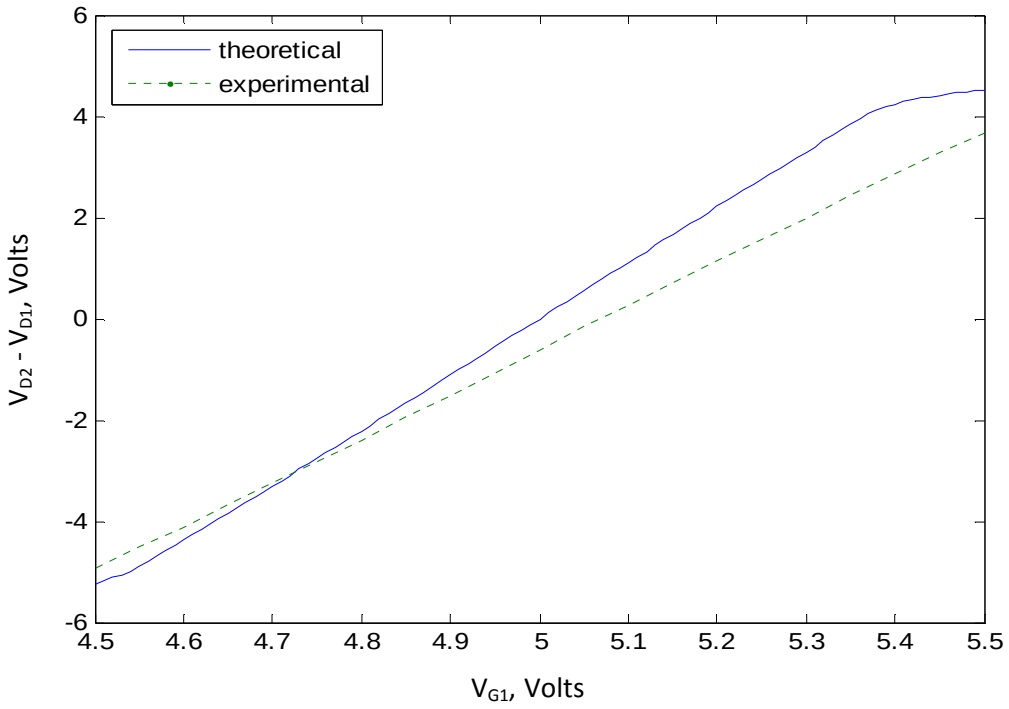

Fig. 53: Difference output voltage, ($V_{D2} – V_{D1}$) versus gate voltage V_{G1} for $V_{G2} = 5$ volts.

3.6.3 Operation with a common-mode input voltage

To study the operation of a differential amplifier with a common-mode input voltage V_{CM}, the circuit was connected as shown in Fig. 54 below.

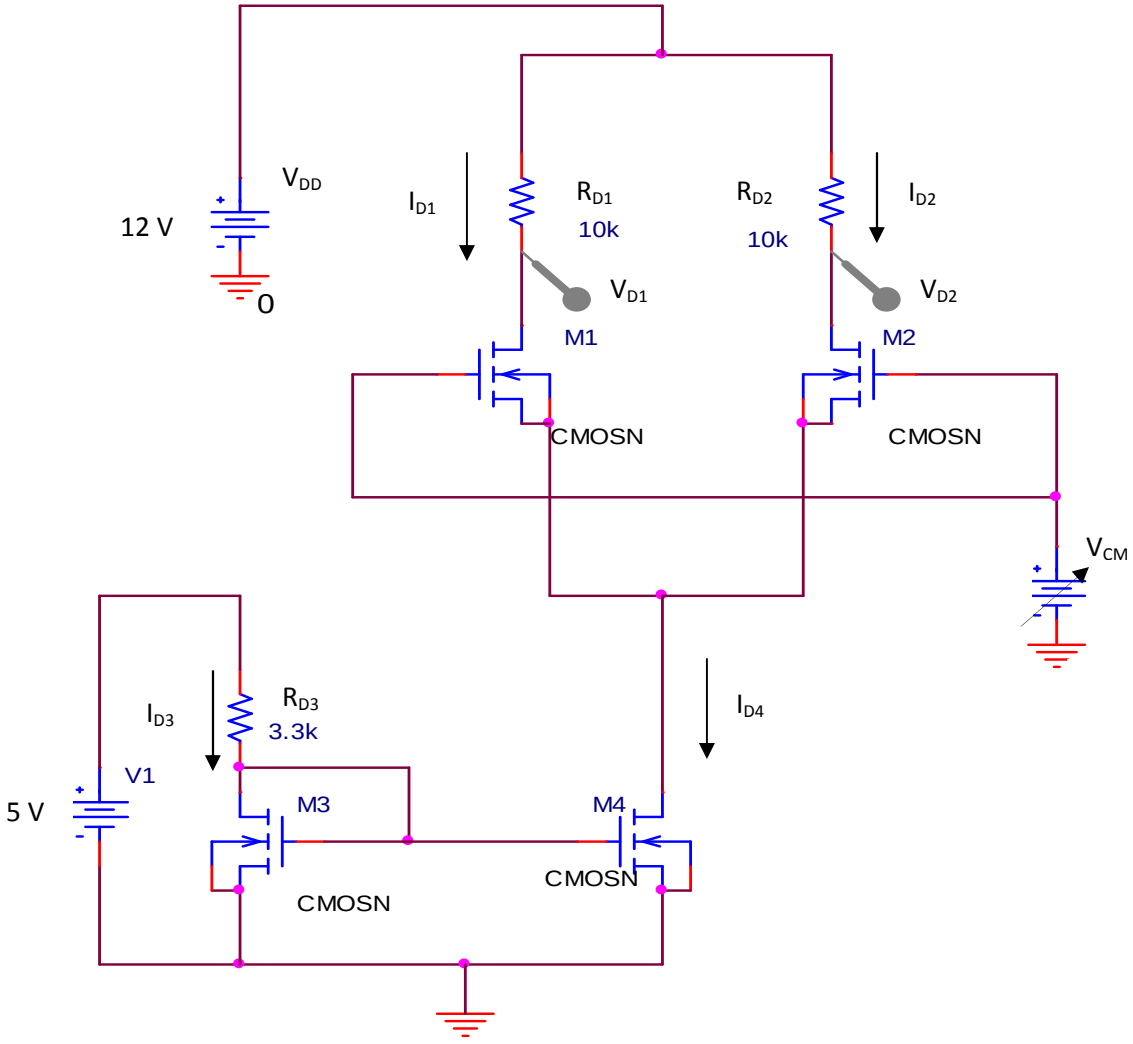

Fig. 54: MOS differential using NMOS devices having W/L = 30 with a common-mode input voltage.

For transistors M1 and M2 to operate in the saturation region, common-mode input voltage ranging from 3.5 volts to 7 volts has been applied. The theoretical and experimental results of drain currents I_{D1}, I_{D2} and drain voltages V_{D1}, V_{D2} versus

common-mode input voltage V_{CM} are shown in Figs 55 through 58. One can see that the drain currents I_{D1} and I_{D2} increase slightly with increase in the common-mode input voltage V_{CM}, thus, reducing the drain voltages V_{D1} and V_{D2}.

The common-mode gain A_{CM} is defined as,

$$A_{CM} = \frac{\Delta V_{D1}}{\Delta V_{CM}} \ or \ \frac{\Delta V_{D2}}{\Delta V_{CM}}$$

From experimental data obtained, the common-mode gain A_{CM} was found out to be -0.13.

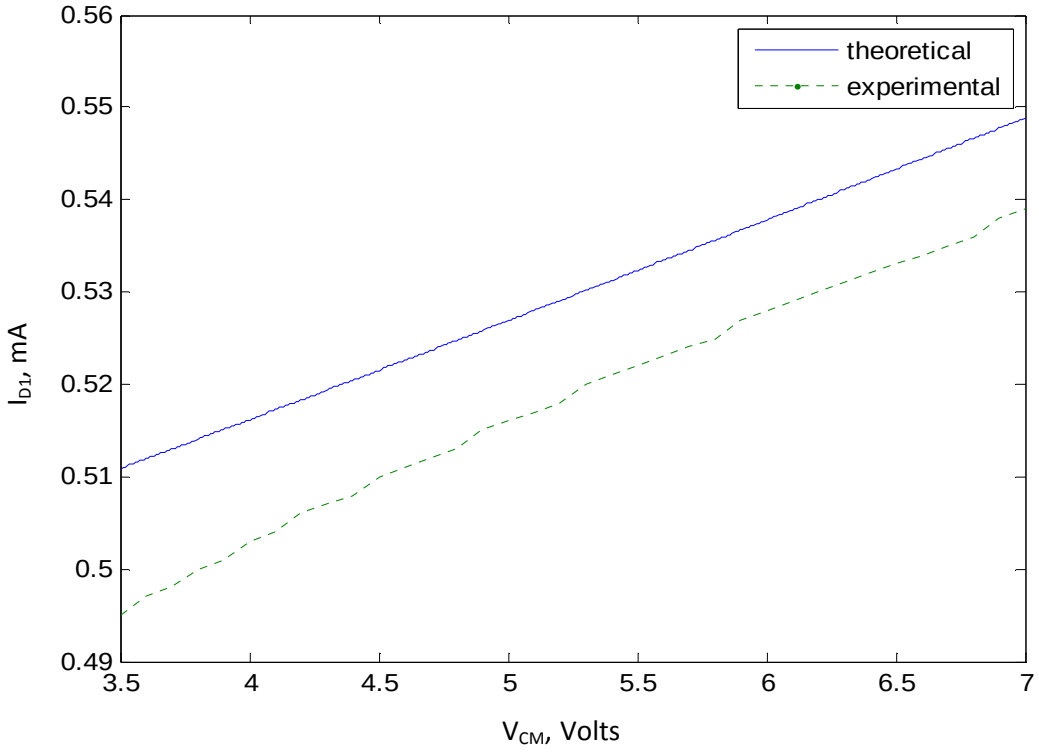

Fig. 55 : Drain current I_{D1} versus common-mode input voltage V_{CM}.

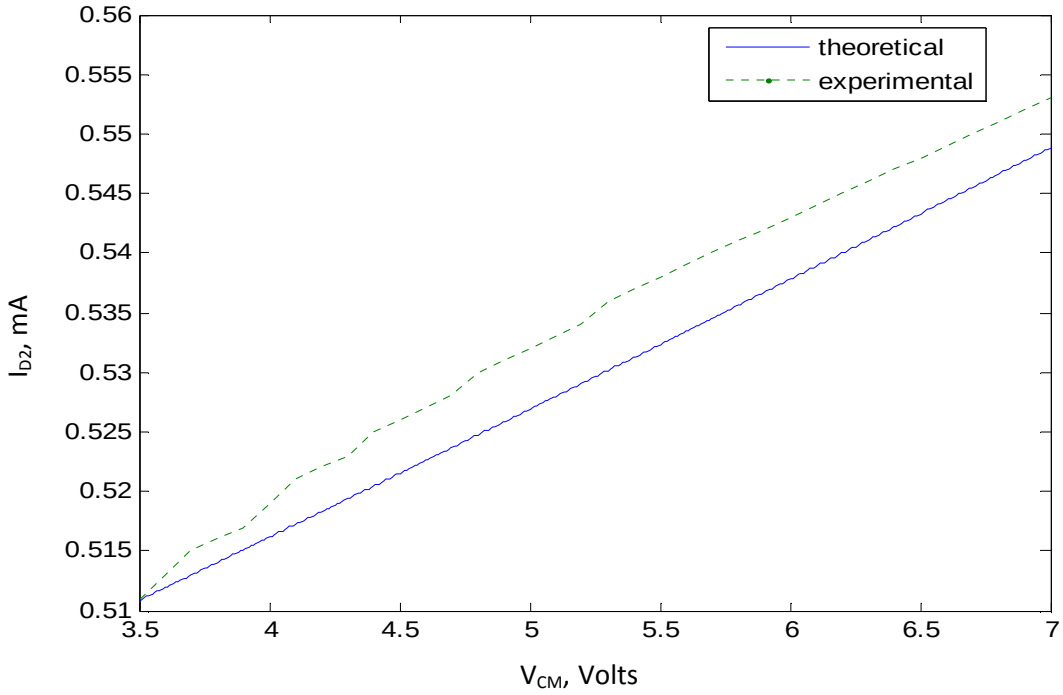

Fig. 56: Drain current I_{D2} versus common-mode input voltage V_{CM}.

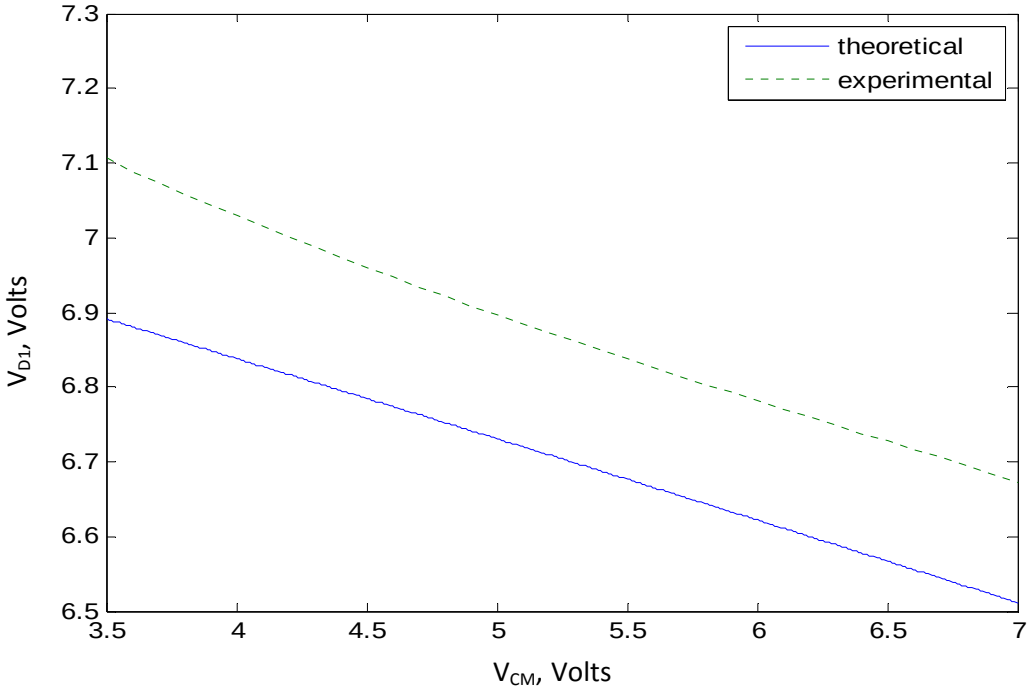

Fig. 57: Drain voltage V_{D1} versus common-mode input voltage V_{CM}.

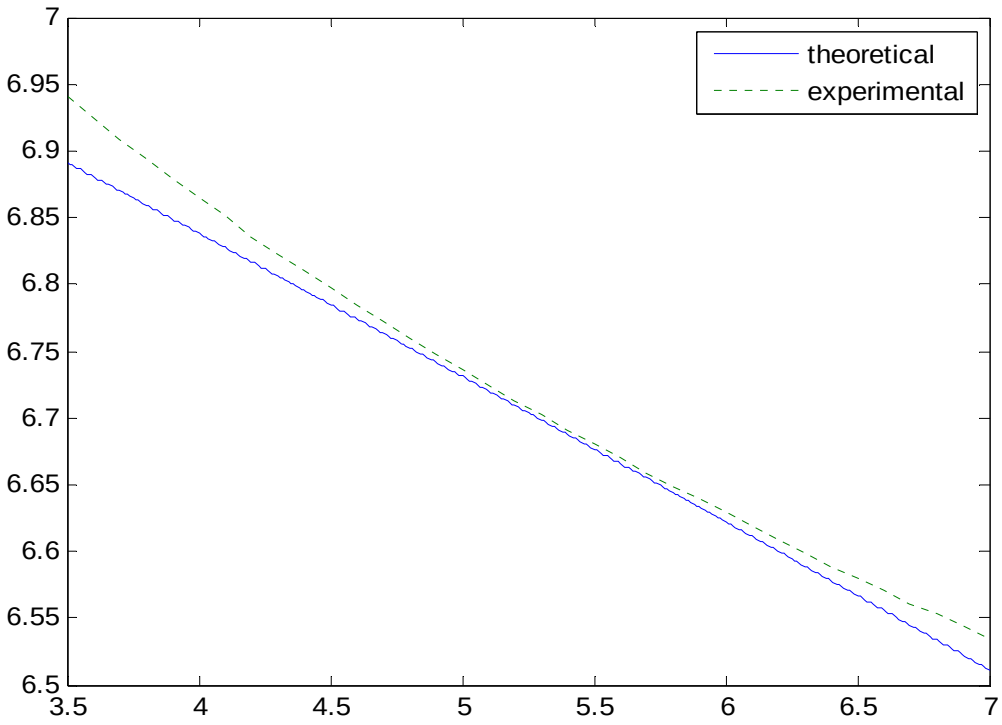

Fig. 58: Drain voltage V_{D2} versus the common-mode input voltage V_{CM}.

3.6.4 Hand calculations for A_{CM} and A_d

The equation to calculate common-mode gain is given by

$$A_{CM} \approx -\frac{R_D}{2R_{eff}}$$

where R_D is the drain resistance of a differential pair and R_{eff} is the internal resistance of the current source.

Similarly, the equation to calculate differential gain is given by

$$A_d = g_m R_D$$

where g_m is the transconductance of a NMOS device in a differential pair which can be given as $g_m = \Delta I_D / \Delta V_{GS}$ and R_D is the drain resistance.

Substituting the values of R_D= 10 KΩ, R_{eff}= 50 KΩ, and g_m= 1.17×10^{-3} A/V, we get common-mode gain A_{CM}= - 0.1 and differential gain A_d= 11.7. As stated earlier the experimental values were found out to be A_{CM}= - 0.13 and A_d = 7.34.

3.7 AC analysis of a common-mode differential amplifier

In this section, we study AC analysis of a common-mode differential amplifier that has been explained in the section 3.5.3. The circuit was connected as shown in Fig. 59. To operate both devices of a differential pair in saturation region the common mode input was biased to 5 volts DC through resistors R1 and R2. A sinusoidal signal of 50 mV amplitude was applied as input as shown in Fig. 59 below. The output was measured across a parallel RC load. For a 100 kHz voltage signal, the input and output waveforms measured on an oscilloscope are shown in Fig. 60. In Fig. 60, the input signal was measured by channel 1 of the oscilloscope where as the output signal by channel 2 across the 10 kΩ resistor in parallel with 47 pF capacitor. Fig. 61 shows the theoretical and experimental plots of voltage gain in dB versus frequency of a common-mode differential amplifier. For mid band frequencies, the experimental gain is 7 dB compared to the theoretical value of 9 dB. The experimentally measured bandwidth is less than the theoretically calculated value. Again, this could be due to parasitic capacitances in the circuit.

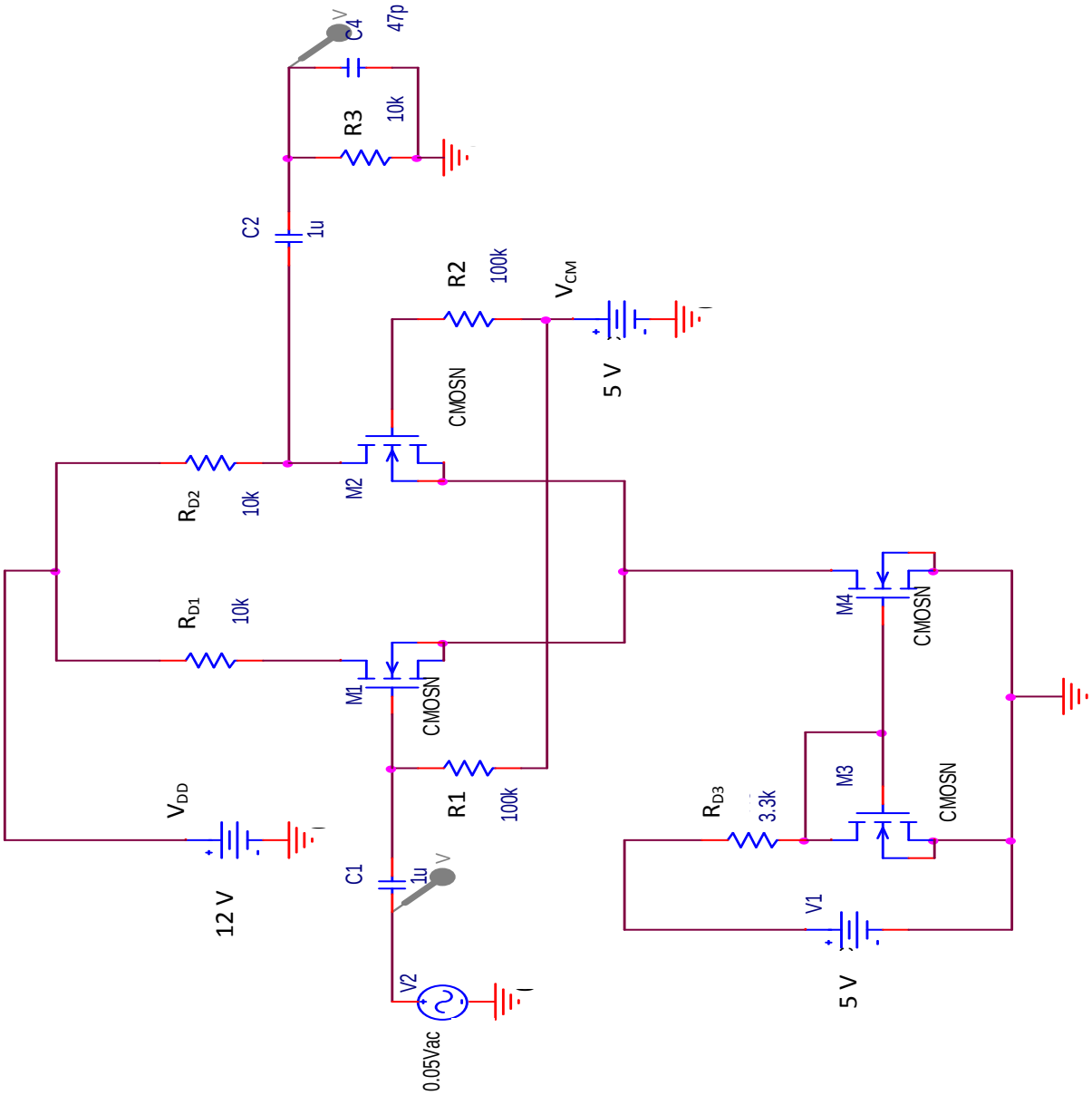

Fig. 59: Small signal analysis for a common-mode differential amplifier with parallel RC load.

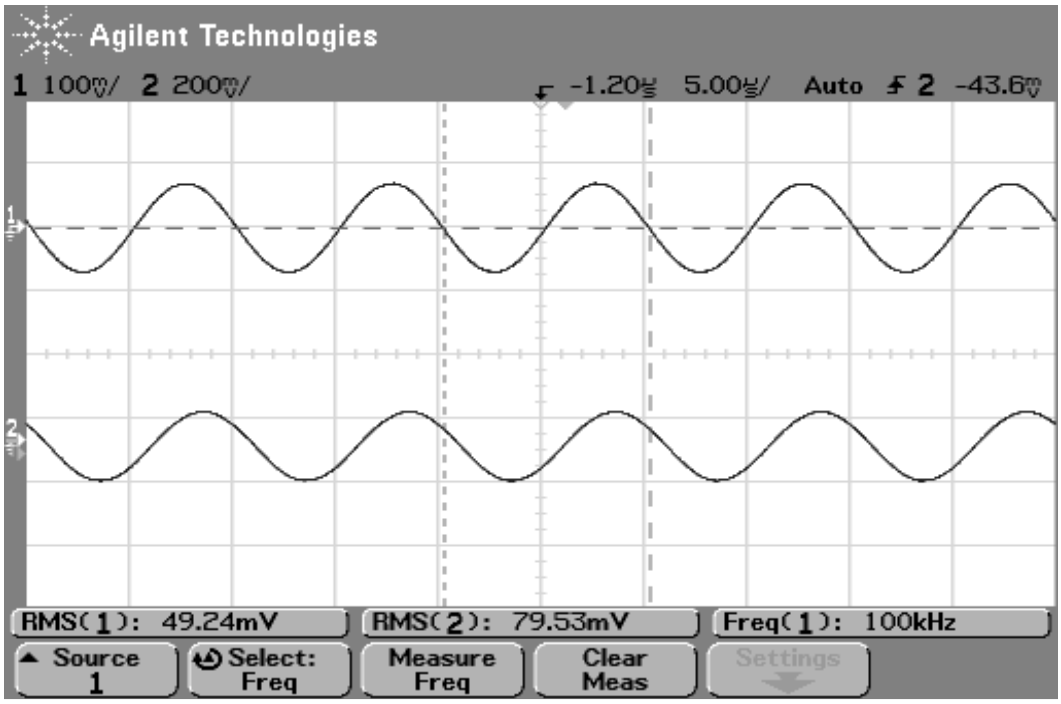

Fig. 60: Input and output voltage waveforms of a common-mode differential amplifier at 100 KHz frequency.

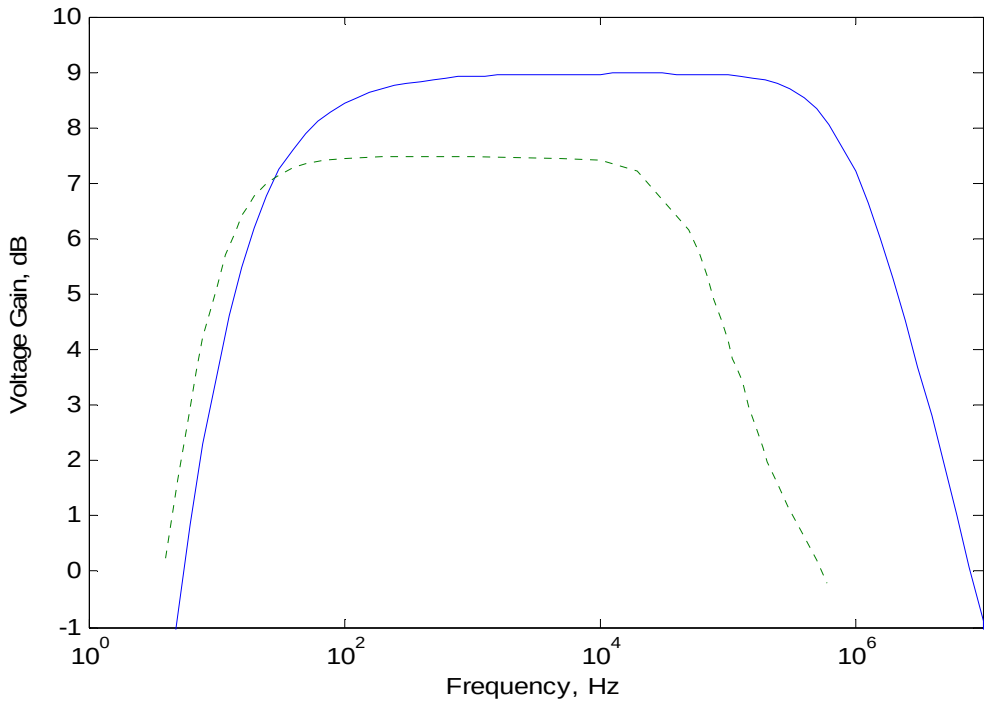

Fig. 61: Plot of voltage gain (in dB) versus frequency of a common-mode differential amplifier. Solid lines: theory; dotted lines: experiment.

3.8 CMOS Logic circuits

CMOS has been considered as an excellent technology for designing digital integrated ciruits. The reason is quite simple, MOSFETs are small, allowing for high-density logic networks, and switching circuits are straightforward to design. In this section we will examine a few basic logic circuits. By using these logic circuits a frequency counter was designed.

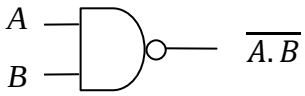

Fig. 62: A schematic symbol of a 2-input NAND gate.

3.8.1 A 2-input NAND gate

To start with, we designed a 2-input NAND gate using NMOS and PMOS transistors of width-to-length ratios 10. The schematic symbol of a 2-input NAND gate is shown in Fig. 62. For a 2-input NAND gate, two NMOS devices were connected in series and two PMOS devices were connected in parallel as shown in Fig. 63. The NMOS devices provide a path from the output to ground if and only if both *A* and *B* are equal to 1; otherwise, at least one of the NMOS device is OFF and the output has a conduction path to the power supply V_{DD} through one of the PMOS devices. For experimental analysis, we have set V_{DD} = 5 volts. By varying the inputs of a 2-input NAND gate, output has been measured. The truth table of a 2-input NAND gate is shown in Table 1. From Table 1 one can see that the output of a NAND gate will become zero if and only if both inputs are equal to V_{DD}.

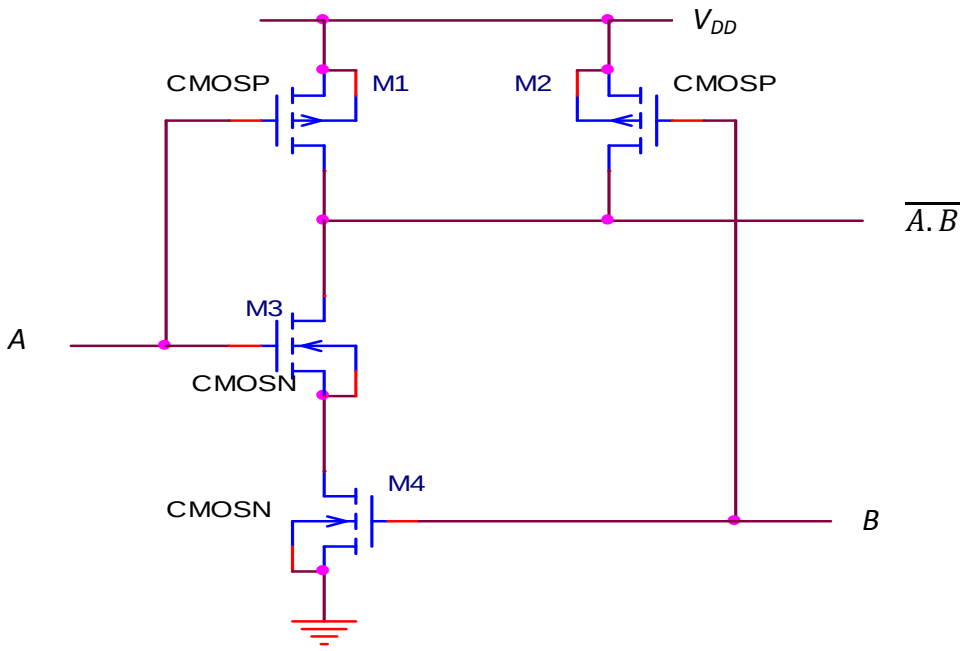

Fig. 63: CMOS 2-input NAND logic gate.

A	***B***	$\overline{\boldsymbol{A.B}}$
0	0	1
0	1	1
1	0	1
1	1	0

Table 1: Truth table of a 2-input NAND gate.

3.8.2 The D flip-flop

By using 2-input NAND gates we designed a D flip-flop as shown in Fig. 64. A latch can be defined as a one bit storage element, whereas a flip-flop is a latch controlled by a clock (*CLK*) input. In order for a logic circuit to store and retain its logic state even

after the controlling input signal has been removed, it is first necessary for the circuit to have some form of feedback, and secondly it should also have some additional input that can be used to change the logic states if necessary. Because of this reason, one will choose either NAND gates or NOR gates over inverters to form a latch.

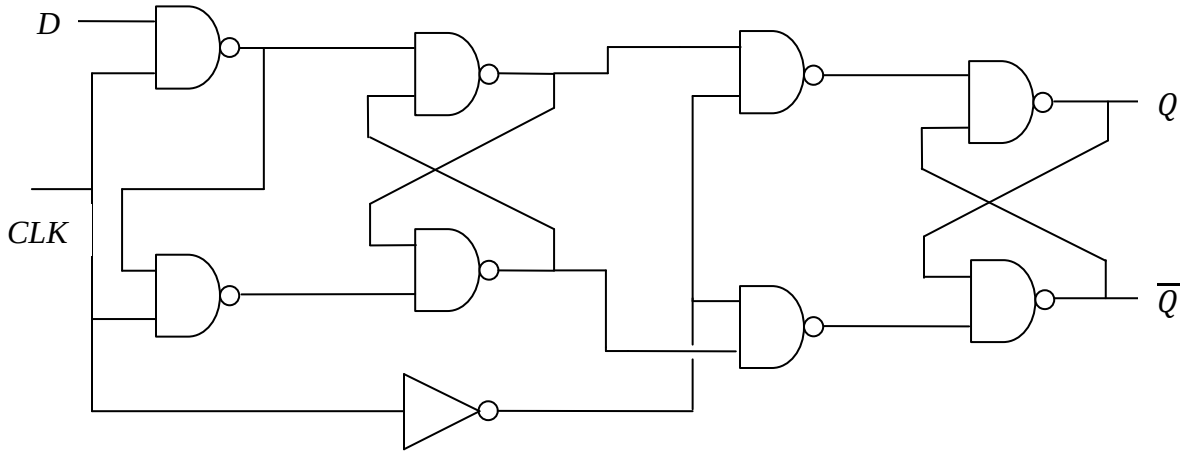

Fig. 64: A D flip-flop.

The output of a D flip-flop will change its state only when the clock input falls to 0 or else the output will hold the last state. Also the output always takes on the state of the D input at the moment when the clock input falls from 1 to 0.

3.8.3 T flip-flop and a 4 bit counter

Next, to convert a D flip-flop into a T flip-flop the $\overline{Q}$ output of a D flip-flop was connected to its D input so that the D input should always tell the flip-flop to change state at each clock pulse. A schematic symbol of a T flip-flop is shown in Fig. 65 below.

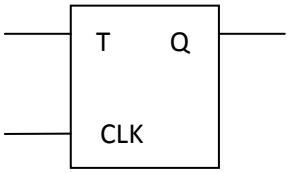

Fig. 65: Schematic symbol of a T flip-flop.

When the T input is at logic 0, change in clock CLK will have no effect on output Q so that means the output Q remains same. However, when T is at logic 1 output toggles with the clock input. Table. 2 shows the experiemental results obtained. The arrow represents the change in output state when the clock input falls from 5 to 0 V. One can see that the experimental results obtained are in agreement with theory. Also from the table one can see that a T flip-flop can work as a 1 bit counter.

To design a 4 bit counter, four T flip-flops were connected in cascade as shown in Fig. 66 below. The T inputs of all flip-flops are at logic 1 and the output of each flip-flop will trigger the next flip-flop. The count held by this counter is read in the reverse order from the order in which the flip-flops are triggered. Thus, output *D* is the high order of the count, while output *A* is the low order. The binary count held by the counter is then *DCBA*, and runs from 0000 (decimal 0) to 1111 (decimal 15). The counter circuit described above was designed and fabricated. Unfortunately, the circuit did not work as calculated. It was found that only the first flip-flop was responding to clock input, while the outputs of the other three flip-flops did not show any change in response to the clock input. The reasons for this are not clear to us at this time.

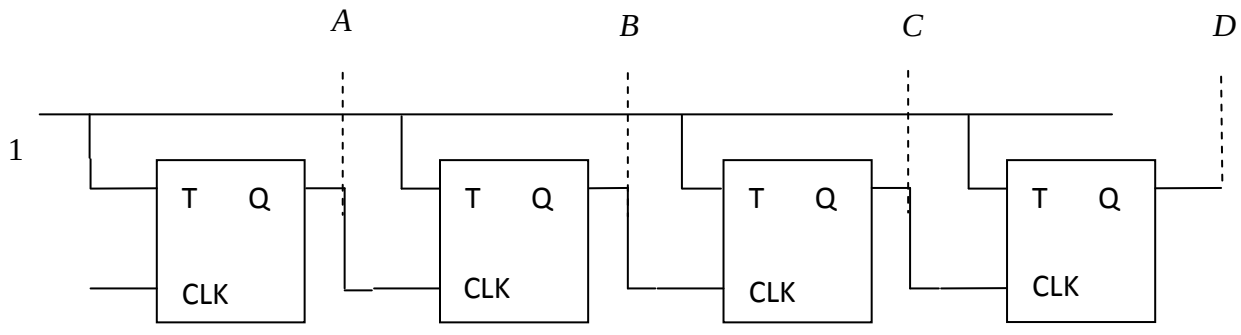

Fig. 66 : A 4 bit counter implementation using T flip-flops.

CLK	T	Q
0	0	1
1	0	1
0	0	1
1	0	1
0	1	0
1	1	0
↓ 0	1	1
1	1	0
↓ 0	1	1

Table 2: Truth table of a T flip-flop.

Chapter 4

Summary and Conclusions

This thesis has investigated the characteristics of acoustic waves propagating in a thin piezoelectric plate that is in contact with a fluid medium. It is found that, under suitable conditions, acoustic wave propagating in a piezoelectric plate can efficiently radiate a bulk acoustic wave in the surrounding fluid. This effect has potential applications for use in ultrasonic flow meters and for development of air-coupled ultrasonic transducers. Another part of the thesis is design and fabrication of an ASIC (Application Specific Integrated Circuit) chip containing an amplifier and a frequency counter suitable for use with acoustic wave transducers and sensors.

In chapter 1, general properties of acoustic waves that can propagate in solid materials are discussed. The applications of acoustic wave devices in the fields of sensing and signal processing are mentioned. The advantages of thin plate wave devices over other types of acoustic wave devices are described. The chapter concludes with a brief discussion of the application of mode conversion principle to realize miniature, high efficiency transducers for use in ultrasonic flow meters.

In chapter 2, propagation of acoustic waves in a piezoelectric plate which is in contact with a fluid medium is investigated theoretically. After applying the boundary conditions on the piezoelectric plate surfaces, the resultant 10×10 matrix is modified into an 8×8 matrix to simplify the calculations. A new method is proposed to calculate the velocity and attenuation of the plate waves. It consists of making the choice between

increase or decrease in the amplitudes of mechanical variables in the bulk of the fluid depending on whether the plate wave velocity is greater than or less than bulk wave velocity in the fluid. For the case of acoustic wave propagating in a 128 Y-X lithium niobate plate loaded with water on one side, it was found that conversion efficiency greater than 2 dB per wavelength can be obtained for values of *hf* (h = plate thickness, f = acoustic wave frequency) lying between 220 and 750 m/s. Analysis of water loading effect on other two widely used substrates, namely lithium tantalate and quartz, also shows strong coupling between plate and bulk acoustic waves. The analysis of wave propagation for the case where the fluid is a gas such as air, for example, shows that the plate wave can radiate bulk wave in the surrounding air. The coupling in this case is weaker than in the case of a liquid contacting the plate surface. Nevertheless, this effect may find applications for generation and detection of ultrasonic waves in air.

Chapter 3 begins with a brief introduction to the subject of Application Specific Integrated Circuits (ASICs). A number of NMOS and PMOS transistors have been fabricated and their characteristics studied theoretically and experimentally. The next topic studied is the voltage transfer characteristics of CMOS inverters having NMOS and PMOS devices of various aspect ratios. The use of a CMOS inverter as a small signal amplifier is investigated. Small signal voltage gain of 16 dB was obtained at a frequency of 100 kHz. Using the NMOS and PMOS transistors fabricated in the chip a differential amplifier with externally connected resistive loads was set up. The experimental values of differential mode gain A_d and common mode gain A_{CM} were found to be A_d = 7.34 and A_{CM}= 0.13, compared to the calculated values of A_d= 11.7 and A_{CM}= 0.1, respectively. Next, we studied use of this amplifier for amplifying a.c. signals. At a signal

frequency of 10 kHz, voltage gain of 7 dB was obtained compared to the theoretical value of 9 dB. Next the implementation of a 2-input NAND gate is explained. By using NMOS transistors having W/L values of 10:1 a 2-input NAND gate was designed and fabricated. The next topic deals with the design of a D flip-flop using NAND gates and a CMOS inverter. It is shown that by small modification a D flip-flop can be converted to a T flip-flop or a 1-bit counter. Finally, the implementation of a 4-bit counter by cascading four 1-bit counters is briefly explained.

The work described in this thesis has shown that an acoustic wave propagating in a thin piezoelectric plate can be used to generate bulk acoustic waves in a liquid or a gaseous medium. One of the important applications of this effect can be for realization of miniature, high efficiency transducers for use in ultrasonic flow meters. More theoretical and experimental work is required to develop these transducers. The generation of waves in air should also be investigated in more detail to study the feasibility of using this approach for development of air-coupled transducers.

REFERENCES

1. S. G. Joshi and B. D. Zaitsev, “Low Profile Transducer for Flow Meters”, U. S. Patent 6,609,430.

2. S. G. Joshi, B. D. Zaitsev, and I. E. Kuznetsova, “Miniature, high efficiency transducers for use in ultrasonic flow meters,” J. Appl. Phys., vol. 105, 034501, 2009.

3. B. Drafts, “Acoustic Wave Technology Sensors,” IEEE Trans. Microwave Theory and Techniques, vol. 49, No. 4, pp. 795-802, Apr. 2001.

4. R. J. Besson, J. M. Groslambert, and F. L. Walls, “Quartz crystal resonators and oscillator-recent developments and future trends,” Ferroelectrics, vol. 43, pp. 57-65, 1982.

5. W. H. King Jr., “Piezoelectric sorption detector,” Anal. Chem., vol. 36, No. 9, pp. 1735-1739, Aug. 1964.

6. H. Lamb, “On waves in an elastic plate,” Proc. Roy. Soc. London, Series A, vol. 93, pp. 114-128, 1917.

7. K. Toda, “Lamb-wave delay lines with interdigital electrodes,” J. Appl. Phys, vol. 44, pp. 56-62, Jan. 1973.

8. K. Toda, “Frequency characteristics of an interdigital transducer for Lamb wave excitation,” J. Appl. Phys, vol. 45, pp. 5136-5140, Dec. 1974.

9. R. S. Wagers, “Spurious acoustic responses in SAW devices,” Proc. of the IEEE, vol. 64, No. 5, pp. 699-702, May 1976.

10. R. S. Wagers, “Plate modes in surface acoustic wave devices,” in “Physical acoustics,” ed. by W.P. Mason and R.N. Thurston, New York, Academic Press, vol. 13, pp. 49-78, 1977.

11. T. M. Niemczyk, S. J.Martin, G. C. Frye, and A. J. Ricco, “Acoustoelectric interaction of plate modes with solutions,” J. Appl. Phys., vol. 64, pp. 5002-5008, 1988.
12. S. J. Martin, A.J. Ricco, T.M. Niemczyk, G.C. Frye, “Characterization of SH acoustic plate mode liquid sensors,” Sensors and Actuators, vol. 20, pp. 253-268, 1989.

13. J. C. Andle and J. F. Vetelino, “Acoustic wave – based biosensors,” Sensors and Actuators A, vol. 44, No.3, pp. 167-176, 1994.

14. J. C. Andle, J. F. Vetelino, M. W. Lade, and D. J. McAlister, “An acoustic plate mode biosensor,” Sensors and Actuators B, vol. 8, pp. 191-198, 1992.

15. S. W. Wenzel and R. M. White, “Analytical comparison of the sensitivities of bulk-wave, surface-wave, and flexural plate-wave ultrasonic gravimetric sensors,” Appl. Phys. Lett., vol. 54, pp. 1976-1978, May 15, 1989.

16. S. W. Wenzel and R. M. White, “A multisensor employing an ultrasonic Lamb-wave oscillator,” IEEE Trans. Electronic Devices, vol. 35, pp. 735-743, June 1988.

17. B. J. Costello, B. A. Martin and R. M. White, “Ultrasonic plate waves for biochemical measurements,” Proc. IEEE Ultrasonics Symposium, pp. 977-981, 1989.

18. N. Tirole, D. Hauden, and G. Martin, “Lamb waves pressure sensor using an AlN/Si structure,” Proc. IEEE Ultrasonics Symp., pp. 371-374, 1993.

19. M. J. Vellekoop, G. W. Lubking, and A. Venema, “Acoustic-wave based monolithic microsensors,” Proc. IEEE Ultrasonics Symposium, pp. 565-574, 1994.

20. C. E. Dube, J. O. Fiering, and M. J. Mescher, “A Si-based FPW sensor array system with polymer micro fluidics integrated on a PCB,” Proc. IEEE Sensors Conference, pp. 460-465, 2002.

21. B. D. Zaitsev, S. G. Joshi, and I. E. Kuznetsova, “Propagation of QSH acoustic waves in piezoelectric plates,” IEEE Transactions Ultrasonics, Ferroelectrics, and Freq. Control, vol. 46, No.5, pp. 1298-1302, Sept. 1999.

22. B. D. Zaitsev, S. G. Joshi, I. E. Kuznetsova, and I. A. Borodina, “Influence of conducting layer and conducting electrode on acoustic waves propagating in potassium niobate plates,” IEEE Trans. Ultrasonics, Ferroelectrics, and Freq.Control, vol. 48, pp. 624 - 626, March 2001.

23. B. D. Zaitsev, I. E. Kuznetsova, S. G. Joshi, and I. A. Borodina, “Shear horizontal acoustic waves in piezoelectric plates bordered with conductive liquid,” IEEE Trans. Ultrasonics, Ferroelectrics, and Freq. Control, vol. 48, pp. 627 - 631, March 2001.

24. S. G. Joshi, B. D. Zaitsev, and I. E. Kuznetsova, “Reflection of plate acoustic waves produced by a periodic array of mechanical load strips or grooves,” IEEE Trans. on Ultrasonics, Ferroelectrics, and Freq. Control, vol.49, No.12, pp. 1730-1734, 2002.

25. J. E. Hyslop and G. Hayward, “The study of lamb wave dispersion in piezoelectric plate transducers,” IEEE Ultrasonics Symposium, vol. 1, pp. 577-580, Oct 1999.

26. A. Gachagan and G. Hayward, “A flexible piezoelectric transducer design for efficient generation and reception of ultrasonic lamb waves,” IEEE Transactions on Ultrasonics, Ferroelectrics, and Freq. Control, vol. 52, no. 7, pp. 1175-1182, July 2005.

27. L. C. Lynnworth, “Ultrasonic Measurements for Process Control,” Academic Press, New York, 1989.

28. J. J. Campbell and W. R. Jones, “Propagation of surface waves at the boundary between a piezoelectric crystal and a fluid medium,” IEEE Transactions on Sonics and Ultrasonics, vol. SU-17, no. 2, pp. 71-76, April 1970.

29. S. G. Joshi, G. S. Nagaraj, B. D. Zaitsev, and I. E. Kuznetsova, “Efficient Mode Conversion Transducers for use in Ultrasonic Flow Meters,” Proc. IEEE International Ultrasonic Symposium, Rome (Italy), Sept. 2009, Paper ID 1491, doi: 10.1109.

30. M. C. Bhardwaj, “High transduction piezoelectric transducers and introduction of non-contact analysis,” NDT.net, Jan. 2000, vol. 5, No. 01. http://www.ndt.net/article/v05n01/bhardwaj

31. T. E. Gomez Alvarez-Arenas, “Acoustic impedance matching of piezoelectric transducers to air,” IEEE Transactions on Ultrasonics, Ferroelectrics, Freq. Control, vol. 51, pp. 624-633, May 2004.

32. T. E. Gomez Alvarez-Arenas, P. Yu Apel, and O. L. Orelovich, “Characterization of ion track membranes by non-contact ultrasonic magnitude and phase spectroscopy,” J. Membrane Science, vol. 301, pp. 201-220, 2007.

33. J. P. Uyemura, “Physical design of CMOS Integrated circuits using L-Edit,” PWS Publishing Company, Boston, 1995.

34. A. .S. Sedra and K. C. Smith, “Microelectronic Circuits,” 6th Edition, Oxford University Press, New York, 2010, pp. 1124-1127.

APPENDICES

Appendix A: Matlab program to calculate plate wave velocity

```
% fluid on top and vacuum in the bottom
%   Title: program for liq after bump velocity calculation for Y-X
Lithium niobate
clear  % clearing all previous commands
clc    %clearing Matlab command window
format long g   % floating-point format
count=1;
pcompare=1;  % max value of P for comparison
lambda1=1; % name representation of lambda for formulae
P=eye(8); % Unit matrix initialization
lambda=0;mu=218; theta=0;% Euler angles
lambda=lambda*pi/180;mu=mu*pi/180;theta=theta*pi/180; % changing degree
into radians
ep0=8.854187817*10^-12; % Absolute value of permittivity
ro=4628;% density of material kg/m3
cxy=(10^11)*[ 1.9839    0.5472  0.6513    0.0788   0         0;
              0.5472    1.9839  0.6513   -0.0788   0         0;
              0.6513    0.6513  2.279     0        0         0;
              0.0788   -0.0788  0         0.5965   0         0;
              0         0       0         0        0.5965    0.0788;
              0         0       0         0        0.0788    0.71835;];
% The elasticity constant N/m2
exy=[0     0     0        0     3.69        -2.42;
    -2.42  2.42  0        3.69  0            0;
```

```
    0.3    0.3   1.77     0     0            0;];
% piezoelectric constant in F/m
ep=(10^(-11))*[ 40.36     0       0;
                0        40.36    0;
                0        0       23.28;]; %dielectric constant in C/m2
T=[1 6 5;6 2 4;5 4 3]; % local matrix
for k=1:3% converting engineering notation to tensor notation
    for l=1:3
        for i=1:3
            for j=1:3
                m=T(k,l);  n=T(i,j);   %local variables
                c(k,l,i,j)=cxy(m,n);
            end
        end
    end
end
for k=1:3% converting engineering notation to tensor notation
    for i=1:3
        for j=1:3
            n=T(i,j);
            e(k,i,j)=exy(k,n);
        end
    end
end
a1=[cos(lambda) sin(lambda) 0 ; -sin(lambda) cos(lambda) 0; 0 0 1];
%1st euler rotation around z axis
a2=[1 0 0 ; 0 cos(mu) sin(mu); 0 -sin(mu) cos(mu)];
%2nd euler rotation around x' axis
a3=[cos(theta) sin(theta) 0 ;-sin(theta) cos(theta) 0; 0 0 1];
```

```
%3rd euler rotation around z'' axis
a=a3*a2*a1;% composite euler rotation matrix
for i=1:3 % initialization of rotated elasticity constant matrix
    for j=1:3
        for k=1:3
            for l=1:3
                cc(i,j,k,l)=0;
            end
        end
    end
end
for i=1:3  % initialization of rotated dielectric constant matrix
    for j=1:3
        for k=1:3
            ee(i,j,k)=0;
        end
    end
end
for i=1:3    % initialization of rotated piezoelectricity constant
matrix
    for j=1:3
        epp(i,j)=0;
    end
end
for i=1:3      % calculation of rotated elasticity constant matrix
    for j=1:3
        for k=1:3
            for l=1:3
                for r=1:3
```

```
                    for s=1:3
                        for t=1:3
                            for n=1:3

cc(i,j,k,l)=cc(i,j,k,l)+a(i,r)*a(j,s)*a(k,t)*a(l,n)*c(r,s,t,n);
                            end
                        end
                    end
                end
            end
        end
    end
end
for k=1:3% converting tensor notation to engineering notation
    for l=1:3
        for i=1:3.
            for j=1:3
                m=T(i,j);
                n=T(k,l);
    cf(m,n)=cc(i,j,k,l);
            end
        end
    end
end
for i=1:3 % calculation of rotated dielectric constant matrix
    for j=1:3
        for k=1:3
            for r=1:3
                for s=1:3
```

```
                    for t=1:3
   ee(i,j,k)=ee(i,j,k)+a(i,r)*a(j,s)*a(k,t)*e(r,s,t);
                    end
                end
            end
        end
    end
end
T=[1 6 5;6 2 4;5 4 3];
for k=1:3% converting tensor notation to engineering notation
    for i=1:3
        for j=1:3
            n=T(i,j);
            enew(k,n)=ee(k,i,j);
        end
    end
end
for i=1:3% calculation of rotated piezoelectric constant matrix
    for j=1:3
        for r=1:3
            for s=1:3  % epp is epsilon
                epp(i,j)=epp(i,j)+a(i,r)*a(j,s)*ep(r,s);
            end
        end
    end
end
cxy=cf; % rotated elastic constant
exy=enew;% rotated dielectric constant
ep=epp;% rotated piezoelectric constant
```

```
for k=1:3 % converting engineering notation to tensor notation
    for l=1:3
        for i=1:3
            for j=1:3
                m=T(k,l);
                n=T(i,j);
                c(k,l,i,j)=cxy(m,n);
            end
        end
    end
end
for k=1:3 % converting engineering notation to tensor notation
    for i=1:3
        for j=1:3
            n=T(i,j);
            e(k,i,j)=exy(k,n);
        end
    end
end
jj=sqrt(-1);
itrn=24;vstep=1;vstart=2845+63.8*jj;v=vstart; % velocity loop
hstart=0.4;hstep=0.1;hfinal=0.4;%thickness of the plate, h/wavelength,?
rhof=997.3;
c_liq=2.25*10^9;
v_liq=sqrt(c_liq/rhof);
bf=-sqrt(((rhof*v^2)-c_liq)/(c_liq));
epf=80*ep0;
for h=hstart:hstep:hfinal % h/? loop starts here
    if real(vstart)>v_liq
```

```
        v=vstart; % re-initialization of velocity loop for each h loop
        bf=-bf;
    end
    for vloop=1:itrn   % the velocity loop
        b=tf('s'); % decay constants variable
        for i=1:3 % lambda matrix declaration
            for j=1:3

L(i,j)=c(3,i,3,j)*b^2+(c(1,i,3,j)+c(3,i,1,j))*b+c(1,i,1,j);
            end
            L(i,4)=e(3,i,3)*b^2+(e(1,i,3)+e(3,i,1))*b+e(1,i,1);
            L(4,i)=L(i,4);
        end
        L(4,4)=-(ep(3,3)*b^2+(ep(1,3)+ep(3,1))*b+ep(1,1));
        for i=1:4
            for j=1:4
                if i==j
                    if i==4
                        A(i,j)=L(i,i);
                    else
                        A(i,j)=L(i,j)-ro*(v^2);
                    end
                else
                    A(i,j)=L(i,j);
                end
            end
        end
% calculation of determinant of lambda matrix
        inx=[2 3 4 ;1 3 4; 1 2 4;1 2 3;];
```

```
        DE=0;% initialization of determinant of lambda matrix
        for i=1:4
            j=inx(i,1);            k=inx(i,2);            m=inx(i,3);
D=A(2,j)*A(3,k)*A(4,m)+A(2,k)*A(3,m)*A(4,j)+A(3,j)*A(4,k)*A(2,m)-
A(2,m)*A(3,k)*A(4,j)-A(2,j)*A(4,k)*A(3,m)-A(2,k)*A(3,j)*A(4,m);
            DE=DE+(-1)^(i+1)*D*A(1,i);
        end
        [rot]=zero(DE); % roots of lambda matrix
        n=0;
        for k=1:size(rot)
            b=rot(k); % decay constants
            for i=1:3 % recalculation of lambda matrix with found b
                for j=1:3
Lx(i,j)=c(3,i,3,j)*b^2+(c(1,i,3,j)+c(3,i,1,j))*b+c(1,i,1,j);
                end
                Lx(i,4)=e(3,i,3)*b^2+(e(1,i,3)+e(3,i,1))*b+e(1,i,1);
                Lx(4,i)=Lx(i,4);
            end
            Lx(4,4)=-(ep(3,3)*b^2+(ep(1,3)+ep(3,1))*b+ep(1,1));
            for i=1:4
                for j=1:4
                    if i==j
                        if i==4
                            Ax(i,j)=Lx(i,i);
                        else
                            Ax(i,j)=Lx(i,j)-ro*(v^2);
                        end
                    else
                        Ax(i,j)=Lx(i,j);
```

```
                end
            end
        end
        n=n+1;
        ap=null(Ax);% eigenvectors B
        B(:,n)=null(Ax);
        clear Ax Lx
    end
    m=1;
    for k=1:size(rot)
        b(m)=rot(k);
        m=m+1;
    end%4
    [w1 w2]=size(b);
    if w2==8
        j=sqrt(-1);

        for n=1:8 %calculation of boundary condition matrix P
                for i=1:3
                    P(i,n)=(e(1,3,i)+e(3,3,i)*b(n))*B(4,n);
                  for k=1:3

     P(i,n)=P(i,n)+(c(3,i,k,1)+c(3,i,k,3)*b(n))*B(k,n);
                  end

P(7,n)=P(3,n)*exp(j*b(n)*2*pi*h/lambda1);
                P(3,n)=P(3,n)-B(3,n)*((rhof*v^2)/bf);
                  end
```

```
                    P(4,n)=-(ep(1,3)+ep(3,3)*b(n)+j*epf)*B(4,n);
                    P(8,n)=-(ep(1,3)+ep(3,3)*b(n)-
j*ep0)*B(4,n)*exp(j*b(n)*2*pi*h/lambda1);
                    for k=1:3
                        P(4,n)=P(4,n)+(e(3,k,1)+e(3,k,3)*b(n))*B(k,n);

P(8,n)=P(8,n)+(e(3,k,1)+e(3,k,3)*b(n))*B(k,n)*exp(j*b(n)*2*pi*h/lambda1
);
                    end
                end
            end
              for n=1:8
                for i=5:6
                    P(i,n)=0;
                    s=i-4;
                    P(i,n)=P(s,n)*exp(j*b(n)*2*pi*h/lambda1);
                end
             end
            velocity(vloop)=v;
            DP(vloop)=abs(det(P)); % determinant of P
            v=v+vstep;% increment in velocity
        end
%     count1=1;
%     for vc=1:itrn-2
%         if DP(vc)>DP(vc+1)&&  DP(vc+1)<DP(vc+2) &&  DP(vc+1)<pcompare
%            h1=round(h*100)
%            vlowest(h1,count1)=velocity(vc+1)
%            DDP(h1,count1)=DP(vc+1)
%            count1=count1+1;
```

```
%         end
%     end
for i=1:length(DP)
if(min(DP)==DP(i))
    DP(i)
vlowest(vloop)=velocity(i);
vlowest(vloop)
else
i=i+1;
end
end
    figure(1)
    plot(velocity(2:vloop-2),DP(2:vloop-2))
    ylabel('P')
    xlabel('v')
    title('Plot of P versus velocity to search minima')
    count=count+1;
    hh(count)=h;% values of h
end
```

Appendix B: Derivation of Equation for Attenuation Coefficient α

The relation between the attenuation coefficient α and imaginary part of the propagation velocity can be derived as follows.

Let $v = v^R + jv^I$.

Then the propagation constant k is given by

$$k = \frac{w}{v}$$

$$= \frac{w}{v^R + jv^I}$$

$$= \frac{w}{|v|^2}(v^R - jv^I)$$

$$= \frac{w}{|v|}\frac{(v^R - jv^I)}{|v|}$$

$$= |k|\frac{(v^R - jv^I)}{|v|}$$

Thus the imaginary part of k is given by

$$k^I = -|k|(\frac{v^I}{|v|})$$

The propagation of the wave in the x direction is represented by e^{jkx}. We get

$$e^{jkx} = e^{j(k^R + jk^I)x} = e^{-k^I x}e^{jk^R x}$$

Thus k^I, the imaginary part of k, gives rise to attenuation of the wave along the propagation direction. If $A_1$and A_2 denote the wave amplitudes at points x and $x + \Delta x$ respectively, we get

$$\frac{A_1}{A_2} = e^{k^I(\Delta x)}$$

Therefore wave attenuation in dB in distance Δx is

$$= 20log_{10}(A_1/A_2)\ dB = (20log_{10}e)(k^I\Delta x) = 8.67(k^I\Delta x)$$

If Δx = the wavelength λ, then

$$k^I\lambda = |k|\ \lambda\frac{v^I}{|v|} = 2\pi\ \frac{v^I}{|v|}$$

Therefore attenuation in dB per wavelength

$$= 8.67 \times 2\pi\ \frac{v^I}{|v|} = 54.58\ \frac{v^I}{|v|}\ dB/\lambda$$

Since $v^I \ll v^R$, we have $|v| \cong v^R$ and so we can write attenuation α in dB per wavelength as $\alpha = 54.58\ (v^I/v^R)$.

Appendix C: SPICE Level 3 parameters of NMOS and PMOS transistors in our ASIC chip

```
* DATE: Mar 31/09
* LOT: T8CD                  WAF: 6102
* DIE: N_Area_Fring          DEV: N3740/10
* Temp= 27
.MODEL CMOSN NMOS (                                LEVEL
= 3
+ TOX    = 3.12E-8         NSUB   = 9.774379E15     GAMMA
= 0.773496
+ PHI    = 1               VTO    = 0.6204887       DELTA
= 0.6077766
+ UO     = 551.3067103     ETA    = 8.822751E-4     THETA
= 0.073779
+ KP     = 7.212452E-5     VMAX   = 2.101886E5      KAPPA
= 0.5
+ RSH    = 21.8240936      NFS    = 5.686446E11     TPG
= 1
+ XJ     = 3E-7            LD     = 7.881538E-15    WD
= 6.680894E-7
+ CGDO   = 2.13E-10        CGSO   = 2.13E-10        CGBO
= 1E-10
+ CJ     = 2.855654E-4     PB     = 0.8852603       MJ
= 0.5
+ CJSW   = 1.077247E-10    MJSW   = 0.05            )
*
```

```
* DATE: Mar 31/09
* LOT: T8CD                  WAF: 6102
* DIE: P_Area_Fring          DEV: P3740/10
* Temp= 27
.MODEL CMOSP PMOS (                                LEVEL
= 3
+ TOX    = 3.12E-8         NSUB   = 1E17           GAMMA
= 0.4944052
+ PHI    = 0.7             VTO    = -0.9072807     DELTA
= 0.3899087
+ UO     = 102.2071731     ETA    = 1.471018E-4    THETA
= 0.1284443
+ KP     = 2.415694E-5     VMAX   = 1.439273E5     KAPPA
= 50
+ RSH    = 0.2005287       NFS    = 5.309638E11    TPG
= -1
+ XJ     = 2E-7            LD     = 1.000829E-14   WD
= 1E-6
+ CGDO   = 2.39E-10        CGSO   = 2.39E-10       CGBO
= 1E-10
+ CJ     = 2.93836E-4      PB     = 0.8            MJ
= 0.448408
+ CJSW   = 1.479762E-10    MJSW   = 0.0817737      )
*
```